From microscopic simulations towards a macroscopic description of granular media

Von der Fakultät Physik der Universität Stuttgart
zur Erlangung der Würde eines
Doktors der Naturwissenschaften (Dr. rer. nat.)
genehmigte Abhandlung

vorgelegt von

MARC LÄTZEL

aus Braunschweig

Hauptberichter:	PD. Dr. S. Luding
Mitberichter:	Prof. Dr. U. Seifert

Tag der mündlichen Prüfung: 30.01.2003

Institut für Computeranwendungen 1
der Universität Stuttgart

2003

”We know more about the movement of celestial bodies than about the soil underfoot.”

Leonardo Da Vinci, ≈ 1530

Contents

Contents 5

Nomenclature 9

List of Symbols 9

1. Deutsche Zusammenfassung 13

1.1 Einführung 13

1.2 Übersicht 15

1.3 Das Modellsystem 16

1.4 Die Molekulardynamik 17

1.5 Die Mittelungsmethode 19

1.6 Vergleich zwischen Simulation und Experiment 20

1.7 Der Mikro-Makro-Übergang 21

1.8 Rotationsfreiheitsgrade 23

1.9 Vergleich mit einem Kontinuumsmodell 24

1.10 Zusammenfassung und Ausblick 25

2. Introduction 27

2.1 Overview 32

3. The Model System 35

3.1 Motivation and History 37

3.2 The Setup 39

3.3 Preparation of the Sample 41

3.4 Differences between Experiment and Simulation 43

3.5 Conclusion 44

4. The Simulation Method 45

4.1 Molecular Dynamics 46

4.2 Force Laws 48

4.2.1 Normal Forces 49

4.2.2 Tangential Forces 51

4.2.3 Effect of Different Tangential Force Laws 55

4.2.4 Bottom Forces 56

4.2.5 Non-linear Forces 56

4.3 Conclusion 57

5. The Averaging Method 59

5.1 Averaging Strategy 60

5.2 The Averaging Formalism 62

5.3 Representative Elementary Volume (REV) 65

5.4 Conclusion 68

6. Comparing Simulation and Experiment 69
6.1 Density Change with Time 70
6.2 Changing the Packing Fraction 72
6.2.1 Density 73
6.3 Kinematic Quantities 77
6.3.1 Velocity Profiles 77
6.3.2 Spin Profiles 80
6.3.3 Velocity Distributions 81
6.4 Conclusion 84

7. The Micro-Macro-Transition 87
7.1 Classical Continuum Theory 89
7.2 The Micro-Mechanical Fabric Tensor 95
7.2.1 The Fabric Tensor for one Particle 96
7.2.2 The Averaged Fabric Tensor 97
7.2.3 Properties of the Fabric Tensor 98
7.2.4 Contact Probability Distribution 101
7.3 The Dynamical Micro-Mechanical Stress Tensor 104
7.3.1 The Mean Stress for one Particle 105
7.3.2 The Averaged Stress Tensor 110
7.3.3 Behavior of the Stress 110
7.3.4 Conclusion 114
7.4 Total Elastic Deformation Gradient 115
7.4.1 Behavior of the Total Elastic Deformation Gradient . . 118
7.4.2 Conclusion 120
7.5 Material Properties 121

7.6 Constitutive Law 124
7.7 Conclusion 127

8. Rotational Degrees of Freedom 129
8.1 Cosserat Theory 130
8.2 Rotational Degree of Freedom in the Simulation 135
8.3 Conclusion 138

9. Frictional Cosserat Model 141
9.1 Mohan's Model 142
9.2 Comparison 147
9.3 Conclusion 150

10. Conclusion 153
10.1 From a Microscopic Point of View... 154
10.2 ...to a Macroscopic Description 155
10.3 Outlook 157

Bibliography 161

Acknowledgments 171

Nomenclature

As for the notation, we generally employ Roman letters with an arrow above for vectors and boldface letters for second-rank tensors. Particles are identified by Roman superscripts $i, j, \ldots$. Tensor components are denoted by Greek indices $\alpha, \beta, \ldots$, with expressions of the form $\psi_{\alpha\beta}$. The symmetric part of a tensor will be indicated by round brackets as $\psi_{(\alpha\beta)}$ while the antisymmetric part is denoted by $\psi_{[\alpha\beta]}$.

The tensor product of $\psi_{\alpha\beta}$ and $\phi_{\alpha\beta}$ is denoted by $\boldsymbol{\psi} \otimes \boldsymbol{\phi}$ to be distinguished from the contraction of indices (scalar product in the case of vectors) $\boldsymbol{\psi} \cdot \boldsymbol{\phi}$.

We further adopt certain notations of the modern continuum-mechanics literature (BECKER AND BÜRGER [8]; TRUESDELL [98]), in particular $\boldsymbol{\sigma}$ for the stress tensor. Each symbol is declared upon its first appearance. A list of symbols is also included below.

List of Symbols

Symbol	meaning throughout this thesis
$\vec{a}$	vectorial quantity
$\boldsymbol{a}$	tensorial quantity
$\dot{a}$	time derivative
a_r	radial outwards component of a
a_ϕ	azimutal/tangential component of a
$a_{\alpha\beta}$	component $\alpha\beta$ of tensor $\boldsymbol{a}$
$a_{(\alpha\beta)}$	component $\alpha\beta$ of symmetric part of tensor $\boldsymbol{a}$
$a_{[\alpha\beta]}$	component $\alpha\beta$ of skew symmetric part of tensor $\boldsymbol{a}$

Symbol	meaning throughout this thesis
a_i	radius of particle i
$\mathcal{B}$	body in the actual configuration
$\tilde{d}$	reference diameter of the particles

Symbol	meaning throughout this thesis
d_{small}	diameter of the small particles
d_{large}	diameter of the large particles
D	diameter of the inner wheel
δ	overlap between two particles
Δt	time step
e^n	coefficient of normal restitution
E	granular stiffness
η	length of the tangential spring
$\boldsymbol{\varepsilon}$	total elastic deformation gradient
$\vec{f}$	forces
$\vec{f}^n$	normal direction of force
$\vec{f}^t$	tangential direction
$\boldsymbol{F}$	fabric tensor
G	shear stiffness
γ^n	viscous damping constant in normal direction
γ^t	viscous damping constant in tangential direction
J	moment of inertia
k^n	springconstant in normal direction
ℓ	Cosserat length
m	mass
$\vec{M}$	external moments
$\boldsymbol{M}$	couple stress tensor
μ_C	Coulomb constant
ν	local volume fraction
$\bar{\nu}$	global volume fraction
ω	angular velocity
$\bar{\omega}$	continuum rotation velocity
ω^*	excess rotation
Ω	angular velocity of the inner wheel
$\bar{\nu}$	global volume fraction
r	radial distance of a particle from the center of the shearing device
r_i	radial position of particle i
$\tilde{r}$	dimensionless distance from the inner wheel $(r-R_i)/\tilde{d}$
R_i	inner radius of the shear cell
R_o	outer radius of the shear cell
ϱ	density
ϱ^p	density of the particles
$\boldsymbol{\sigma}$	stress tensor

Symbol	meaning throughout this thesis
t	time
τ^M	bottom torque parameter
$\vec{x}$	position

1 Deutsche Zusammenfassung

1.1 Einführung

Sitzt man am Strand und beobachtet Kinder beim Bau von Sandburgen oder Pferde die über den Sand galoppieren, wird sich kaum jemand Gedanken über eine mathematische Beschreibung des Sandes machen. Dennoch lohnen sich diese Gedanken. Sand gehört zu einer Gruppe von Materialien, die als *granulares Material* oder *Schüttgut* bezeichnet wird. Im alltäglichen Gebrauch fallen uns granulare Materialien meist nicht auf, obwohl bereits beim Frühstück das Kaffeepulver oder die Cornflakes Beispiele granularer Medien sind. Zucker, Tabletten oder Zahncreme sind weitere Beispiele granularen Materials im Haushalt. Auch im industriellen Umfeld sind Schüttgüter wie Erze, Zement oder auch Plastikgranulate omnipräsent. Aufgrund ihrer Allgegenwärtigkeit erscheinen Granulate häufig als einfach und gut verstanden, allerdings geben einige Phänomene im Verhalten von Schüttgütern bis heute Rätsel auf.

Wir haben uns daran gewöhnt Materialien in flüssig, gasförmig oder fest zu unterscheiden. Für Schüttgut trifft dieses Schema jedoch nur bedingt zu. Vakuumverpackter Kaffee beispielsweise scheint ein fester Block zu sein, öffnet man jedoch die Verpackung, so lässt sich das Pulver fast wie eine Flüssigkeit ausgießen. Andererseits bildet das Pulver auf einem Tisch einen Haufen und zerfließt nicht wie Wasser. Die gasartige Verhaltensweise von

Granulaten zeigt sich, wenn man diese stark schüttelt. Granulares Material zeigt also durchaus das Verhalten der klassischen Phasen, darüber hinaus lassen sich jedoch Phänomene wie „nicht-Gleichverteilung der Energie“, Klusterbildung, Phasenübergänge, Glasphasen, Anisotropie, Strukturbildung und hysteretisches Verhalten beobachten. All diese Beispiele zeigen, dass es nicht immer möglich ist Schüttgüter mit einer der klassischen Methoden wie der Hydrodynamik, der kinetischen Gastheorie oder der Kontinuumstheorie, zu beschreiben.

Eine Eigenschaft granularer Medien, welche die Verwendung klassischer Kontinuumstheorien verhindert, sind starke Fluktuationen beispielsweise der Kräfte innerhalb des Materials. Diese Kräfte werden durch die Kontakte zwischen den Teilchen übertragen. Die Richtung dieser Kraftübertragung wird dabei möglichst beibehalten, wodurch sich Strukturen ausbilden, die als *Kraftketten* bezeichnet werden. Von diesen Kraftketten wird nahezu die gesamte externe Last des Systems getragen, während direkt benachbarte Teilchen keine oder nur geringe Kräfte erfahren und so lediglich das “starke” Kraftnetzwerk stabilisieren. Dadurch entsteht eine starke Inhomogenität innerhalb des Granulates. Diese Inhomogenität ist letztendlich auch die Ursache beispielsweise für das zu beobachtende Verstopfen von Silos. Dabei bilden sich, während das Silo geleert wird, Kraftketten als eine Art Bogen vor dem Auslass und verhindern so das Nachfließen weiterer Teilchen. Ein weiteres wichtiges Phänomen bei granularem Material ist die *Dilatanz*. Läuft man am Strand entlang, so kann man feststellen, dass sich beim kräftigen Auftreten auf nassem Sand der Fußabdruck nicht mit Wasser füllt, sondern die Umgebung des Abdrucks trocknet. Dieser Effekt lässt sich dadurch erklären, dass sich komprimierter Sand ausdehnen muss, bevor er sich verformen lässt und dadurch Platz für die Flüssigkeit zwischen den Teilchen schafft.

Dieser Effekt spielt auf einer größeren Skala auch bei Erdbeben, Erdrutschen oder Lawinen eine Rolle. Wenn sich bei Erdbeben beispielsweise zwei benachbarte Erdschollen aneinander vorbei bewegen, bildet sich zwischen beiden eine Zone, in der sich das Material (lokal) ausdehnen muss. In dieser *Dilatanzzone* finden sich vergleichsweise viele Einzelkörner welche rotieren, um dadurch die Bewegung der großen Blöcke zu ermöglichen. Die Dicke dieser lokalisierten Zonen beträgt nur wenige Korndurchmesser, dennoch wird in diesen *Scherzonen* oder *Scherbändern* die gespeicherte Energie freigesetzt, welche für das Erdbeben verantwortlich ist.

1.2 Übersicht

Die genannten Beispiele zeigen die Vielfalt von Effekten in granularer Materie. Die vorliegende Arbeit beschäftigt sich mit Scherzonen und Dilatanz in einem gescherten Granulat, ihrer Modellierung und theoretischen Beschreibung. Der Aufbau der Arbeit spiegelt dieses Ziel wider, indem zunächst ein experimentelles Modellsystem vorgestellt und anschließend mittels einer Molekulardynamik simuliert wird. Um einen Vergleich von Experiment und Simulation zu ermöglichen, wird ein geeigneter Mittelungsformalismus entwickelt, um aus den diskreten „mikroskopischen“ Größen der Simulation „makroskopische “ Messgrößen zu erhalten. Dieser Formalismus wird verwendet, um kinematische Größen wie Geschwindigkeitsprofile und Rotationen in der Simulation der Scherzelle zu ermitteln und mit den experimentellen Daten zu vergleichen. Aufgrund der gefundenen Vergleichbarkeit von Experiment und Simulation lassen sich dann vertrauenswürdige Aussagen auch über Größen treffen, die im Experiment gar nicht oder nur schwer zugänglich, jedoch für das Verständnis der Vorgänge innerhalb des Granulates hilfreich sind. Im Rahmen eines kontinuumstheoretischen Ansatzes werden die Spannungen und die Deformationen des Granulates bestimmt. Zusätzlich wird der *Fabric*-, oder Strukturtensor ermittelt, mit dessen Hilfe sich Aussagen über die innere Struktur des Schüttgutes, wie beispielsweise den Grad der Anisotropie, treffen lassen. Die ermittelten Feldgrößen werden dann verwendet, um Materialkenngrößen einer Kontinuumstheorie zu bestimmen. Dazu wird zunächst ein elastisches Materialgesetz nach Hooke verwendet und der Elastizitäts- und Schermodul berechnet. Da es sich zeigt, dass die Rotationen der einzelnen Körner im System eine wichtige Rolle für das Verhalten des Materials insbesondere in der Scherzone spielen, führen wir einen Cosserat-Ansatz ein, in welchem die klassische Kontinuumstheorie um die rotatorischen Freiheitsgrade erweitert wird. Daher müssen die Bilanzrelationen um Gleichungen für Momente und Krümmungen erweitert werden. Diese Größen werden ebenfalls aus den Simulationen bestimmt und eine neue Materialgröße, die *Verdrehungssteifigkeit* errechnet. Im letzten Teil der vorliegenden Arbeit werden die Ergebnisse der Simulationen mit den Vorhersagen eines elastoplastischen Cosserat-Modelles verglichen. Da experimentelle Daten für diesen Vergleich fehlen, bietet die Simulation hier erstmals die Möglichkeit einen Test des Modells durchzuführen.

1.3 Das Modellsystem

Im Gegensatz zu Effekten von Granulaten in der Natur, bei denen eine sehr große Anzahl von Körnern beteiligt ist, ist es sinnvoll sich bei Laborversuchen und Simulationen zum Verständnis granularer Materie auf eine begrenzte Anzahl von Teilchen zu beschränken. Daher werden meist nur Teil- oder Modellsysteme untersucht. Um die Bildung und Entwicklung von Scherbändern studieren zu können, muss über einen längeren Zeitraum hinweg eine Scherung auf ein Granulat ausgeübt werden. Die Couette-Scherzelle ist ein Gerät, mit dem dies möglich ist. Daher wird sie für die vorliegende Arbeit als Modellsystem verwendet. Eine 2-dimensionale experimentelle Umsetzung des Gerätes wurde an der Duke University in Durham (USA) in der Gruppe um Prof. Behringer entwickelt und experimentell untersucht.

Die Geometrie der simulierten Scherzelle wurde den Abmessungen der experimentellen Anlage angepasst, um soweit möglich einen quantitativen Vergleich und eine Eichung der Simulationsergebnisse vornehmen zu können. In Abb. 1.1 ist die Scherzelle schematisch dargestellt. Zwischen einem inneren und einem äußeren Zylinder befinden sich Plexiglasscheibchen zweier unterschiedlicher Radien. Durch die beiden unterschiedlichen Teilchenradien werden Kristallisationseffekte reduziert, wenn auch nicht ganz verhindert. Der innere Ring des Gerätes kann um die Symmetrieachse rotieren, der äußere Ring wird festgehalten, somit bleibt das Volumen der Scherzelle konstant. Der Boden des Apparats ist mit einer dünnen Schicht Backpulver bestreut, um die Reibung der Teilchen mit der Bodenplatte zu reduzieren.

Im Experiment werden die Teilchen einzeln von Hand in die Scherzelle eingesetzt. In der Simulation werden die Teilchen auf einem Dreiecksgitter aufgesetzt, wobei der äußere Zylinder zunächst einen größeren Radius besitzt und erst langsam auf den experimentellen Wert geschrumpft wird, um so eine dichte Teilchenpackung zu erhalten.

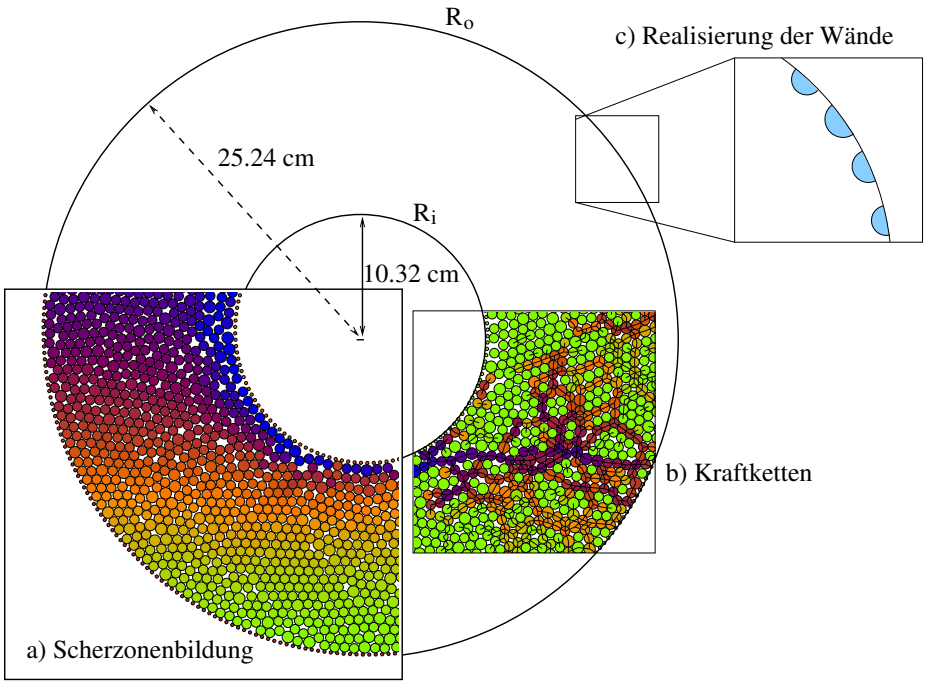

Fig. 1.1: *Schematische Draufsicht des experimentellen Aufbaus.* **a)** *Bildung einer Scherzone nach einer halben Umdrehung des inneren Ringes. Die Farbe der Teilchen kodiert die vertikale Position der Teilchen zu Beginn der Simulation.* **b)** *Kraftketten in einem Teilbereich der Scherzelle nach einigen Rotationen des Innenrings. Die Stärke der übertragenen Käfte ist farblich markiert. Dabei bedeutet dunkel starke Kräfte und hell schwache.* **c)** *Skizze der Realisierung der Ränder in der Simulation.*

1.4 Die Molekulardynamik

Für die Simulation wird eine Molekulardynamik (MD) bzw. Diskrete-Elemente-Methode (DEM) verwendet. Dabei werden die Newtonschen Bewegungsgleichungen aller Teilchen numerisch integriert. Für die Integration wird ein *Verlet-Verfahren* verwendet. Um die aufwendige Suche nach benachbarten Teilchen (Stoßpartnern) zu beschleunigen, wurde ein *Linked-Cell* Algorithmus implementiert.

Für die Modellierung spielen die Wechselwirkungskräfte zwischen den Teilchen eine entscheidende Rolle. In der hier verwendeten Simulationsmethode werden die Wechselwirkungen als Kontaktkräfte mit Dissipation und Reibung zwischen Teilchenpaaren beschrieben.

Die Teilchenzentren befinden sich an den Orten $\vec{x}^i$ ($i = 1, \ldots, N$) und die Größe der Teilchen wird durch den Radius a_i bestimmt. Zwei Teilchen i und j sind in Kontakt, sobald sich ihre Umrisse überlappen und üben dann eine gegenseitige Kraft aufeinander aus („actio = reactio“). Man zerlegt die Kraft zwischen den Teilchen eines Paares in eine normale Komponente $\vec{f}_{ij}^{\,n}$, die der Abstoßung und Energie-Dispersion Rechnung trägt und eine tangentiale Komponente $\vec{f}_{ij}^{\,t}$, für welche die Reibung verantwortlich ist.

Sieht man von starken „plastischen“ Verformungen wie lokalen „Dellen“ oder Brüchen der Teilchen ab, so lässt sich die Normalkraft in einen elastischen und einen dissipativen Anteil zerlegen. Für die Simulation von Scheiben wird im einfachsten Fall ein lineares Gesetz verwendet. Die Kraft ist dabei proportional zum virtuellen Überlapp $\delta = |\vec{x}_i - \vec{x}_j| - (a_i + a_j)$ der Teilchen. Der zweite Anteil der Normalkraft trägt der Dissipation von Energie während des Stoßes Rechnung und wird mittels einer viskosen, dissipativen Kraft beschrieben, die proportional zur Normalkomponente der Relativgeschwindigkeit zweier kontaktierender Teilchen ist.

Die Tangentialkräfte $\vec{f}^{\,t}$ lassen sich im einfachsten Fall als Coulombsche Reibungskräfte $\vec{f}^{\,t}_{\mathrm{Coulomb}}$ definieren. Dabei ist jedoch die statische Reibung zwischen den Teilchen als wichtiges Element realistischer Simulationen nicht berücksichtigt. Eine quasi-statische Reibungskraft kann als Cundall-Strack-Feder implementiert werden. Hierbei verwendet man als Tangentialkraft die Länge einer imaginären Tangentialfeder, die sich zum Zeitpunkt des Kontaktbeginns zwischen zwei Teilchen ausbildet. Das Kraftgesetz erwies sich als zuverlässig, stabil und realistisch insofern, als dass statische Packungen erzeugt werden konnten. Zusammenfassend lässt sich die Kraft auf ein Teilchen i damit als

$$\vec{f}_i = \sum_c (\vec{f}^{\,n}_{\mathrm{el}} + \vec{f}^{\,n}_{\mathrm{diss}} + \vec{f}^{\,t}) + \vec{f}_{\mathrm{b}} \tag{1.1}$$

beschreiben, wobei sich die Summe über die Kräfte an allen Kontaktpunkten c erstreckt und weiterhin eine Volumenkraft $\vec{f}_{\mathrm{b}}$ wie die Gravitation berücksichtigt werden kann. Berechnet man neben den Kräften und daraus entstehenden Beschleunigungen noch die Drehmomente und entsprechende Rotationen, so ist die Dynamik des Systems vollständig beschrieben und die Bewegungsgleichungen können numerisch integriert werden.

1.5 Die Mittelungsmethode

Um die Ergebnisse diskreter Simulationen mit physikalischen (makroskopischen) Messungen vergleichen zu können, bedarf es effizienter Mittelungsmethoden, welche die diskreten Werte der Simulation homogenisieren und so das Verhalten des Granulats als Ganzes beschreiben. Dazu wird ein Mittelungsformalismus definiert, mit dem sich neben skalaren Größen (wie Dichte oder Koordinationszahl) auch vektorielle und tensorielle Felder (wie Geschwindigkeit, Spannung oder Geschwindigkeitsgradient) ortsabhängig ermitteln lassen. Aufgrund der Symmetrie des untersuchten Systems, sind alle Teilchen gleichen Abstands zum Zentrum gleichwertig. Daher lassen sich Mittelungen sowohl räumlich (in Kreisringen), wie auch zeitlich (quasistationärer Zustand) durchführen.

Ausgangspunkt für unseren Formalismus ist die naheliegende Definition des lokalen Volumenanteils

$$\nu = \frac{1}{V} \sum_{p \in V} w_V^p V^p \,, \tag{1.2}$$

den man aus der allgemeinen Beziehung für eine beliebige Größe Q

$$Q = \langle Q^p \rangle = \frac{1}{V} \sum_{p \in V} w_V^p V^p Q^p \,, \tag{1.3}$$

erhält, indem man die für ein Teilchen definierte Größe $Q^p = 1$ setzt. V^p ist dabei das Teilchenvolumen und w_V^p der Gewichtsfaktor des Teilchens p.

Für die Wahl von w_V^p gibt es mehrere Möglichkeiten: zum einen kann man eine teilchenzentrierte Mittelung durchführen, eine andere Möglichkeit ist die zu mittelnde Größe gleichmäßig über das Teilchen zu verschmieren und nur den im Mittelungsvolumen V liegenden Anteil des Teilchen zu berücksichtigen. Die zweite Methode erwies sich als wesentlich robuster und führte zu realistischen Resultaten. Interessanterweise stimmen beide Mittelungsverfahren gerade dann besonders gut überein, wenn die Dicke Δr des Mittelungskreisrings in etwa so groß wie ein Teilchendurchmesser gewählt wird.

Eine beliebige Größe Q^p, die für ein Teilchen p definiert ist, lässt sich mit Glg. 1.2 in das zugehörige Volumen-Mittel überführen. Dabei kann die Teilcheneigenschaft Q^p ein Tensor beliebiger Stufe sein, die gemittelte makroskopische Größe $Q = \langle Q^p \rangle$ besitzt dann die entsprechende Tensorstufe.

1.6 Vergleich zwischen Simulation und Experiment

Ein Ziel dieser Arbeit war es eine Simulation zu entwickeln, welche sich mit einem existierenden Experiment vergleichen lässt. Unsere Ergebnisse zeigen zumeist sehr gute qualitative, in vielen Fällen auch quantitative Übereinstimmung mit dem Experiment.

Sowohl im Experiment als auch in der Simulation entwickelt sich aus einer anfänglich homogenen Dichte, in radialer Richtung eine Dilatanzzone innen und eine leicht komprimierte Zone außen. Dabei bildet sich aufgrund der durch die Drehung des inneren Ringes induzierten Scherung und der daraus resultierenden Dilatanz an der inneren Wand ein Scherband aus. Die Dichteprofile aus Simulation und Experiment stimmen dabei gut miteinander überein. Aus beiden lässt sich eine Scherbandbreite von ca. $5 - 6$ Teilchendurchmessern ablesen.

Besondere Aufmerksamkeit bei den Vergleichen galt der Variation der globalen Packungsdichte $\bar{\nu}$. Dabei zeigte es sich, dass sich das System für Packungsdichte von $\bar{\nu} < 0.793$ in einem subkritischen Bereich befindet. In diesem Bereich besteht nach einigen Umdrehungen des Innenrings kein Kontakt mehr zwischen Ring und System, da alle Teilchen nach außen gedrückt werden. Erhöht man die Dichte, so findet sich am inneren Ring ein ausgeprägtes Scherband, welches mit weiter zunehmender Dichte schmäler wird und schließlich bei einer Packungsdichte von $\bar{\nu} > 0.811$ nur noch schwer zu bestimmen ist. Bei diesen hohen Dichten können die Teilchen nicht mehr ausreichend gegeneinander verschoben werden, das System ist blockiert.

Betrachtet man das Profil der Tangentialgeschwindigkeit als Funktion des radialen Abstands vom Zentrum, so findet man sowohl in den Simulationen wie auch in den Experimenten ein exponentielles Abklingen der Geschwindigkeit wenn man sich vom inneren Ring entfernt. Allerdings ist in den Experimenten deutlich zu erkennen, dass die Amplitude der Geschwindigkeit mit zunehmender Packungsdichte ebenfalls zunimmt. In unseren Simulationen lässt sich dies nur für hohe Dichten eindeutig feststellen, bei geringen Dichten scheinen Unterschiede in der Implementierung der Wände und der Bodenreibung einen starken Einfluss zu haben.

Sowohl im Experiment wie auch in den Simulationen lassen sich die Rota-

tionen der Körner messen. Dabei findet man ein Oszillieren der Rotationsrichtung der Teilchen, wenn man sich vom inneren Ring entfernt. Die Teilchen verhalten sich dabei wie eine Art Kugellager, in dem sie Schichtweise aufeinander abrollen um so die Scherung zu erleichtern.

Betrachtet man die Häufigkeitsverteilungen der Tangentialgeschwindigkeiten und der Rotationen der Teilchen nahe des inneren Ringes, so zeigen diese sowohl in den Simulationen, wie auch in den Experimenten eine komplexe Struktur, welche ebenfalls von der globalen Packungsdichte abhängt. Zum Verständnis dieser Struktur hilft es, die Korrelation zwischen Rotation und Tangentialgeschwindigkeit zu betrachten. Dabei zeigt sich, dass sich für geringe Dichten die meisten Teilchen in Ruhe befinden. Mit zunehmender Dichte findet man mehr und mehr Teilchen in einem Zustand, in dem sie eine Kombination aus Dreh- und Translationsbewegung ausführen, um dadurch ein Abgleiten auf anderen Teilchen und dem inneren Ring zu verhindern.

Zusammenfassend lässt sich also feststellen, dass die vorliegende, vergleichsweise „einfache“ Simulation in der Lage ist, das Verhalten eines Modellexperimentes qualitativ, in vielen Fällen auch quantitativ zu reproduzieren. Diskrepanzen in den Ergebnissen lassen sich auf Unterschiede zurückführen, deren Implementierung eines enorm großen Aufwands bedürfte, wie beispielsweise die Möglichkeit der Teilchen sich aus der Bewegungsebene zu verkippen. Die Übereinstimmungen ermutigen jedoch im Weiteren auch Größen zu bestimmen, welche im Referenzexperiment nicht zugänglich sind und diesen Größen zu vertrauen.

1.7 Der Mikro-Makro-Übergang

Das übergeordnete Ziel von diskontinuierlichen, mikro- oder mesoskopischen Simulationsverfahren ist letztendlich das Verständnis des Materialverhaltens, auch auf makroskopischer Ebene. Dieser Übergang von den zu bestimmenden Größen und Eigenschaften des diskreten Mikrosystems zu einer makroskopischen Kontinuumsbeschreibung und die damit verbundene Vorhersagbarkeit des für praktische Anwendungen interessierenden Materialverhaltens, war ein weiterer Schwerpunkt unserer Arbeit.

Aufgrund der gefundenen Vergleichbarkeit von Experiment und Simulation, lassen sich vertrauenswürdige Aussagen auch über Größen treffen, welche im Experiment gar nicht oder nur schwer zugänglich sind.

Als ein Beispiel sei hier der Strukturtensor genannt. Dieser, obwohl nicht Bestandteil der klassischen Kontinuumstheorie, beschreibt zu einem gewissen Grad die innere Struktur des Granulates. Aus der Orientierung der Hauptachsen des Strukturtensors lässt sich ermitteln, ob es innerhalb des Systems eine Vorzugsrichtung gibt, in welcher sich vermehrt Kontakte befinden. Im Fall der vorliegenden Scherzelle findet man nahe des inneren Ringes bevorzugt Kontakte in tangentialer Richtung, die durch die Wand-Nahordnung hervorgerufen werden. Ebenso finden sich Kontakte in Richtung von 60^0 gegen die Tangentialrichtung. Diese Kontakte bilden sich, da sich das Granulat gegen die Scherung wehrt. Entfernt man sich vom Innenring, so wird die Kontaktverteilung zunehmend homogener, bevor sie im äußeren Bereich erneut anisotrop wird. Diese Anisotropie rührt allerdings aus Kristallisationseffekten in der Kompressionsphase der Simulation her und repräsentiert eine Dreiecksgitter-Struktur. Da die Dynamik im Außenbereich der Scherzelle sehr langsam ist, überleben diese Strukturen sehr lange.

Um Aussagen über das makroskopische Verhalten von Granulaten unter Belastung von außen machen zu können, müssen makroskopische Zustandsgrößen aus der Mittelung mikroskopischer Größen gewonnen werden. Für praktische Zwecke wird dabei gemeinhin eine Spannungs-Dehnungs Beziehung als unverzichtbar angesehen. Im Rahmen dieser Arbeit wurde die Bestimmung dieser Größen aus den mikroskopischen Variablen Kontaktkräfte, Kontaktvektoren und Verformungen am Kontakt hergeleitet. Dabei wurden insbesondere auch die Anteile des Spannungstensors berücksichtigt, die sich aus der Dynamik des Granulates ergeben. Für diese kann jedoch gezeigt werden, dass sie um einige Größenordnungen kleiner sind als die Spannungen aus den wirkenden Kräften. Daher kann der dynamische Anteil hier vernachlässigt werden.

Das Verhalten der Komponenten des Spannungstensors lässt sich aus kontinuumstheoretischen Überlegungen herleiten. So sind die Hauptdiagonalelemente des Spannungstensors konstant, während die Nebendiagonalelemente die die Scherung beinhalten mit $1/r^2$ abklingen, wenn man sich radial auswärts bewegt.

Die Definition eines makroskopischen Dehnungstensors ist ein kontrover-

ses Thema der aktuellen Forschung. Unsere Definition des Dehnungstensors basiert auf der Arbeit von LIAO ET AL. [51]. Mit dem verwendeten Minimierungsverfahren wurde der elastische Dehnungstensor bestimmt. Mit Hilfe von Spannung und Dehnung kann man dann versuchen Stoffgesetze für granulares Material zu formulieren, um so wiederum zu einer Kontinuumstheorie zu gelangen. Basierend auf einem isotropen, elastischen Stoffgesetz konnten wir die Steifigkeit E des granularen Materials für verschiedene globale Packungsdichten bestimmen. Obwohl die Annahme der Isotropie für das verwendete System in weiten Bereichen nicht zutrifft, lassen sich dennoch die Steifigkeiten bei verschiedenen Dichten auf eine gemeinsame Kurve skalieren, wenn sie gegen die Spur des Strukturtensors aufgetragen werden. Dieses Resultat lässt sich auch aus „mean field“ Überlegungen ableiten. Ebenso das Verhalten der Schersteifigkeit G.

1.8 Rotationsfreiheitsgrade

Ein besonderes Phänomen in Scherexperimenten sind die in der Scherzone verstärkt auftretenden Teilchenrotationen. Die Rotationen ermöglichen den Schichten des Granulats kugellagerartig aufeinander abzugleiten. In einer klassischen Kontinuumstheorie werden die Rotationsfreiheitsgrade jedoch nicht berücksichtigt. Daher wurde in der vorliegenden Arbeit ein Cosserat-Kontinuum als Erweiterung gewählt. Dabei werden jedem Materiepunkt zusätzlich zu den translatorischen Freiheitsgraden auch rotatorische Freiheitsgrade zugeordnet. Die Gesamtrotation der Teilchen (Spindichte) setzt sich aus einer Kontinuumsrotation und der Teilchenzusatzrotation ω^* zusammen. Die Kontinuumsrotation lässt sich aus der klassischen Kontinuumstheorie insbesondere aus dem Geschwindigkeitsgradienten ableiten. Die abgeleitete Größe stimmt gut mit den Ergebnissen der Simulationen überein.

Die konstituierenden Gleichungen in einem Cosserat-Kontinuum müssen um eine Beziehung zwischen den Momentenspannungen und den Krümmungen erweitert werden. Jene erhält man aus den Definitionen der Spannungen $\boldsymbol{\sigma}$ und der Dehnungen $\boldsymbol{\varepsilon}$ durch Analogieüberlegungen, wobei Kräfte bzw. zugehörige Überlappungen jeweils durch Drehmomente bzw. Kreuzprodukte ersetzt werden.

Die genannten Größen bilden den Kern mikropolarer Theorien und die analytische Herleitung sowie das bessere Verständnis ihrer Eigenschaften sind Voraussetzung dafür, dass die interne Länge in der Cosserat-Theorie mit entsprechenden Längenskalen anderer Modelle verglichen werden kann. Das erste vielversprechende Resultat hierzu betrifft den Quotienten der Momentenspannung und der korrespondierenden Krümmung, der angibt, wie stark ein Material auf eine kleine Rotationsbewegung reagieren wird – er stellt also eine Verdrehungssteifigkeit (in Analogie zur Steifigkeit E) dar. Die Ergebnisse zeigen, dass die Rotationssteifigkeit in der Scherzone abnimmt (durch abnehmende Dichte und dadurch abnehmende Frustration) und aus ähnlichen Gründen, mit zunehmender Materialdichte systematisch zunimmt. Ein dichtes Material setzt also einem Drehmoment mehr Widerstand entgegen als ein dünneres.

1.9 Vergleich mit einem Kontinuumsmodell

Mit den aus den Simulationen gewonnenen makroskopischen Größen kann nun das mikropolare Modell eines elasto-plastischen Reibungsmaterials getestet werden. Für das von MOHAN ET AL. [65] vorgeschlagene Modell gibt es derzeit keine experimentelle Rechtfertigung. Aus der Simulation lassen sich hingegen alle benötigten Größen bestimmen und mit den Modellvorhersagen vergleichen. Dies zeigt, dass das Modell für die Geschwindigkeitsprofile, sowie die Rotationen exzellent mit den Daten der Simulation übereinstimmt. Auch das Verhalten der Asymmetrie des Spannungstensors, die sich aus einer Cosserat-Theorie ergibt, stimmt in Modell und Simulation qualitativ überein. Allerdings scheint das Modell zu einer Momentenspannung zu führen, welche mit wachsender Entfernung von der inneren Wand ansteigt. Dieses Verhalten steht in deutlichem Widerspruch zu den Ergebnissen der Simulation, in der die Momentenspannungen weg vom Innenring schnell abklingen. Hier muss eine genaue Untersuchung der Modellgleichungen klären was die Ursache für das falsche Modellverhalten ist.

1.10 Zusammenfassung und Ausblick

Um den Mikro-Makro-Übergang von einer „mikroskopischen“ zu einer kontinuumstheoretischen Beschreibung eines Granulates möglich zu machen, ist ein konsistenter allgemeiner Mittelungsformalismus entwickelt worden. Damit konnten neben der Dichte und dem Geschwindigkeitsfeld auch tensorielle Größen wie der Geschwindigkeitsgradient, der Spannungstensor, der elastisch-reversible Deformationsgradient und der Strukturtensor berechnet werden. Zusätzlich zu diesen Größen einer klassischen Kontinuumstheorie wurden aus der Teilchenrotation und der Kontinuumsdrehung die Teilchenzusatzrotation im Sinne einer mikropolaren Kontinuumstheorie bestimmt. In Analogie zu den klassischen Größen Spannungstensor und Deformationsgradient sind zuletzt auch der Momentenspannungstensor und die Krümmung ausgewertet worden.

Aus den tensoriellen Größen lassen sich verschiedene Materialparameter wie z.B. die isotrope Steifigkeit oder das Schermodul berechnen. Als neue Größe kommt die aus den mikropolaren Tensoren bestimmte Rotationssteifigkeit hinzu, die den Widerstand eines Materials gegenüber Drehungen einzelner Teilchen beschreibt.

Die vorgestellte Simulation kann mit einem Experiment verglichen und daran geeicht werden. Andererseits erhält man mit Hilfe der Simulation auch mehr Informationen über den Mikro-Makro-Übergang. Sie eignet sich daher, die Vorhersagen einer Kontinuumstheorie zu überprüfen. Simulationen sind daher ein wertvolles Werkzeug, um ein tieferes Verständnis des Verhaltens granularer Materie zu erlangen. Die hier gezeigten Ergebnisse haben dazu sicherlich beigetragen, jedoch haben sich durch die Arbeit auch neue Fragestellungen ergeben.

Im Rahmen dieser Arbeit haben wir uns auf runde Scheibchen beschränkt. Für die Simulation von realen Granulaten ist es jedoch von Interesse auch nicht runde Teilchen in einem dreidimensionalem Behälter zu simulieren. Nicht runde Teilchen ermöglichen einerseits einen stärkeren Drehmomentenübertrag, andererseits werden sich solche Teilchen deutlicher verhaken, wodurch Rotationen behindert werden.

Der vorgestellte Mittelungsformalismus erwies sich als sehr zuverlässig. In Systemen, die nicht wie das verwendete zeitliche wie auch räumliche Mit-

telungen erlauben, ist die Frage nach der Größe des Mittelungsvolumens immer noch offen.

Die verwendete Definition des Dehnungstensors berücksichtigt nur elastische Deformationen. Hier wäre eine Erweiterung, welche die plastische Verformungen des Granulates berücksichtigt, wünschenswert. Dazu muss jedoch die Umgebung eines Teilchens und deren Deformation miteinbezogen werden.

Im Hinblick auf die Verwendung eines Cosserat-Modells zur Beschreibung granularer Medien konnte diese Arbeit aufzeigen, dass in einem solchen Modell das Fließverhalten des Granulates zutreffend beschrieben wird. Für die Formulierung der Gleichungen der Momentenspannungen müssen jedoch weitergehende Überlegungen erfolgen. Dies insbesondere im Hinblick auf die Tatsache, dass sich die mikropolaren Effekte nur in der schmalen Scherzone des Granulates abspielen. Aufgrund der oszillierenden Rotationsrichtungen der Körner ist hier jedoch eine Mittelung äusserst schwierig und bedarf weiterer Untersuchungen.

Der Weg, um in einem Kontinuumsmodell das Verhalten eines Granulates auch in Scherzonen vorhersagen zu können scheint noch weit, jedoch interessant und gangbar.

2 Introduction

While sitting on a beach and watching children building sand castles or horses galloping on the sand no one will think of how to describe sand in a mathematical way. But it is worth thinking about. Sand belongs to a group of materials known as *granular materials*. Most of the time we handle granular materials in everyday life, we do not even notice it. At breakfast, the coffee powder and the cereals are granular materials. Sugar, drugs and tooth paste are other examples of granular media in a household. In industrial environments granular materials are also omnipresent, e.g. cement, ore and plastic pellets. With the abundance of granular materials they often seem particularly ordinary and well understood, yet there are a lot of phenomena which are still not (HERRMANN [39]; JAEGER AND NAGEL [46]).

We are adopted to sort matter into the categories of gas, fluid or solid. However, granular materials sometimes behave like either of the three states, or even different from any. As an example let us consider the coffee powder mentioned above: The vacuum packed block of coffee powder seems to be quite solid but by opening the package one can pour out the powder just like a liquid. Still, in contrast to a fluid the powder does not deliquesce but forms a heap, i.e. it behaves like a solid again. The gas-like behavior of granular material can be found by shaking a granular assembly heavily. These examples demonstrate that granular media show the behavior of the classical phases as special cases and, in addition, show a variety of extra phenom-

ena like non-equipartition of energy, clustering, phase transitions, jammed or glassy states, anisotropy, structuring and hysteretic behavior. Because of this variety of effects it is not possible to describe granular media always with one of the classical theories like hydrodynamics, kinetic gas theory or continuum mechanics.

One of the features of granular media which prohibits the use of classical theories are the strong fluctuations for example of the forces inside a granular assembly. In short range, the forces propagate along the contacts between the grains. Because they keep their direction the structure formed by this particles is called a *force chain*. Yet, directly in the neighborhood of the force chains there might be particles bearing no load. So there is a strong inhomogeneity inside the assembly which, in the end, is also responsible for the *clogging* in silos. While letting the grains flow out of a silo force chains sometimes develop at the outlet, blocking the descending particles and thus jam the silo.[1]Another fascinating property of granular materials is the *dilatancy*. While walking on the beach one might recognize that when stepping on wet sand the footprints do not fill with water, instead the surrounding of the print becomes dry. The effect is understood by considering the fact that compressed sand needs to dilate before becoming able to deform and thus leaving more space for the fluid between the grains. On a larger scale granular materials are also of interest to earth scientists in order to understand earthquakes, landslides or avalanches. Earthquakes may serve as an example for intermittent behavior. Most of the time the fragmented rock layer (termed "gouge") within a geological fault stays at rest. But sometimes two adjacent blocks of soil move relative to each other and energy is released by the fast moving blocks overcoming their blockages. Between the two blocks a zone forms which has to dilate. In this dilated region relatively many small particles are found to rotate in order to support the motion of the bigger blocks. These localized zones are only of the width of a few particle diameters and are called shear bands.

These few examples show the wide variety of effects occurring in granular media. In the present thesis we will focus on the shear zone and dilatancy in a sheared granular media. As a model system an actual experiment will be used and simulations are carried out, in order to finally evaluate a continuum theoretical approach predicting the collective behavior of a granular assembly.

[1] This is why you can sometimes see people hitting a silo with iron bars.

Experiments

In contrast to natural phenomena where a huge number of grains is involved, it is useful to investigate systems with a limited number of particles in order to obtain better insights into the underlying physics. These *reference experiments* have a long tradition in engineering science, where they are used to characterize granular media. Apart from the obvious properties of a granulate like grain sizes and their distribution or the volume fraction, there are further characteristic properties that are accessible via experiments. Especially in geotechniques various experiments with different boundary conditions exist, which are used for this purpose. For example the oedometer is used to determine the compressibility of a granular material while the shear resistance is measured with biaxial or triaxial devices. These devices are only capable to produce small deformations before the boundary conditions change significantly.

In order to observe the formation of shear bands shear has to be applied over a comparatively long time. Therefore, geometries are required which resemble a quasi infinite medium. In this kind of apparatus a quasi steady state develops and can be studied for long times and corresponding, large displacements. The physical realization of such a device is done by forming rings. The Couette shear cell used in this thesis belongs to this class of measurement tools. It consists of two concentric rings which are able to rotate. The granular material is confined between the two rings and by rotating one or two of the (often roughened) walls shear is induced at the walls and a shear band might form.

Continuous Modeling of Granular Media

Research activities in the field of granular media have attracted scientists and engineers with a variety of backgrounds. Not only physicists but also applied mathematicians, geologists, geophysicists, chemical, mechanical, and civil engineers have been working on a general physical or mathematical formalism that successfully predicts the collective behavior of a large number of grains. The modeling of the granular material is often done with a continuum-based model. In this kind of models the granular structure of the material is idealized with a continuum of *material points*. The corresponding field equations can be derived from the properties of a *representative elementary volume* (REV) in the vicinity of the point. The combina-

tion of classical continuum theory and hardening material theories has not been that successful. In particular, it results in a mathematically ill-posed problem because the numerical solutions show a mesh dependency. For example, the width of a shear band approaches zero in the limit of an infinite fine mesh (in the framework of a traditional continuum theory).

In recent years some regularization methods arose to circumvent this insufficiency. Among others the micropolar Cosserat continuum (COSSERAT AND COSSERAT [19]; DE BORST [24]; MÜHLHAUS AND VARDOULAKIS [73]; STEINMANN [89]; STEINMANN AND WILLAM [90]), gradient theories (gradient plasticity) (GERMAIN [34]; MÜHLHAUS AND AIFANTIS [71]) and integral continua (non-local plasticity) should be mentioned. For an overview see also (BAŽANT AND GAMBAROVA [7]; ERINGEN AND KAFADAR [30]; MÜHLHAUS [70]).

Discontinuous Modeling of Granular Media

A different approach to model granular materials are discontinuous models which treat the particles in a direct, discrete way (ALLEN AND TILDESLEY [1]; BASHIR AND GODDARD [6]; CUNDALL AND HART [22]). Examples of this approach are the "discrete element method" (DEM) or "molecular dynamics" (MD). This discrete way allows to take care of details like particle shape and material, size distribution, friction or cohesion of the granular material. The basic idea is to capture these properties by the interactions at a contact between two particles. These interaction laws are modeled with linear or non-linear springs in a direction normal and tangential to the contact plane. In order to describe, e.g. repulsive forces, rotations or dissipation the springs have to be chosen carefully by means of form, size and material laws. Then the equations of motion of the particles are solved with an explicit integration scheme like the VERLET algorithm (VERLET [104]). The advantages of particle based methods are: All forces, velocities and rotations of every single grain are known at every point in time. Thus the simulation provides at least the same information as the experiment. In contrast to continuum models the granular structure and thus a natural length scale is implicitly included by the formalism. Shear bands and cracks show up on the particle scale. However, the exact formulation of the interaction laws, the meaning of some of the parameters therein and the relevance of most of the details is still unsolved. Hopefully, as indicated by some research,

some details are not important – and thus negligible. To overcome this disadvantage a comparison between actual experiments and simulations has to be performed to calibrate the parameters and to validate the results of the simulation to allow, finally, for predictive results.

Micro-Macro Transition

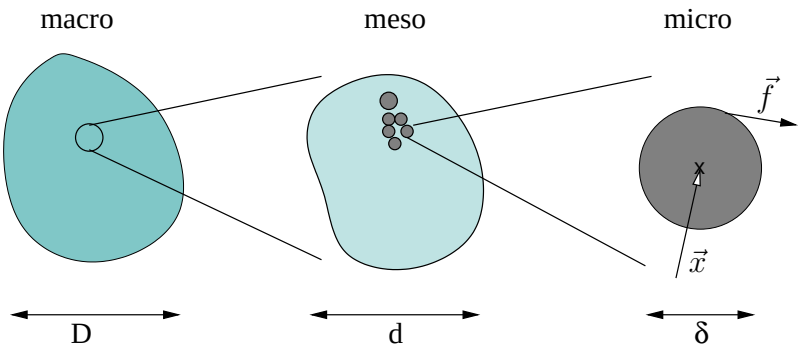

Fig. 2.1: *The different scales a granular media might be looked at. From the left: On the macro scale a block of granular media is treated as one unit. On a mesoscopic scale one already takes care of the multi body nature of granulates, while on the microscopic scale the behavior of every single grain is dealt with.*

Quantities like the velocity which are intrinsically available in the simulation are relatively easy to compare to experimental data, but for example for the stress tensor this task is not as straightforward. Such quantities have to be calculated indirectly from quantities directly accessible. Moreover, in most experiments the quantities are not measured for the single grains, but for a bulk of particles. Thus a comparison between simulation and experiment necessitates a formalism how to derive an averaged, "macroscopic" quantity from the "microscopic" quantities of the single grains. To accomplish this *homogenization* process the physical properties of the particles have to be averaged over a region of the granulate including a sufficiently large number of grains. If the result of the averaging is statistically representative the averaging volume is called a *representative elementary volume* (REV). Within REV the local inhomogeneities on the micro-scale are averaged away but the size of the REV is still small enough to account for global inhomogeneities on the macro-scale. These three different length scales are shown in Fig. 2.1. On the right side the micro-scale is defined by the diameter δ

of a characteristic particle. The dimension of the REV is denoted by d and the system size is given by D. In order to derive a consistent REV a scale separation

$$\delta \ll d \ll D \tag{2.1}$$

has to exist but should never be taken for granted.

Provided that scale separation holds, different averaging techniques can be applied to derive homogenized quantities characterizing the overall behavior of the assembly. A key to the understanding of the behavior of granular materials is the stress-strain relationship. Therefore, the definition of the macroscopic stress tensor has been studied intensively (CHRISTOFFERSON ET AL. [18]; ROTHENBURG AND SELVADURAI [83]) and might now be considered as well established (BAGI [4]; CHANG [17]; KRUYT AND ROTHENBURG [48]; LÄTZEL ET AL. [50]; LUDING ET AL. [58]). However, the description of a granular material also necessitates a definition of the strain tensor. Various studies have been dedicated to the derivation of explicit expressions for the overall strain tensor (BAGI [4]; CAMBOU AND DUBUJET [15]; DEDECKER ET AL. [26]; KRUYT AND ROTHENBURG [47]) in order to obtain macroscopic constitutive moduli (CAMBOU ET AL. [14]; CHAMBON ET AL. [16]; LIAO ET AL. [51]).

With the derivation of the constitutive moduli the circle closes. This moduli like YOUNGs modulus or the shear resistance may now be inserted into a continuous model and the results of this macroscopic models have then again to be validated with either experiments or simulations. For a better understanding of granular materials all scales of the granulate prove to be important: the interactions between the single grains in a simulation, the stress-strain curves in an experiment in a laboratory, and also the application of a continuum model on for example the rings of Saturn.

2.1 Overview

The aim of this thesis is twofold. On the one hand, a DEM is carried out and compared with an experiment. On the other hand, a micro-macro transition is developed and applied, leading to insights related to constitutive models for continuum theories. These two goals reflect also in the structure of this

thesis. Chapters 3 - 6 deal with the setup and the comparison of the simulation and the experiment, while Chapters 7 - 9 develop the micro-macro transition and compare the results to a recently presented, micropolar continuum model.

After this introduction part one starts with Chapter 3 by presenting the setup of the simulation and the experiment. A motivation for the use of the Couette shear device is given, as well as an overview of the literature on Couette devices. The dimensions of the system and the particles confined in the cell are shown and the way of preparing the system is outlined. Interspersed in this first section the differences between the physical system and the simulation are pointed out.

For the simulation of the system a MD simulation is used. Chapter 4 describes how this simulation method works and briefly outlines the algorithms used. The integration method and a speed up method for the neighborhood search, namely the linked-cell algorithm, are recalled in this chapter. Since the interaction forces between the particles play a significant role in the simulation of granular media, the necessary laws and their implementation are provided. Forces in the normal direction at a contact point are dealt with as well as tangential forces.

In order to compare the results of the simulation to experiments and to move towards a continuum description of the system, a consistent way of obtaining various quantities has to be developed. This averaging formalism is presented in Chapter 5 and the use of the formalism is demonstrated by computing the local density profile and the velocity profile in the shear cell.

The simulation results are compared to the experimental data in Chapter 6. An initial, homogeneous density becomes radially non-uniform as a consequence of shear induced dilatancy, for both experiment and simulation. The investigation of this shear zone shows good quantitative agreement between experiment and simulation. Special attention is drawn to the kinematic properties of the device such as radial and angular velocities and the spin of the particles. Profile as well as distribution data are compared and the quantitative agreement/disagreement is discussed and possible reasons are given.

Because of the good agreement the simulation is used to gain further insights on quantities not available from the experiment. These quantities are useful in order to explore granular media by means of a continuum theory.

Part two starts with Chapter 7 by recalling the classical continuum theory. The chapter continues by providing the formalism how macroscopic quantities are obtained. Even if not a quantity of the classical continuum theory the fabric tensor is introduced. The fabric tensor describes the local structure of the granulate to some extent and therefore is a measure for the anisotropy of the system. It is also used in the definition of the stress and strain tensors. Finally, these tensors are used to compute the macroscopic moduli, namely the Young's and the shear modulus which we use to develop a new constitutive model relating the stress with the deformations and the structure inside a granular assembly.

Due to the ability of the single grains to rotate freely, the classical continuum theory has to be extended. Therefore, a COSSERAT type theory is introduced in Chapter 8. The related macroscopic quantities of the theory are calculated from the simulation and a new modulus, the torque resistance is calculated.

Chapter 9 finally compares the simulation results with a recently presented micropolar continuum model involving the previously discussed ideas and a flow rule as an additional ingredient.

The thesis closes with a summary and an outlook of the work in Chapter 10.

3 The Model System

The behavior of granular materials e.g. in landslides or avalanches seems to be that of an ordinary fluid. But when exposed to shear stresses the reactions are quite different. Rather than being deformed uniformly, materials such as dry sand or cohesionless powders develop shear bands, narrow zones of large relative particle motion, with essentially rigid adjacent regions. This shear bands mark areas of flow, material failure, and therefore, energy dissipation, making them important in various industrial, civil engineering and geophysical processes.

However, detailed (three-dimensional) measurements on the physics within a shear band, including the degree of particle rotation and inter-particle slip, are lacking. Similarly, very little is known about the dependency of the grains movement in densely packed material on the microscopic properties of the particles. Most of the experiments on granular shearing have primarily focused on the force properties of the system (HOWELL ET AL. [42]; HOWELL [43]; HOWELL ET AL. [44]; MILLER ET AL. [64]; VEJE ET AL. [102, 103]). The kinematics of shear zones were explored only in a few experiments, and these involved using either inclined or vertical chutes (AZANZA ET AL. [3]; DRAKE [27]; NEDDERMAN AND LAOHAKUL [74]) or vibrated beds (LOSERT ET AL. [54]) involving also air flow between the particles.

The setup used in this study is a Couette shear device shown in Fig. 3.1.

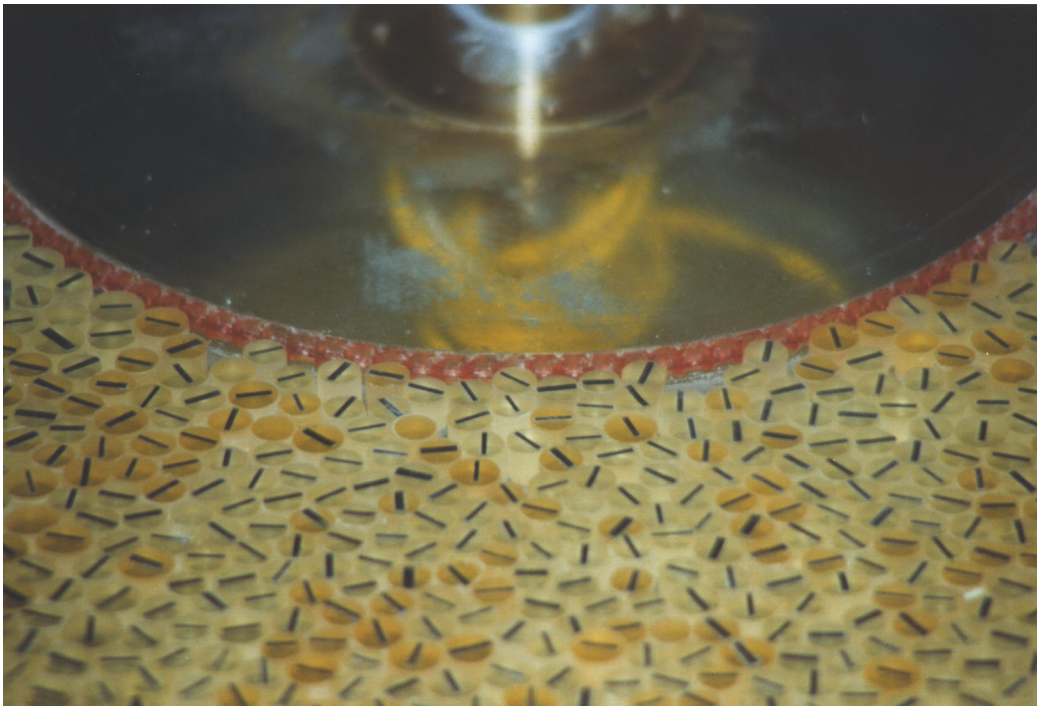

Fig. 3.1: *Plexiglas disks near the inner shearing wheel of the Couette shear device of the Behringer group. (Photo: USA, Durham, 1999, Marc Lätzel)*

In the physical system the granular material (disks) is confined between a stationary outer and a rotating inner cylinder, thus exposed to shear at the inner wall. As a consequence of the shear and the higher curvature at the inner wall a small shear band localizes at the inner cylinder, indicated e.g. by the velocity and spin profiles, which decay approximately exponentially away from the rotating wall. For that reason the Couette shear cell is used as a prototype system to have a closer look at the properties inside a shear band. To relate the simulation results to experiments, they are compared to the work of Dan Howell (HOWELL ET AL. [42]; HOWELL [43]; HOWELL ET AL. [44]) and differences in model-details are discussed.

In this chapter the history and motivation of this kind of shearing devices is presented before the setup of the physical system is introduced. We also show the preparation of the sample and point out the differences in the modeling between simulation and experiment.

3.1 Motivation and History

Shear devices are a well established tool for the study of the rheology of polymers, fluids, etc. and also for granular materials. They are used to determine the properties of granular materials experimentally, e.g. to test the usability of a type of sand for a specific task. Shearing tests are also performed to obtain the parameters to properly design industrial plants like silos or conveyors.

In principle, one can distinguish two groups of shear devices:

- Shear devices where measurements at the surface determine the full stress and strain situation inside the device. Examples for this type are the biaxial- and triaxial-compression-device.
- Shear devices in which a deformation at the boundaries of the granular material leads to a sliding of granular material inside the medium. In this kind of devices, e.g. the Jenike or the Couette shear device, it is not possible in general to deduce the traits of the shear zone from measurements at the boundaries.

There are three reasons for using a Couette shear cell in this work: First, we were able to check and calibrate our results with those of the experimental group of Prof. R. Behringer, Duke University (Durham, NC (USA)). Second, after some transient initial effects a (quasi) steady state of the system is reached, which allows taking measurements over a long time, i.e. time averaging can be carried out. And third, because of the symmetry of the device, also space averaging in the cylindrical geometry is possible.

Comparisons between experiments with a Couette apparatus and a continuum approach trace back to BOGDANOVA-BONTCHEVA AND LIPPMANN [11] in 1975. In order to model a two-dimensional system they were using a material consisting of parallel metal needles (Schneebeli material) with very weak frictional particle-particle interactions. However, in their work no quantitative measurements were performed. Instead, because of the observed spin of the particles a COSSERAT-type continuum theory was developed. In 1989 BUGGISCH AND LÖFFELMANN [13] also performed experiments on a Couette device focusing on the mixing properties of the

granulate. In his PhD thesis LÖFFELMANN [52] additionally examined the influence of the wall roughness and showed measurements of tangential velocities. Recently, apart from the work of VEJE ET AL. [101; 102] and HOWELL ET AL. [42; 43] to which will be referred in the next Sections, MUETH ET AL. [67; 68] did three dimensional experiments. Their apparatus was filled with mustard seeds (spherical) and poppy seeds (kidney-shaped). With a combination of magnetic resonance imaging, X-ray tomography and high-speed-video particle tracking they obtained the local steady state particle velocity, rotation and packing density in the Couette device. In contrast to the results of a 2D system the velocity is almost completely described by a Gaussian for aspherical particles. Another three dimensional experiment of a Couette cell was performed by BOCQUET and LOSERT ET AL. [10; 53]. The main focus of their work was on the fluctuations of the tangential velocity and on the shear forces. They also developed a locally Newtonian, continuum model of granular flow and compare it with the experimental results. The only simulations of a 2D Couette setup of which we are aware is that of ZERVOS ET AL. [109; 110]. In their work they addressed the problem of a 2D Couette shear device filled with Schneebeli material experimentally and with Contact-Dynamics simulations, focusing mainly on the dynamical features of the material. Different to our setup their experiment is not carried out under constant volume conditions, but constant confining pressure. ZERVOS ET AL. investigate the tangential velocity as well as the rotation of the grains and propose the use of a COSSERAT-type continuum model for the description of the granular material and compute the COSSERAT rotation (see Sect. 8.1). Unfortunately the process of experimental data acquisition does not allow immediate comparisons between simulation and experiment. So only qualitatively agreement could be found.

The thesis in hand was inspired by the work of VEJE ET AL. [101; 102] in Paris at the early nineties. In his diploma thesis SCHÖLLMANN [87] developed a first version of the simulation used and compared his results with the experiments (SCHÖLLMANN [88]). The code of this first version was reimplemented using the P3T-classes (P3T CLASS LIBRARIES [77]) developed at the ICA1.

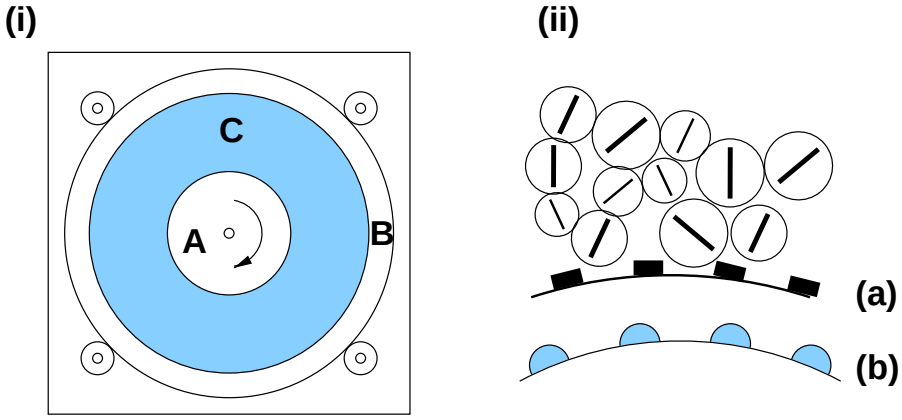

Fig. 3.2: **(i)** *schematic top view of the experimental setup.* **(ii)** *schematic drawing of the disks close to the shearing wheel.* **(a)***) experimental realization of the walls.* **(b)***) realization of the walls in the simulation.*

3.2 The Setup

In the simulation the granular material is sheared in a Couette geometry. This geometry was chosen in a way to match the experimental setup of VEJE ET AL. [102] and HOWELL [43] as closely as possible. Thus, the material is confined between two concentric rings, as sketched in Fig. 3.2. The inner shearing wheel (A) of radius $R_i = 10.32\,\mathrm{cm}$ is able to rotate, whereas the outer ring (B) of radius $R_o = 25.24\,\mathrm{cm}$ is stationary during the simulation, i.e. the simulation is carried out under *constant total volume* condition.[1]

In order to enhance the shearing between the granular material in the cell and the walls, where the actual energy input takes place, the walls have to be roughened. In the physical system this is done by coating the side of the wheel and the inner surface of the ring with plastic 'teeth' spaced $7\,\mathrm{mm}$ apart and $2\,\mathrm{mm}$ deep to enhance shearing (Fig. 3.2 (ii) (a)). For simplicity half disks of radius $a_{\mathrm{wall}} = 1.25\,\mathrm{mm}$ with a spacing of $2.5\,\mathrm{mm}$ are used in the simulation, as shown in the right part of Fig. 3.2.

The granular material in the experiment is made of a $6\,\mathrm{mm}$ thick trans-

[1] Although both the wheel and the outer ring could be used to shear (SCHÖLLMANN [88]), we will focus on shearing with the inner wheel only.

Tab. 3.1: *Microscopic material parameters of the model.*

Property	Values
radius of outer wall R_o	0.2524 m
radius of inner wall R_i	0.1032 m
radius a_{small}, mass m_{small}	3.71 mm, 0.275 g
radius a_{large}, mass m_{large}	4.495 mm, 0.490 g
reference diameter $\tilde{d}$	7.4 mm
material density ϱ^p	1060 kg/m^3
wall-particle radius a_{wall},	1.25 mm
system/disk-height h	6 mm

parent photo-elastic polymer which has a nominal Young's modulus of $Y = 4.8\,\text{MPa}$. Therefore, the disks are much softer than the material of the wheel and the ring ($Y \approx 3\,\text{GPa}$).

The disks are confined to a plane between these rings and two smooth horizontal Plexiglas sheets. The surfaces of the Plexiglas sheets are lubricated with a fine dusting of baking powder.[2] Even with this precaution, there is still some remaining friction between the disks and the sheet, which is also taken into account in the simulation, see Sect. 4.2.4. However, the typical friction force between the particles and the bottom sheet is about an order of magnitude smaller than the typical force in a stress chain, so its influence on the material properties like, e.g. the stress, should be small.

When compacting a sample of mono-disperse particles the grains crystallize, i.e. regular grain patterns form in the sample. These patterns, although helping in the formation of very stable arches that prevent deformation, make mono-disperse samples unsuitable for the shearing device where one is interested in the dynamics and reorganization of the particles. Therefore, a bi-disperse size distribution is used in the experiment as well as in the simulations, with roughly 400 larger and 2500 smaller disks, i.e. about 86% of the total number of particles are smaller disks. The bimodal distribution limits the formation of hexagonally ordered regions over large scales – even though the presently used width of the size distribution might be a little too small in order to avoid ordering effects (see also Sect.7.2.4). According to a recent paper of LUDING [56] our distribution will still lead to the formation

[2] Another way was chosen by LOSERT ET AL. [53]. They used a continuous upwards air flow, to suppress friction with the bottom plate in their experiment.

of ordered structures.

One concern is that the disks would segregate by size. However, we have not observed any strong tendency for this to happen over the course of a typical experiment. We used small particles of radius $a_{\mathrm{small}} = 3.71\,\mathrm{mm}$ and large particles of radius $a_{\mathrm{large}} = 4.495\,\mathrm{mm}$. Throughout this thesis the diameter $\tilde{d} = d_{\mathrm{small}}$ is used as a characteristic length scale.

The packing fraction $\bar{\nu}$ (fractional area occupied by disks) is varied over the range $0.789 \leq \bar{\nu} \leq 0.828$. As we vary $\bar{\nu}$ we maintain the ratio of small to large grains almost fixed.[3]

A variation of the angular velocity, Ω, of the inner wheel over the range $0.0029\,\mathrm{s}^{-1} \leq \Omega \leq 0.09\,\mathrm{s}^{-1}$ shows rate independence in the experiments. A few simulations with $0.01\,\mathrm{s}^{-1} \leq \Omega \leq 1.0\,\mathrm{s}^{-1}$ showed clear rate independency at least for the slower shearing rates $\Omega \leq 0.1\,\mathrm{s}^{-1}$.

Although the system is a representation of a two-dimensional model, the physical particles have a height of $h = 6\,\mathrm{mm}$ which is taken into account in the simulation as well, so that all properties like mass, stress, etc. are provided in their natural units.

3.3 Preparation of the Sample

The creation of a sample is a relatively simple process: In the experiments, the particles are put into the shearing device by hand, one by one until the desired number and density is reached.

The dense packing of grains is an other topic in the research of granular media (NICODEMI ET AL. [75]; NOWAK ET AL. [76]), involving a very slow process for the packing and is out of the scope of this thesis. Therefore, the simulations are started in a dilute state with an extended outer ring $R_{\mathrm{prepare}} > R_o = 25.24\,\mathrm{cm}$, and the inner ring already rotates counterclockwise with constant angular velocity. The particles are created in the sample's area on a regular, triangular lattice with a random velocity in order to pre-

[3] Note that the effect of the wall particles for the calculation of the global packing fraction is very small. The small particles glued to the wall are counted with half their volume only, and thus contribute with $\bar{\nu}_{\mathrm{wall}} = 0.0047$ to $\bar{\nu}$.

Tab. 3.2: *Details of the simulation runs provided in this study. Mentioned are those particle numbers for which data were available in both experiment and simulation. The horizontal lines in the last column mark the transition between the sub-critical (the blocked) range of density with the shear flow regime.*

Global Volume Fraction $\bar{\nu}$	Number of Particles small	large	Flow Behavior
0.789	2462	404	
0.791	2469	405	sub-critical
0.793	2476	406	————
0.796	2483	407	
0.798	2490	408	
0.800	2498	409	
0.800	2511	400	
0.802	2520	399	
0.804	2511	410	shear flow
0.805	2524	404	
0.807	2518	412	
0.807	2545	394	
0.809	2525	414	————-
0.810	2538	407	————-
0.811	2555	399	
0.819	2560	418	blocked
0.828	2588	422	

vent crystallization.[4] The created sample, though, is loose and grains are not in contact with each other in general. The particles are initialized with a random velocity in order to prevent crystallization. Afterwards, the outer wall shrinks up to the desired radius of $R_o = 25.24\,\mathrm{cm}$.

Before collecting the data the inner ring ran for about 20 rotations in the experiment. In the simulation, however, the preparation had to be limited in order to reduce the comparatively long computation time. The simulations are prepared for about 5 rotation periods, because a few runs with preparation times of up to ten periods of rotation did *not* show clearly further relaxation effects. However, the still much longer relaxation time of tens

[4] The triangular lattice provides that the particles do not overlap with existing grains or the boundaries. However, the sample remembers the lattice due to the chosen distribution of the particle sizes, especially at the boundaries. This effect will be discussed in Section 7.2.

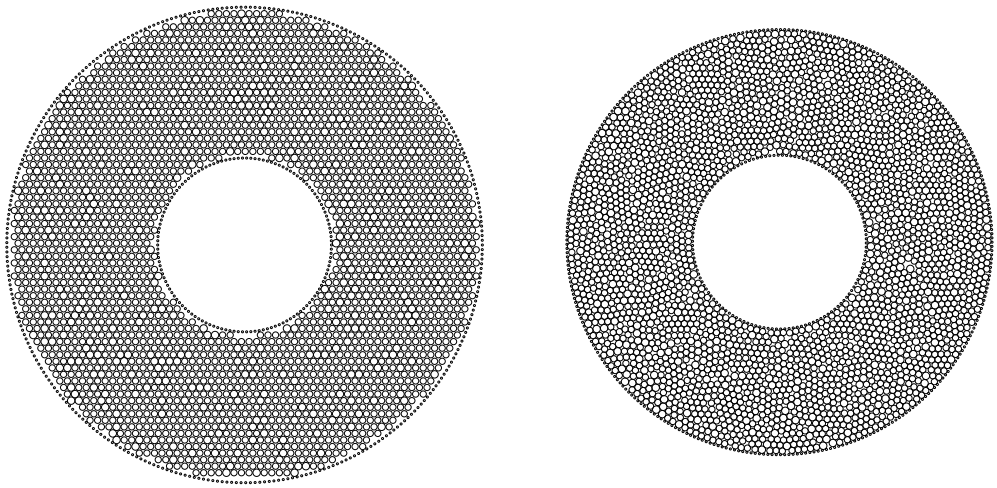

(a) Initial configuration.

(b) Configuration after shrinking of the outer wall.

Fig. 3.3: *The Figure demonstrates the preparation of the sample. In the initial configuration the particles are placed on a triangular lattice, which is then compressed until the desired radius is reached.*

to hundreds of periods as used in the experiment was not reached, so that long time relaxation effects can not be ruled out by the simulation results presented here.

3.4 Differences between Experiment and Simulation

Although the simulation was set up in a way to resemble the experiment as closely as possible, there still remain some seemingly modest differences, some of which can not be overcome without substantially re-modeling.

First, the inner ring in the original apparatus is not perfectly round, but there is a small bump at the region where the strip forming the roughness of the inner wheel overlaps. Especially in the case of low packing fractions, where the particles are easily moved away from the inner wheel, this results in an intermittent behavior, because even if the inner wall is not in contact

with the granular material, in general, the small bump might sometimes be. Thus the radius of the inner wall is in effect a little larger than the ideal R_i used in the simulations.

The second difference seems to be more crucial. In the experiment the bottom plate is coated with backing powder in order to reduce friction. The amount of remaining friction is hard to determine because the baking powder is not uniformly distributed and snow-plug (stack of powder) effects might occur. Additionally, the friction depends on the number of particles in a cluster moved over the powder. Therefore, the friction of the simulation might be smaller than in the actual experiment thus allowing more dynamics of the particles.

As a third difference it should be mentioned that the grains in the experiment are real three dimensional bodies and are able to slightly tilt out of plane of observation (parallel to the bottom). A degree of freedom which is not allowed in the simulation. This difference is connected with possibly increased tangential forces due to increased, artificial, normal forces.

3.5 Conclusion

In this chapter we reasoned the use of a Couette shear device as an experimental realization of a quasi infinite media. In this kind of apparatus a quasi steady state develops and might be studied for long times. Therefore, the Couette shear cell has attract many scientist to perform experiments and simulations on granular media.

We introduced the geometrical setup of our apparatus and showed the physical values of the granulate used in the experiment. Moreover, we outlined the preparation procedure for the experiment and the simulation and pointed out the differences between simulation and experiment.

In Chapter 4 we will describe the simulation model in detail. Due to the importance of the interaction laws between the single particles, special attention will be drawn on these force laws.

4 The Simulation Method

Because of its wide variety of effects, granular media have been and are still attracting considerable attention both from the experimental, and the theoretical side. In the last decade, as a third way to study granular materials, the computer simulations, have emerged due to the considerable increase in computing power. The advantage of such a micro-mechanical simulation is that for all the grains and at every instant in time, the displacements, rotations and acting contact forces are known. Therefore, it offers the possibility of analyzing and visualizing the behavior inside the medium. Additionally to most experiments simulations provide access to the state of inter-granular forces (TSOUNGUI ET AL. [99]) which is a key quantity to the understanding of granular media.

The challenge of simulations is to develop techniques that are, on the one hand, giving accurate enough results to be compared to physical experiments, but on the other hand, are of sufficient numerical efficiency to study "large" systems in terms of particle numbers and boundary conditions, system sizes and "long" times with respect to intrinsic time scales like e.g. L/v, the time information needs to propagate from one end of the system to the other, with a typical velocity v.

Many different methods are used to simulate granular materials, for an overview see HERRMANN AND LUDING [40]. One way to characterize the two major different simulation approaches is the way the material is de-

scribed: as a continuum or as discrete particles. The aim of this study is to start with the properties of the discrete particles and to end up with a continuous description, eventually. Therefore, a discrete element method (DEM) is chosen for the simulations.

The method is described in the first section of this chapter. As will be pointed out there, the implementation of the forces plays a crucial role in how accurately the simulation mimics an experiment. We will present the force laws used throughout our simulations in Section 4.2. In the last section of this chapter we comment on the use of non-linear force laws to simulate the behavior of a granular medium.

4.1 Molecular Dynamics

Molecular Dynamics (MD) simulations are one of the oldest computer-simulation techniques. They were primarily designed for the simulation of atoms and molecules as a new approach to the understanding of "many particle" systems. Those systems could only be tackled in a statistical way, since detailed properties of every particle were not available experimentally. However, MD simulations integrate the equations of motion for each particle, thus enabling the knowledge of e.g. the velocities or trajectories, of a discrete atom. Especially in system with highly fluctuating quantities most experimental measurements smear out a quantity over a certain region, thus averaging away the details.

A MD simulation is performed as follows. First an initial configuration of a physical system is created, i.e. every particle in the system possesses at least a position and a velocity vector, as well as an angular velocity. Afterwards, the NEWTONian equations of motion

$$\vec{f}_i = m_i \ddot{\vec{x}}_i \,, \qquad \vec{M}_i = J_i \dot{\omega}_i \tag{4.1}$$

are solved for every particle i, with mass m and acceleration $\ddot{\vec{x}}$ according to the acting forces $\vec{f}$ as well as for all particles with $\vec{M}$ the external moments, J the moment of inertia and $\dot{\omega}$ the angular acceleration, respectively. These equations are discretized and solved numerically to obtain the time

evolution of the N particle system.[1]Different ways to solve Eq. 4.1 are available, for an overview see e.g. (ALLEN AND TILDESLEY [1]; PRESS ET AL. [79]; RAPAPORT [82]). Each of these algorithms has its pros and cons in ways of speed, stability and accuracy. In this study we use a VERLET-Integration scheme (VERLET [104]) to solve the resulting finite differences equations. The VERLET integrator is derived from a TAYLOR expansion of $\vec{x}_i(t)$ up to second order:

$$\vec{x}_i(t \pm \Delta t) = \vec{x}_i(t) \pm \Delta t \dot{\vec{x}}_i(t) + \frac{1}{2}\Delta t^2 \ddot{\vec{x}}_i(t) \; . \tag{4.2}$$

Subsequent addition of $\vec{x}_i(t + \Delta t)$ and $\vec{x}_i(t - \Delta t)$ leads to the new position vector $\vec{x}_i(t + \Delta t)$ at time $t + \Delta t$:

$$\vec{x}_i(t + \Delta t) = 2\vec{x}_i(t) - \vec{x}_i(t - \Delta t) + \ddot{\vec{x}}_i(t)\Delta t^2 \; . \tag{4.3}$$

The time step Δt of the integration has to be chosen clearly smaller than a typical natural oscillation of a contact (LUDING [55]; LUDING ET AL. [57]). A ratio of $1 : 50$ proved to give satisfying results. Different integration schemes do not lead to a different outcome of our simulation, as shown by (SCHÖLLMANN [87]).

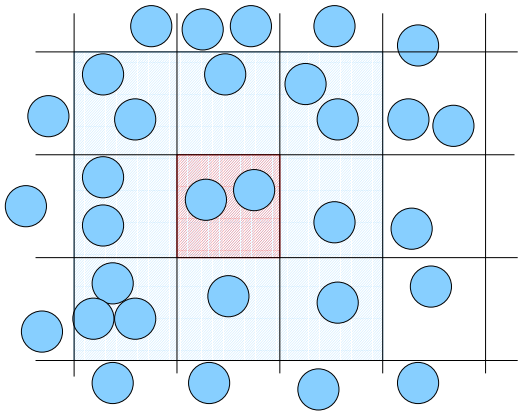

Fig. 4.1: *Linked-cell algorithm for molecular dynamic simulations. The search for interaction partners is limited to the actual cell (dark gray) and its neighbors (light gray).*

During the integration process the most time consuming part is the calculation of the interactions between the particles. This calculation results in a

[1] Note that solving of the equations of motion is a fully deterministic process. Randomness enters the system only via different initial conditions.

$\mathcal{O}(N^2)$ loop over all possible pairs, if N particles are interacting with each other. For short range forces, as discussed here, one can speed up this calculations by using so called *linked cell* structures (ALLEN AND TILDESLEY [1]), resulting in an $\mathcal{O}(N)$ algorithm. In the linked-cell algorithm the system is divided into cells of length L_c, where L_c is the so called cut-off length. If all interactions beyond this range are neglected, it is sufficient to look for interaction partners in the actual cell and the neighboring cells (see Fig. 4.1).

A more crucial point than the integration method used and the speed-up tricks in the MD simulation, is the implementation of the forces since those forces incorporate assumptions and simplifications. Forces, as e.g. gravity, electromagnetic forces are quite straightforward. The important particle-particle interactions are not known in general. Therefore, we will describe the force laws used in this study in detail in the following sections.

4.2 Force Laws

Even if the approach of a MD simulation is physically motivated, one cannot avoid to introduce phenomenological assumptions on the interaction forces. In this study only dry granular media are investigated, which implies the forces arising between the particles are only of short-range type. For (nearly) sphere shaped particles the forces acting at a contact between particles i and j can be decomposed into normal $\vec{f}_{ij}^{\,n}$ and tangential $\vec{f}_{ij}^{\,t}$ components

$$\vec{f}_{ij} = \vec{f}_{ij}^{\,n} + \vec{f}_{ij}^{\,t} \,, \tag{4.4}$$

with respect to the contact line (dashed line in Fig. 4.2).[2]

The behavior of an inelastic collision is modeled via the normal components and requires at least two terms; repulsion and some sort of dissipation. The repulsive force accounts for the excluded volume of the modeled grains and is active during the collision of the particles, acting normal to the contact line. The dissipative part of the force is modeled as a phenomenological damping in a way to represent linear viscoelastic behavior.

[2] In 3D the contact line becomes a contact plane. In the following only the 2D case is dealt with.

In addition to the normal forces there is a force parallel to the contact line, accounting for the friction between the particles.

In the following sections these forces are described in more detail according to their hierarchy in the complexity of their implementation. We start with the implementation of the normal forces, and advance to the more difficult tangential forces in Section 4.2.2. The different realizations of the forces in some cases lead to dramatic changes in the outcome of a simulation as shown in Section 4.2.3. Therefore, we will also comment on the limitations of the chosen interaction laws.

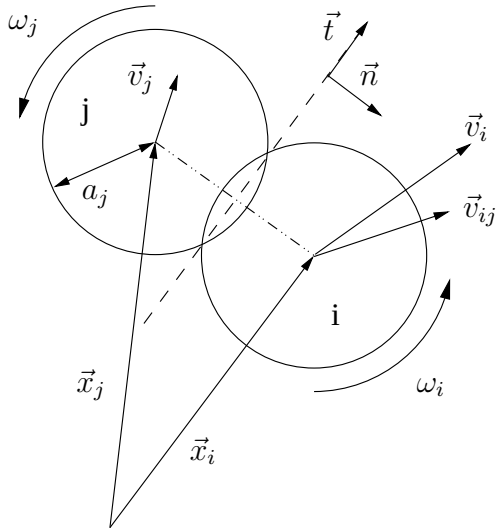

Fig. 4.2: *Definition of the quantities of particles i and j used for the description of the force laws.*

4.2.1 Normal Forces

When solving the equations of motion as described in Section 4.1, two grains may turn out to overlap due to the finite time step. This overlap is interpreted as the elastic deformation which occurs for particles under stress. However, in dry granular media particles only interact when they are in contact. Therefore, the overlap

$$\delta = (a_i + a_j) - (\vec{x}_i - \vec{x}_j) \cdot \vec{n} \tag{4.5}$$

of two particles is related to the interaction force between the two grains i and j.[3] The symbol '$\cdot$' denotes the scalar product of vectors or, more generally, the contraction of indices for each of two tensors. $\vec{n} = (\vec{x}_i - \vec{x}_j)/|\vec{x}_i - \vec{x}_j|$ is the unit vector pointing from j to i. The radius and the position of particle i are denoted by a_i and $\vec{x}_i$, respectively, as shown in Figure 4.2.

The first contribution to the force acting on particle i from particle j is an elastic repulsive force

$$\vec{f}^{\,n}_{\text{el}} = k^n \delta \vec{n} \,, \tag{4.6}$$

proportional to the overlap and a spring constant k^n proportional to the material's modulus of elasticity with units $[N/m]$. Since we are interested in disks rather than spheres, we use a linear spring that follows HOOKE's law, whereas in the case of elastic spheres, the Hertz contact law would be more appropriate (HERTZ [41]; LANDAU AND LIFSHITZ [49]; SCHÄFER ET AL. [86]).

One of the key features of granular materials is the dissipation of energy due to inter-particle collisions i.e. the transfer of kinetic energy into internal degrees of freedom of a particle and finally into heat. In order to introduce dissipation into the system, one assumes a viscous damping proportional to the relative velocity in the normal direction

$$\vec{f}^{\,n}_{\text{diss}} = \gamma^n \vec{v}^{\,n} \,, \tag{4.7}$$

where $\vec{v}^{\,n} = -(\vec{v}_{ij} \cdot \vec{n})\vec{n} = -((\vec{v}_i - \vec{v}_j) \cdot \vec{n})\vec{n}$. The proportionality coefficient γ^n is of pure phenomenological origin and has to be chosen in a way to assemble the desired dissipation.

The dissipation is quantified by the normal restitution coefficient $e^{\,n}$ which is defined as the ratio of the post- and the pre-collisional velocities in a head on collision between two particles

$$e^{\,n} = -v_f^n / v_i^n \;\in [0, 1] \,. \tag{4.8}$$

Here the subscripts i and f refer to the pre-collisional (*initial*) and to the post-collisional (*final*) normal velocity, respectively. The coefficient of normal restitution equals 0 for a completely inelastic collision and becomes 1 for a perfectly elastic collision.

[3] Note that the evaluation of the inter-particle forces based on the overlap may not be sufficient to account for the nonlinear stress distribution inside the particles. Consequently, our results presented below are of the same quality as this basic assumption.

The combination of the linear elastic part of Eq. 4.5 and the dissipative part of Eq. 4.7 is know as *linear spring dashpot* model and reads as

$$\vec{f}^{\,n} = \vec{f}^{\,n}_{\mathrm{el}} + \vec{f}^{\,n}_{\mathrm{diss}} = k^n \delta\vec{n} + \gamma^n \vec{v}^{\,n} \; . \tag{4.9}$$

The force law leads to a constant e^n for different velocities and is valid if the range of velocities in a simulation is not too broad. Otherwise, one has to think of force laws accounting for a normal restitution coefficient which falls off like $(v^n)^{-1/4}$ with increasing impact velocity (SCHÄFER ET AL. [86]).

4.2.2 Tangential Forces

As mentioned previously the normal force is accompanied by a frictional force tangential to the contact line. This frictional force prevents e.g. a sand pile from deliquescing to a plain, even though this would be the more favorable energy state. In this section the implementation of the tangential forces is described.

Tangential forces are active at contacts where the relative tangential velocity of the particles $\vec{v}^{\,t}$ is non-zero, or was non-zero during the history of the contact. The relative tangential velocity is obtained from the relative velocity of two particles i and j at a contact via

$$\begin{aligned} \vec{v}^{\,t} &= \vec{v}_{ij} - \vec{v}^{\,n} \; , & (4.10)\\ &= \vec{v}_{ij} - (\vec{v}_{ij} \cdot \vec{n})\vec{n} \; , & (4.11) \end{aligned}$$

with the relative velocity

$$\vec{v}_{ij} = (\vec{v}_i - \vec{v}_j) - (\omega_i a_i + \omega_j a_j) \times \vec{n} \; , \tag{4.12}$$

where ω_i denotes the angular velocity of particle i (see also Fig. 4.2). The relative tangential velocity is also used to define the tangential unit vector:

$$\vec{t} = \frac{\vec{v}^{\,t}}{|\vec{v}^{\,t}|} \; , \tag{4.13}$$

in a somewhat different way from the frequently used rotation of $\vec{n}$ by 90°.

Coulomb Friction

In general, tangential friction forces are implemented proportional to the normal force according to COULOMB [20]:

$$f^t_{\text{static}} \leq \mu_s f^n \qquad v^t = 0\,, \tag{4.14}$$

$$f^t_{\text{dynamic}} = \mu_d f^n \qquad v^t \neq 0\,. \tag{4.15}$$

Here μ_s and μ_d are the coefficients of static and dynamic friction, respectively. Additionally to the dynamic (sliding) and the static friction there exist different kinds of friction forces like rolling friction. Those forces are not accounted for in this study, because in most cases $\mu_s > \mu_d \gg \mu_r$, so the coefficients for static friction and sliding friction are assumed to be equal ($\mu_d = \mu_s = \mu_C$), whereas the rolling coefficient is set to zero ($\mu_r = 0$).

The simplest implementation of a COULOMB friction force is

$$\vec{f}^t_{\text{Coulomb}} = -\mu_C |\vec{f}^n| \vec{t}\,. \tag{4.16}$$

However, this setup accounts only for the dynamic friction of Eq. 4.15. The static part in Eq. 4.14 is more complex and is described in the following.

Static Friction

The difficulty of handling static friction originates in the discontinuity of Eq. 4.16 for $\vec{v}^t \to 0$. To overcome this difficulty one introduces a viscous force

$$\vec{f}^t_{\text{visc}} = -\gamma^t \vec{v}^t \tag{4.17}$$

and thus regularizes Eq. 4.15. Yet, there is no real phenomenological equivalent of a viscous force in a collision of two bodies. But coupling Eqs. 4.16 and 4.17 by taking the minimum leads to a widely used tangential friction force which is a good trade-off between reality and implementation ability

$$\vec{f}^t = -\min\left(\gamma^t \left|\vec{v}^t\right|, \mu_C \left|\vec{f}^n\right|\right) \vec{t}\,. \tag{4.18}$$

The parameter γ^t is auxiliary, and should be set large enough to ensure that on the one hand, the singularity vanishes and on the other hand, the deviations from Eq. 4.15 are still small.

Even often used, there are two problems with force law 4.18: First, it does not allow the reversal of v^t (SCHÄFER ET AL. [86]) although this is observed

in experiments (FOERSTER ET AL. [32]). Second, it yields $f^t(v^t = 0) = 0$, which means that such a contact is not able to bear any load at rest, and hence, e.g. a sand pile under gravity would collapse. Therefore, in the next paragraph another force law is given, overcoming this intricacy.

Tangential Spring

Already in 1979 CUNDALL AND STRACK [23] tried to implement a force law able to allow for the reversal of v^t by introducing a tangential spring. At the moment when two particles get into contact (t_0) one assigns a "virtual" spring with length zero to this contact, connecting the contact points. During the time the particles stay in contact, the spring is stretched according to

$$\xi = \left(\int_{t_0}^{t} \vec{v}^t(t') \, dt' \right) \cdot \vec{t} \, . \tag{4.19}$$

Note that due to its definition ξ can either be positive or negative so that $\vec{\xi} = \xi \vec{t}$ can be anti-parallel to $\vec{t}$. With this CUNDALL-STRACK spring the tangential force reads as

$$\vec{f^t} = -\min \left(k^t \, \xi, \mu_C \, |\vec{f^n}| \right) \frac{\vec{\xi}}{|\vec{\xi}|} \, , \tag{4.20}$$

where k^t is the stiffness of that spring. In contrast to Eq. 4.18 where the Coulomb force acts in the direction $-\vec{t}$ against the relative tangential velocity $\vec{v}^t$, here it works against the elongation of the spring thus enabling the reversal of the tangential velocity.

In order to account for sliding at the contact the elongation of the tangential spring has to be limited by the relation $k^t \xi_{\max} = \mu_C f^n$.

This force scheme is widely used in the literature (e.g. (MATUTTIS ET AL. [61])) and was shown to produce quite realistic results for collisions (BRENDEL AND DIPPEL [12]; RADJAI ET AL. [80]). However, there are some cases where this force law may lead to unphysical behavior. In Eq. 4.19 one assumes that $\vec{\xi}$ is parallel to $\vec{t}$. This may be wrong for long lasting contacts, as they occur in dense granular media. Another drawback of force law 4.20 is the lack of damping. In the following section both difficulties are addressed.

Extensions

For long lasting contacts the frame of reference of the contact might change while the particles are in contact thus $\vec{\xi}$ is no longer parallel to $\vec{t}$. Therefore, a remapping of $\vec{\xi}$ into the actual tangential plane is used

$$\vec{\xi} = \vec{\xi}' - \vec{n}(\vec{n} \cdot \vec{\xi}') \,, \tag{4.21}$$

where $\vec{\xi}'$ is the old spring from the last iteration. This action is only relevant for an already existing spring, if the contact just formed, the tangential spring length is zero anyway.

One property, which force scheme 4.20 inherited from law 4.18 is the absence of any damping. This may become inconvenient for example if a particle in the shear cell would be kicked, it would not exactly come to rest but would persist to vibrate with a small amplitude. An obvious solution to overcome these oscillations is to add a viscous damping like Eq. 4.17 to Eq. 4.20. Such an extension was proposed by BRENDEL AND DIPPEL [12].

Unfortunately, this extended scheme, including the damping, cannot be written in a simple form like 4.20 anymore. Instead, the implementation requires first a test force

$$\vec{f}^{*} = -k^t \vec{\xi} - \gamma^t \vec{v}^t, \tag{4.22}$$

and second, the comparison of its absolute value to the threshold $\mu_C f^n$. In the case of a too large test force, one gets

$$\vec{f}^{\,t} = \mu_C f^n \frac{\vec{\xi}}{|\vec{\xi}|} \quad , \quad \vec{\xi} = -\frac{\mu_C}{k^t} f^n \frac{\vec{\xi}}{|\vec{\xi}|} \qquad \text{for } |\vec{f}^{\,t*}| > \mu_C f^n \,. \tag{4.23}$$

While for a test force smaller than the Coulomb threshold, one has

$$\vec{f}^{\,t} = \vec{f}^{*} \quad , \quad \vec{\xi} = \vec{\xi} + \vec{v}^t \, dt \qquad \text{for } |\vec{f}^{\,t*}| \leq \mu_C f^n \,. \tag{4.24}$$

The combination of this force law with the distinction between μ_s and μ_d is straightforward to implement, but not used in this work. Thus finally the tangential force in short notation reads as follows:

$$\vec{f}^{\,t} = -\min\left(\mu_C f^{\,n}, |\vec{f}^{\,t*}|\right) \vec{f}^{\,t*} / |vec f^{\,t*}| \,. \tag{4.25}$$

The exact implementation of Eq. 4.24 is of lower importance in collision dominated systems, but in dense sheared systems like in this study, it should be used, especially if one is interested in quantities such as the force distributions in the quasi-static case (*cf.* (RADJAI ET AL. [81])).

4.2.3 Effect of Different Tangential Force Laws

In order to illustrate the influence of the different tangential force laws on a two particle collision a series of head on collisions with different initial spin and different force laws was performed. In Fig. 4.3 the dimensionless final tangential velocity

$$\Psi^f = (v^t)^f/(v^n)^i \,, \tag{4.26}$$

defined as the ratio of the final relative tangential velocity of the two particles and the initial relative normal velocity is plotted as a function of the dimensionless initial tangential velocity Ψ^i. The effects of the different tangential force laws are demonstrated in Fig. 4.3 namely only the tangential spring resembles the reversal of the tangential velocity as in the experiments of e.g. FOERSTER ET AL. [32].

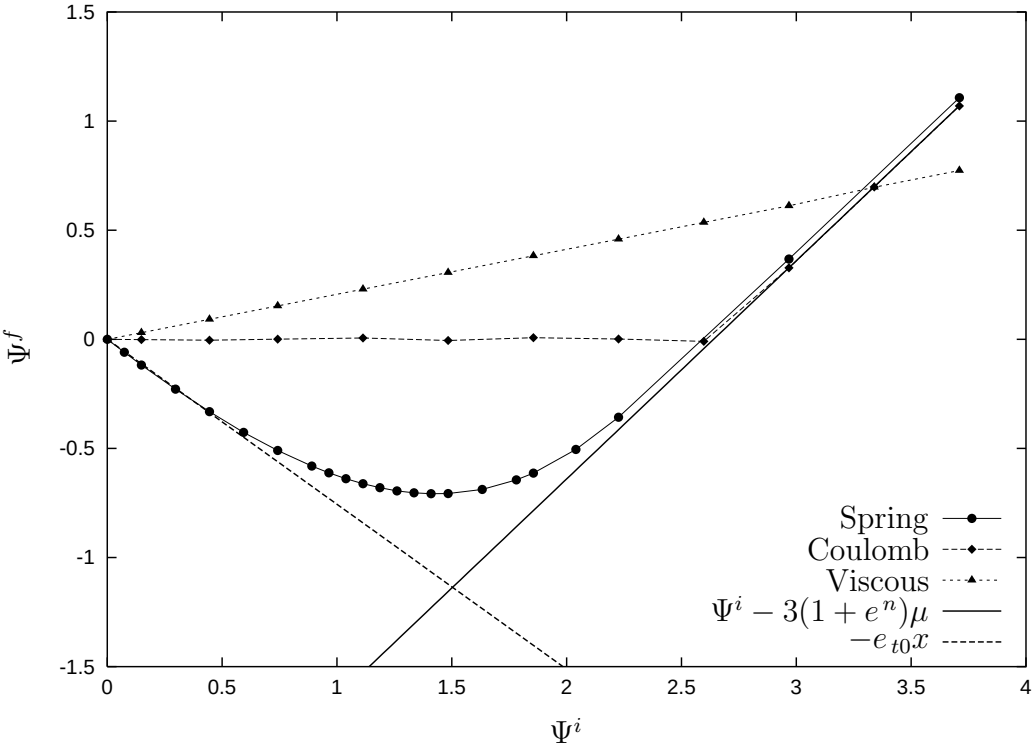

Fig. 4.3: *$\Psi^f = (v^t)^f/(v^n)^i$ vs. $\Psi^i = (v^t)^i/(v^n)^i$ for different tangential forces described in the text. The triangles denote the viscous force of Eq. 4.17, the diamonds refer to the Coulomb force of Eq. 4.16, whereas the circles represent the tangential spring without damping of Eq. 4.20. The lines give the analytic asymptotes according to* LUDING *[55].*

4.2.4 Bottom Forces

In order to account for the interaction of the particles with the bottom plate an additional bottom friction is implemented. The bottom friction acts both on the rotational and the translational degrees of freedom. In the model used throughout this work the bottom force is modeled analogously to the tangential friction forces 4.24 as a spring model. In short notation this reads:

$$\vec{f}^{\,b} = -\min(\mu_b|\vec{f}^{\,n}|, |\vec{f}^{\,b*}|)\frac{\vec{f}^{\,b*}}{|\vec{f}^{\,b*}|} \,, \tag{4.27}$$

where $\vec{f}^{\,b*}$ follows the rules described for the extensions of the tangential spring.

For the damping of rotations of the disks due to bottom friction a phenomenological approach is used. Again a test force

$$f^{\,M*} = -\mathrm{sgn}(\omega)\tau^{\,M}|\vec{f}^{\,b*}| - \gamma^b \omega r \,, \tag{4.28}$$

has to be implemented. The parameter $\tau^{\,M}$ is of purely phenomenological origin and is adjusted in a way that the first and the last term of Eq. 4.28 are of the same order. The applied torque reads as:

$$M = -\mathrm{sgn}(f^{\,M*})\min\left(\mu_b|\vec{f}^{\,n}|, |f^{\,M*}|\right)\frac{2}{3}r \,. \tag{4.29}$$

Note that the term $\frac{2}{3}r$ stems from the integration of the force over the surface of the disk.

Recently, FARKAS ET AL. [31] started to investigate the relationship between rolling, sliding and the interaction with a surface. The results of these experiments might lead to a more physical implementation of the body forces in future simulations.

4.2.5 Non-linear Forces

For the sake of completeness it should be mentioned, that even for spherical particles the linear spring dashpot model used for the normal forces is not accurate when compared with experimental force measurements for single particles. Recently, BOB HARTLEY and JUNFEI GENG from the Behringer group in Durham provided the data of Fig. 4.4. Instead of a linear depend-

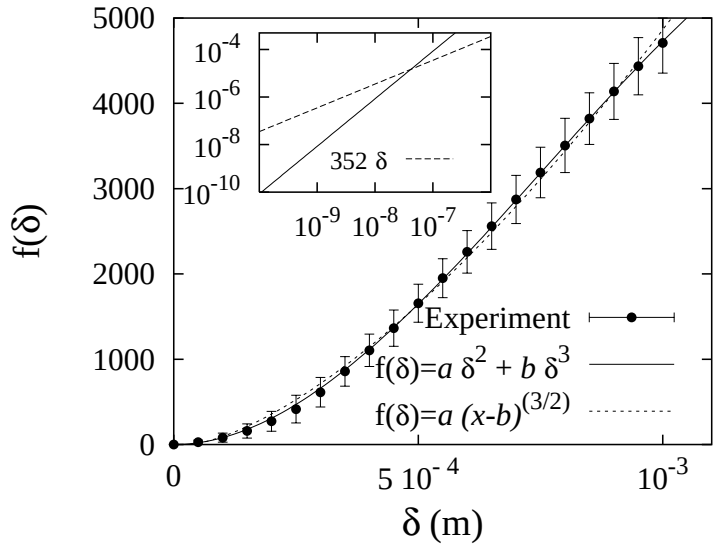

Fig. 4.4: *Experimental curve of the force against the deformation of a single disk of the shear experiment of Howell, Duke University, Durham. (Measurements by Bob Hartley and Junfei Geng). The inset shows the linear force law used for the simulations together with the fitted force law of the experiment in the range of the typical particle overlaps occurring in both the experiment and the simulation.*

ency of the force on the overlap, the data show a cubic behavior. And may be fitted by $f(\delta) = 8.456 \cdot 10^9\, \delta^2 - 3.73 \cdot 10^{12}\, \delta^3$. However, the maximum overlap during a normal run of the simulation is of the order of $10^{-7}\,\mathrm{m}$. Therefore, we are still in a regime where a linear behavior is a rather good approximation to the (fitted) experimental data. More complicated non-linear or hysteretic or plastic models (MEI ET AL. [63]; THORNTON [94, 95]; THORNTON AND ANTONY [96]; THORNTON AND YIN [97]; WALTON AND BRAUN [107, 108]) are not considered in this study but are an interesting direction to follow in order to achieve exact quantitative matching between experiments and simulations.

4.3 Conclusion

In this chapter the simulation method was presented. After a brief description of the used VERLET-integrator scheme and the linked-cell method as a speed up mechanism the force laws of the MD simulation were introduced.

Tab. 4.1: *Microscopic material parameters of the model*

Property		Values
normal spring constant	k^n	$352.1\ \mathrm{N/m}$
normal viscous coefficient	γ^n	$0.19\ \mathrm{kg/s}$
Coulomb friction coefficient	μ_C	0.44
tangential spring constant	k^t	$267.1\ \mathrm{N/m}$
tangential viscous damping	γ^t	$0.15\ \mathrm{kg/s}$
bottom friction coefficient	μ_b	2×10^{-5}
bottom spring constant	k^b	$267.1\ \mathrm{N/m}$
bottom viscous damping	γ^b	$0.15\ \mathrm{kg/s}$
bottom torque parameter	τ^M	0.0001

For the normal component of the inter-particle forces a linear spring dashpot model (Eq. 4.9) is used. Elastic and dissipative behavior are taken into account with this kind of normal forces. Possible extensions towards a nonlinear force law were given in Section 4.2.5 but are not considered in this thesis.

We argued that it is necessary to implement a Cundall-Strack spring (Eq. 4.20) and commented on the extension to implement damping. Additionally to the normal and tangential direction of the forces a friction with the bottom was implemented. In summary the complete force law reads as

$$\begin{aligned} \vec{f} &= \vec{f}^n + \vec{f}^t + \vec{f}^b && (4.30)\\ &= k^n \delta\vec{n} + \gamma^n \vec{v}^n && (4.31)\\ &\quad -\min(\mu_C f^n, |\vec{f}^{t*}|)\vec{f}^{t*}/|\vec{f}^{t*}| && (4.32)\\ &\quad -\min(\mu_b f^n, |\vec{f}^{b*}|)\vec{f}^{b*}/|\vec{f}^{b*}|\ . && (4.33) \end{aligned}$$

The values of the different parameters used throughout this study are summarized in Table 4.1.

5 The Averaging Method

One advantage of a discrete element simulation is the possibility to obtain detailed information such as forces and stresses of an individual particle. However, the behavior of an isolated particle is not significant for the behavior of the whole system, as most of the measurable quantities in granular materials vary strongly on short distances.

One example is the stress, which is not constant inside a grain, but has its largest value at the contacts. An other illustrative example are force chains. The forces in granular materials are transmitted at the contact points from one grain to the other. Thus a network of forces forms inside the medium bearing all the forces and leaving some particles in "cages" nearly force free. In Fig. 5.1 few dark particles carry high forces caging some light gray particles.

This fluctuating behavior, also found in experiments, necessitates the averaging over suitable domains, which in general leads to smearing out the fluctuations. In order to suppress the fluctuations, we perform averages in both, time and space. Which is possible first, due to the quasi-steady state and second, because of the chosen axisymmetric boundary conditions, i.e., the macroscopic fields, when viewed in cylindrical coordinates, should only depend on the radial coordinate. Therefore, averages are taken in ring-shaped areas, concentric to the inner wheel. The mean value is reported on the mid-radius of each ring. The finite width of these rings is limited

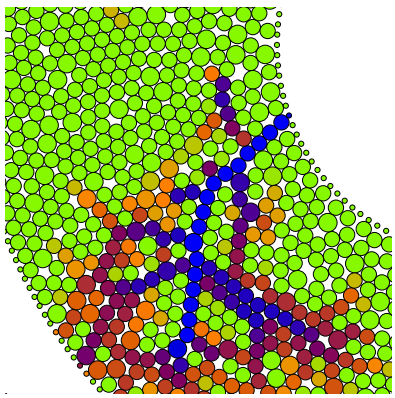

Fig. 5.1: *Force chain spanning the lower left part of the shear device. Dark indicates high forces (high potential energy) on a particle.*

by the need for "sufficiently many" particles inside one ring. The question what "sufficiently many" actually means is addressed in Sect. 5.3 about the Representative Elementary Volume (REV).

In this section we first elaborate the averaging strategy used to obtain scalar as well as tensorial quantities. By using this technique on the density field of the simulation we demonstrate the legitimacy for the time and space averaging. In the last part of this chapter the dependence of the results on the width of the averaging area is presented.

5.1 Averaging Strategy

The intriguing feature of granular materials that most of the measurable quantities vary strongly, both in time and on short distances, leads to the question how to perform proper averages. In general during the computation of the properties presented later on, one has either to reduce or to average over the fluctuations.

In our system it is possible to perform averages in time as well as in space. The time averaging is justified because the system can run for a long time in a quasi-steady state. Therefore, e.g., small but fast rearrangements in the granulate are accounted for by taking averages over many snapshots in time with time steps Δt.

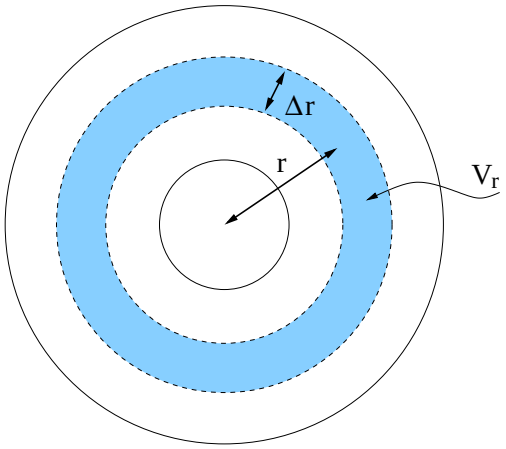

Fig. 5.2: *Points at a certain distance r from the origin are equivalent to each other, therefore space averaging is performed in ring shaped areas of width Δr.*

Additionally, in the cylindrical symmetry of the Couette device all points at a certain distance r from the origin are equivalent to each other. The space averaging is done as follows. Data are measured in rings of material at a center-distance r with width Δr so that the averaging volume of one ring is $V_r = 2h\pi r\Delta r$, as sketched in Figure 5.2. Although our data are two-dimensional the averages taken are three dimensional, with h being the height of the particles ($6\,\mathrm{mm}$).

For the sake of simplicity (and since the procedure is not restricted to cylindrical symmetry), the averaging volume is denoted by $V = V_r$ in the following. The rings are numbered from $s = 0$ to $B-1$, with $B = (R_o - R_i)/\Delta r$. Each ring s reaches from $r^s = r - \Delta r/2$ to $r^{s+1} = r + \Delta r/2$. Averaging over many snapshots is somehow equivalent to an ensemble average. However, we remark that different snapshots are not necessarily independent of each other as discussed in Sect. 5.2 and the duration of the simulation might be too short to explore a representative part of the phase space.[1]

Local Coordinate System

Since we are interested not only in scalar but also in tensorial quantities a local coordinate system is used at every averaged particle. A local directed quantity like a vector, is therefore, rotated depending on the Cartesian posi-

[1] Especially in the outer part of the system where the dynamics is very slow.

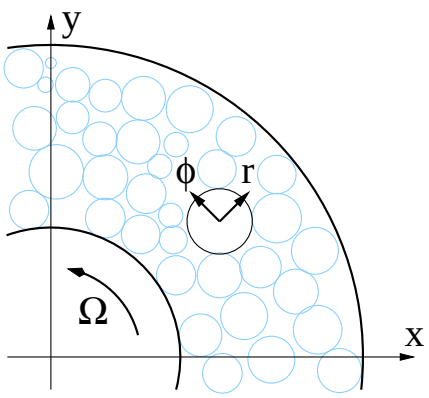

Fig. 5.3: *Local coordinate system for a particle in the shear device.*

tion $\vec{r}_i = (x_i, y_i)$ of the corresponding particle i. The orientation of particle i is $\phi_i = \arctan(y_i/x_i)$ for $x_i > 0$ and periodically continued for $x_i < 0$ so that ϕ_i can be found in the interval $[-\pi, \pi]$. The vector $\vec{n}^c$ that corresponds to contact c of particle i is then rotated about the angle $-\phi_i$ from its Cartesian orientation before being used for an average. Note that this does *not* correspond to a transformation into orthonormal cylindrical coordinates.

In the following, the index r is used for the radial outward direction and the index ϕ is used for the counterclockwise perpendicular direction.

5.2 The Averaging Formalism

The core of our averaging formalism is the definition of the mean value of some quantity Q as

$$Q = \frac{1}{V} \sum_{i \in V} w_i^V V_i Q_i \,, \tag{5.1}$$

with the particle volume V_i, the pre-averaged particle quantity

$$Q_i = \sum_{c=1}^{\mathcal{C}^i} Q^c \,, \tag{5.2}$$

and the quantity Q^c attributed to the contact c of particle i which has $\mathcal{C}^i$ number of contacts.

The simplest choice for w_i^V, the weight of the particle's contribution to the average, is

$$w_i^V = \begin{cases} 1, & \text{if the center of the particle lies inside the ring} \\ 0, & \text{otherwise} \end{cases} \tag{5.3}$$

This method will be referred to as *particle-center averaging* in the following and is shown schematically in Figure 5.4(a).

A more complex way to account for particles which lie partially inside the averaging volume is the *slicing-method*. With this method the weight w_i^V corresponds to the fraction of the particle's volume that is covered by the averaging volume. Since an exact calculation of the area of a circular particle that lies in an arbitrary ring is rather complicated, we assume that the boundaries of V are locally straight, i.e. we cut the particle in slices, as shown in Fig. 5.4(b). The error introduced by using straight cuts is well below one per-cent in all situations considered here.

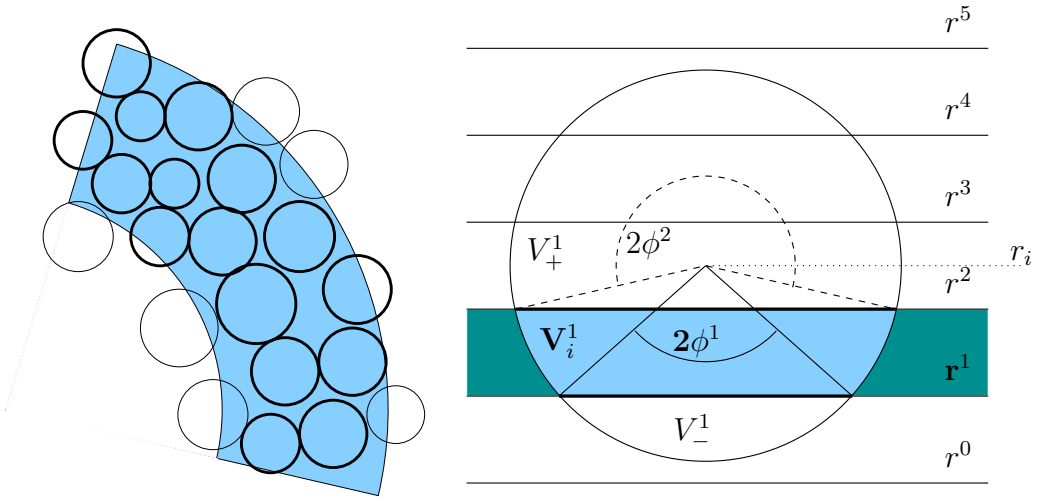

(a) particle-center averaging (b) slicing method

Fig. 5.4: **(a)** *Schematic plot of discrete particles. The averaging volume is intimated by the shaded area and the particles plotted as thick circles contribute to the average.* **(b)** *Schematic plot of a particle i at radial position r_i which is cut into pieces by the boundaries r^s of the averaging volumes. We assume $s = 0, \ldots, m+1$ such that all r^s with $s = 1, \ldots, m$ hit the particle, i.e. $|r_i - r^s| < d/2$.*

The volume $V_i^s = w_i^V V_i$ of a particle i which partially lies between r^s and r^{s+1} is calculated by subtracting the external volumes V_-^s and V_+^s from the

particle volume $V_i = \pi h(d_i/2)^2$ so that

$$\begin{aligned} V_i^s &= V_i - V_-^s - V_+^s \\ &= h(d/2)^2[\pi - \phi^s + \sin(\phi^s)\cos(\phi^s) \\ &\qquad -\phi^{s+1} + \sin(\phi^{s+1})\cos(\phi^{s+1})] \end{aligned} \tag{5.4}$$

with $\phi^s = \arccos(2(r_i - r^s)/d)$ and $\phi^{s+1} = \arccos(2(r^{s+1} - r_i)/d)$. The term $(d/2)^2\phi$ is the area of the segment of the circle with angle 2ϕ, and the term $(d/2)^2\sin(\phi)\cos(\phi)$ is the area of the triangle belonging to the segment. In Fig. 5.4(b) the case $s = 1$ is highlighted, and the boundaries between V_-^s, V_i^s, and V_+^s are indicated as thick solid lines. The two outermost slices $V_i^0 = V_-^1$ and $V_i^s = V_+^{s-1}$ have to be calculated separately.

Time Averaging

As a first example for an averaged scalar quantity, the local volume fraction ν is computed. The volume fraction is related to the local density $\varrho(r) \approx \varrho^p\nu$, with the material density ϱ^p. With the proposed averaging formalism the local volume fraction is given by

$$\nu = \nu(r) = \frac{1}{V}\sum_{i\in V} w_i^V V_i \,. \tag{5.5}$$

It means that Q_i of Eq. 5.1 is set to 1.[2]

The volume fraction ν is displayed for snapshots at different averaging times in Fig. 5.5, in order to understand the fluctuations in the system over time, and to test whether subsequent snapshots can be assumed to be independent.

Changes in density are very weak and mostly occur in the dilated shear zone for small $\tilde{r}$. Note that a rather large dilation in the thin shear zone part leads to a comparatively small compression of the remaining outer part.

From one snapshot to the next, we frequently find that the configuration in the outer part of the shear cell has not changed, whereas a new configuration is found in the inner part. Only after rather long times does the density

[2] For a completely filled averaging volume one would obtain a value of $\nu = 1$. The densest possible packing with mono-disperse particles, a hexagonally packed system, would result in a volume fraction of $\nu = 0.9069$ while a square packing results in $\nu = 0.7854$.

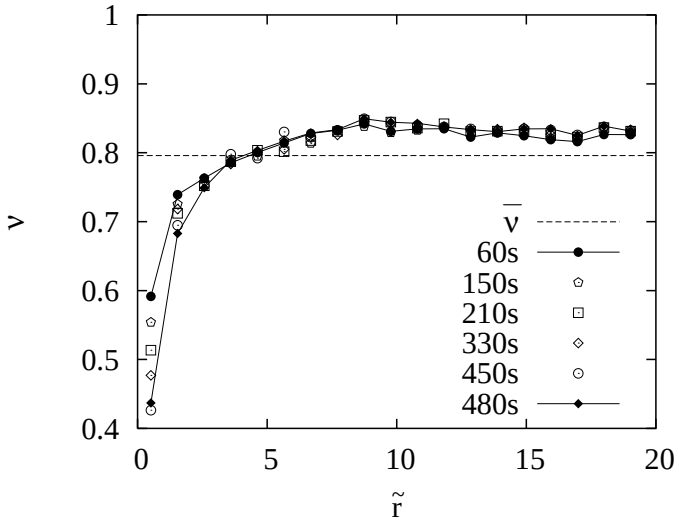

Fig. 5.5: *Volume fraction ν, plotted against the dimensionless distance $\tilde{r} = (r - R_i)/d_{\mathrm{small}}$ from the inner ring, for different times from a simulation with an initial global volume fraction $\bar{\nu} = 0.796$. After some rotations of the inner wheel the volume fraction in the inner part of the system does not change within fluctuations. For the averaging procedure the slicing method is used.*

change also in the outer part. Thus, simulation results in the outer part are subject to stronger fluctuations because the average is performed over less independent configurations than in the inner part.

5.3 Representative Elementary Volume (REV)

An important question is, how does the result of an averaging procedure depend on the size of the averaging volume V. We combine time- and space averaging, i.e. we average over many snapshots and over rings of width Δr, so that the remaining "size" of the averaging volume is the width of the rings Δr. In Fig. 5.6 data for ν at fixed position $r = 0.12$, 0.13, 0.14, and $0.20\,\mathrm{m}$, but obtained with different width Δr, are presented. The positions correspond to $\tilde{r} \approx 2.2$, 3.6, 4.9, and 13, when made dimensionless with the diameter of the small particles. Both the particle-center method (open symbols) and the slicing method (solid symbols) are almost identical for $\Delta r/d_{\mathrm{small}} \geq 2$, for the larger Δr the averaging volume can partially lie out-

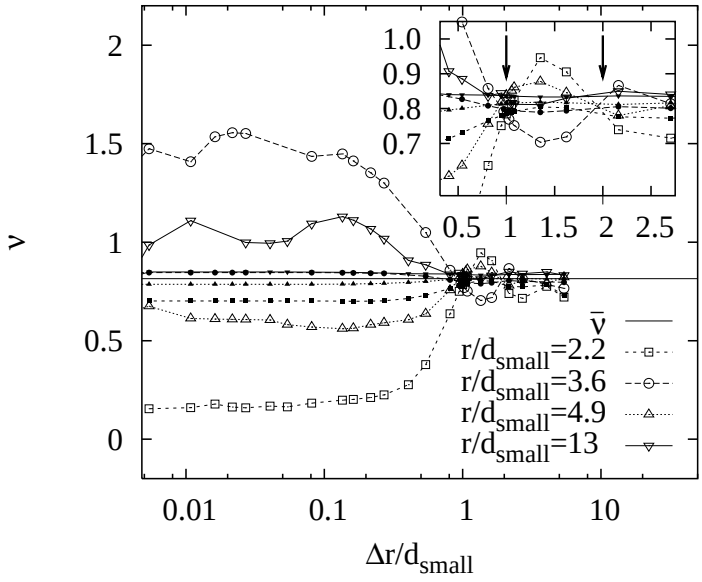

Fig. 5.6: *Volume fraction ν at different distances r from the inner ring, plotted against the width Δr of the averaging ring. Note that the horizontal axis is logarithmic. The open symbols are results obtained with the particle-center method, the solid symbols are results from the slicing method. The inset is a zoom into the large Δr region. The arrows indicate the optimal width Δr for the particle-center method for which the results appear almost independent of the averaging procedure.*

side the system. For very small $\Delta r/d_{\mathrm{small}} \leq 0.1$ the different methods lead to strongly differing results, however, the values in the limit $\Delta r \to 0$ are consistent, i.e. independent of Δr besides statistical fluctuations. In the intermediate regime $0.1 < \Delta r/d_{\mathrm{small}} < 2$, the particle-center method strongly varies, while the slicing method shows a comparatively smooth variation.

Interestingly, all methods seem to collapse at $\Delta r_{\mathrm{REV}} \approx d_{\mathrm{small}}$ (and twice this value), close to the size of the majority of the particles. For the examined situations, we observe that the particle-center and the slicing method lead to similar results for $0.97 \leq \Delta r_{\mathrm{REV}}/d_{\mathrm{small}} \leq 1.03$. This indicates that the systems (and measurements of system quantities) are sensitive to a typical length scale, which is here somewhat smaller than the mean particle size. When using this special Δr_{REV} value, one has $B = 20$ or $B = 21$ binning intervals. The open question of this being a typical length scale that also occurs in systems with a broader size spectrum, cannot be answered with our setup, due to the given particle-size ratio.

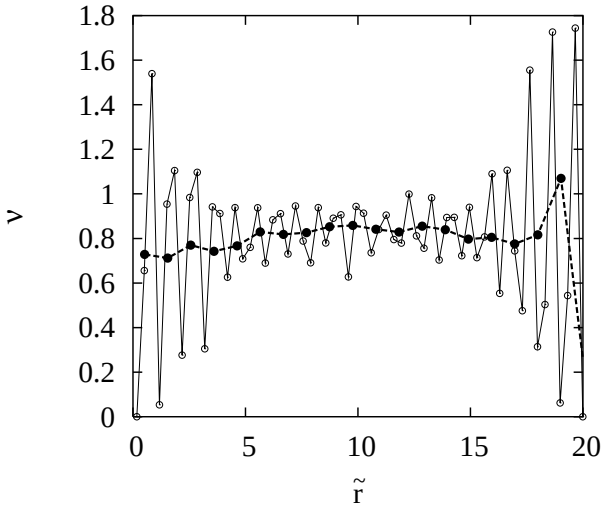

(a) particle-center method

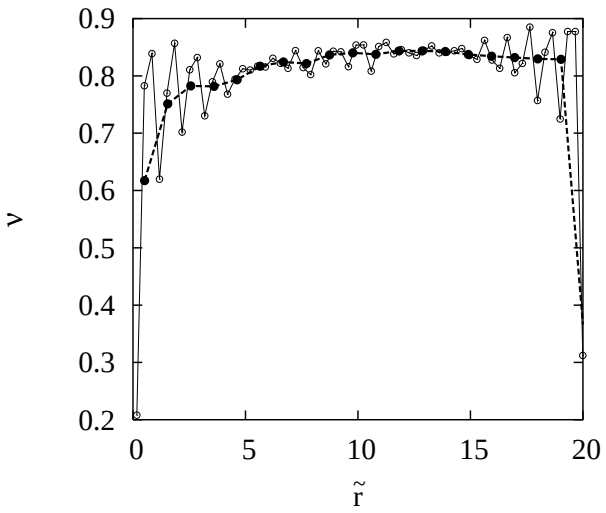

(b) slicing method

Fig. 5.7: *Volume fraction ν plotted against the dimensionless distance $\tilde{r} = (r - R_i)/d_{\mathrm{small}}$ from the inner ring for the different binning methods. Two different binnig widths are investigated. The closed (open) symbols correspond to 20 (60) binning intervals, respectively. The data are taken from a simulation with a global packing fraction $\bar{\nu} = 0.804$.*

In Fig. 5.7 the results of the particle-center and the slicing averaging strategy are ploted for two different widths of binning. The curves of the particle-

center averaging strongly fluctuate for $B \geq 24$ which can be seen in the figure where the density is plotted for 20 and 60 binning intervals. The data points even exceed the value 1.0 for fully packed samples. These oscillations arise due to ordered layers of the particles close to the walls. The particle-center method leads to peaks, where the centers of the particles in a layer are situated and to much smaller densities where few particle centers are found; the particle-center density is obtained rather than the material density. The slicing method although shows oscillations for fine binnigs but these oscillations are much smoother and never exceed 1; the slicing method reflects the real density distribution for fine enough binning. For that reason the particle slicing method will be used in the following.

5.4 Conclusion

Finally, we should remark that the most drastic assumption used for our averaging procedure is the fact, that all quantities are smeared out over one particle. Since it is not our goal to solve for the stress field inside one particle, we assume that a measured quantity is constant inside the particle. This is almost true for the density, but not, e.g., for the stress. However, since we average over all positions with similar distance from the origin, i.e. averages are performed over particles with different positions relative to a ring, details of the position dependency inside the particles will be smeared out anyway. An alternative approach was recently proposed by GOLDHIRSCH [36] who smeared out the averaging quantities along lines connecting the centers of the particles and weighted the contribution according to the fraction of this line within the averaging volume.

6 Comparing Simulation and Experiment

In this chapter the simulation results are compared quantitatively to those of the experiment carried out by the group of R. BEHRINGER, in Durham, North Carolina, USA (HOWELL ET AL. [42]; HOWELL [43]; VEJE ET AL. [102]) and agreement is found.

Provided that numerical and experimental results agree on the grain displacement and rotation fields, the simulation may be considered as complementary to the physical experiment, providing additional information concerning stresses and forces at the microscopic level.

In the first section 6.1 the density profiles are investigated, and used to determine the width of the shear zone which forms after a short time of shearing near the inner wall of the Couette device. Various global densities are used and their influence on the width of the shear band is pointed out in Section 6.2. We find a specific global density $\bar{\nu}$ which results in maximum shear band width.

In Section 6.3.1 the velocity profiles of both, the experiment and the simulation are compared. The mean azimuthal velocity decreases roughly exponentially with the distance from the inner shearing wheel. Within the statistical fluctuations, there is shear rate invariance, rectifying a *quasi steady state*.

The mean particle spin oscillates near the wheel, but falls rapidly to zero

away from the shearing surface. These spin profiles are investigated in Section 6.3.2, before distribution data are compared in Section 6.3.3. The distributions for the tangential velocity and particle spins show a complex shape particularly for the grain layer nearest to the shearing surface, indicating a complicated dynamics. One key to the understanding of this dynamics is the role of stick-slip motions at the interface. This can be demonstrated by a two-variable distribution.

Finally, we comment on the remaining differences between simulation and experiment.

6.1 Density Change with Time

In the traditional picture for shearing of a dense granular material, grains are assumed to be relatively hard so that they maintain their *eigen-volume*. If shear is applied to a granular sample, the grains will respond elastically[1] up to the point of failure where the particles break. The question if the elastic response does exist at all is another issue, not addressed here (GENG ET AL. [33]; VANEL ET AL. [100]). Before failure, the grains will dilate against an applied normal load, and shear will be made possible.

In our setup, this process of dilation begins with the motion of grains nearest to the shearing wheel. The density in the vicinity of the inner wheel decreases as the process evolves; leading to an axial flow further from the shearing wheel. Generally, one assumes that under continued shearing the system can reach a steady state, subject to localized failure in the narrow regions known as shear bands.

The feature of shear band formation, already shown in the discussion of the steady state in Sect. 5.2, is easy to see in the time evolution of the system. Starting from a fairly uniform random packing (dashed lines in Fig. 6.1); the local packing fraction ν quickly becomes nonuniform radially as a consequence of the shearing. This effect occurs in the plot of the simulation data already for the initial density right after the compression of the shear cell, because the inner wheel is rotating from the very beginning. The

[1] If they are not infinitely rigid.

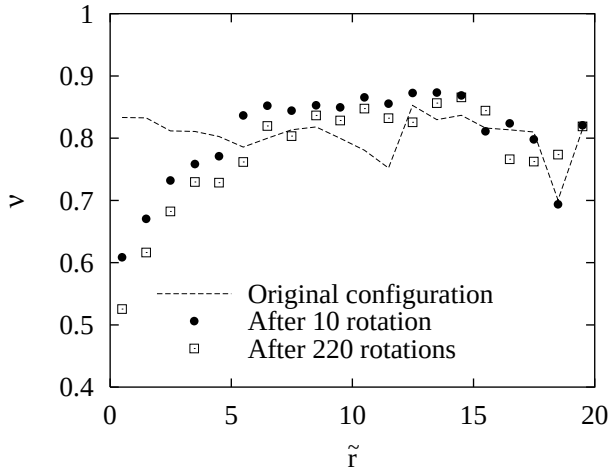

(a) experimental data

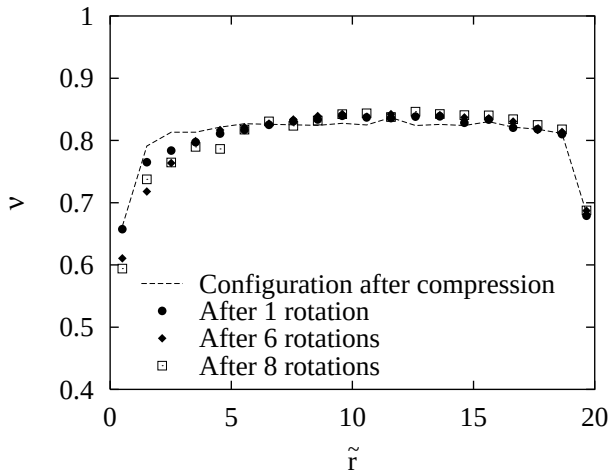

(b) simulation data

Fig. 6.1: *Volume fraction ν plotted against the dimensionless distance $\tilde{r} = (r - R_i)/\tilde{d}$ from the inner ring, for different times. The experiment* **a)** *is performed over a long time, while the simulation data* **b)** *investigate 8 rotations of the inner wheel. Still both plots demonstrate that after some rotations of the inner wheel the volume fraction in the inner part of the system does not change within fluctuations. The data were taken from a system of disks with a global packing fraction of $\bar{\nu} = 0.804$.*

dashed line in the lower panel of Fig. 6.1 therefore represents a transient state between the initial and the steady state of the shear band. Whereas,

the experimental data are obtained from the static initial state, where no onset of the shear band could take place.

The transient time for the formation of the shear band is less than about five rotations of the inner wheel. The simulation data hint that after several rotations the reorganizations in the inner part lead only to changes within the fluctuations of the density profile and the process of shear band formation is slowing down. However, the inner wheel of the experiment can be run for quite long times (days). While most of the evolution of the resulting shear band also occurs in less than about five inner wheel rotations (HOWELL [43]), there are indications that small changes of the profile continue to occur even over very long times. Given a CPU-time of $1-2$ days per rotation, not more than 8 rotations of the inner ring were investigated in the simulation. Therefore, the true long-time behavior is not discussed here.

6.2 Changing the Packing Fraction

In both, the experiment and the simulation, various global packing fractions

$$\bar{\nu} = \frac{1}{V_{\text{tot}}} \sum_{p=1}^{N} V^p \tag{6.1}$$

of the shear cell are examined. The sum in Eq. 6.1 runs over all particles p with volume V^p in the cell, with $V_{\text{tot}} = \pi(R_o^2 - R_i^2)$. Because V_{tot} is fixed for all simulations, $\bar{\nu}$ is varied by changing the number of particles in the apparatus. The particle number was varied form 2866 to 2978 grains, corresponding to $0.789 \leq \bar{\nu} \leq 0.828$; while always about 86% of the total number of particles were small particles. The details are summarized in Tab. 3.2 of Sect. 3.

In this section the dependence of the local density and the kinematics of the system are examined as a function of $\bar{\nu}$. Using this global density $\bar{\nu}$ as a parameter has led to the discovery of an interesting transition as the system approaches a critical packing fraction, $\bar{\nu}_c$ (HOWELL ET AL. [42]). In the experiment we found $\bar{\nu}_c \sim 0.792$ whereas in the simulation $\bar{\nu}_c \sim 0.793$ is evidenced.

The reason for the $\bar{\nu}$-dependence is easy to understand by imagining what

would happen if $\bar{\nu}$ was very low. In this case, grains would easily be pushed away from the wheel, and after some rearrangements they would remain at rest without further contact with the moving wall. Increasing $\bar{\nu}$ by adding more and more grains leads to the critical mean density, $\bar{\nu}_c$, such that there would always be at least some grains subject to compressive and shear forces from the boundaries. By adding more grains, the system would strengthen, more force chains would occur, and grains would be dragged more frequently by the shearing wheel. If even more particles were added, the system would become very stiff and eventually would become blocked, i.e. so dense that hardly any shearing can take place. In the extreme limit, due to large compressive forces and deformations, permanent plastic deformations might occur and brittle materials even might fracture. However, due to the rather soft, rubber-like polymeric material used in the experiment and due to the relatively weak forces applied, this limit can not be investigated with our setup.

6.2.1 Density

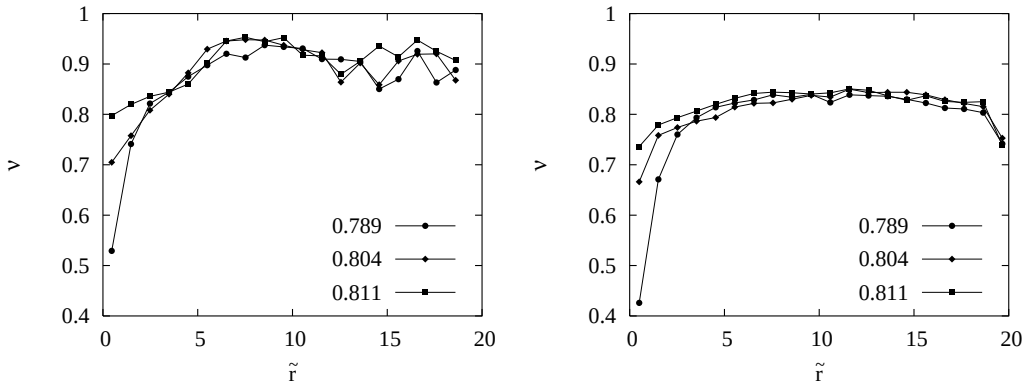

Fig. 6.2: *Volume fraction ν, plotted against the dimensionless distance from the origin $\tilde{r} = (r - R_i)/\tilde{d}$, for different initial global densities $\bar{\nu}$. The left plot shows data for the experiment, in the right plot simulation data are displayed.*

We first consider again the local density profiles. In the two plots of Fig. 6.2 the local density ν is observed and plotted vs. $\tilde{r} = (r - R_i)/\tilde{d}$ the radial distance scaled by the mean particle diameter $\tilde{d}$. Two regions are clearly separated in the data presented for various $\bar{\nu}$ values.

First, the outer part of the system; the dynamics in the outer part is really

slow so that very few reorganizations take place and the packing fraction changes only very slightly. In the outer part of the system the experimental data express higher fluctuations than the simulations, which might be due to the different way of the preparation of the samples. During the compression phase of the simulation the particles tend to form homogeneous clusters. Later in the shearing phase these clusters are only subject to very few rearrangements due to the slow dynamics in the outer part of the system. The outermost data points in the simulation plots of Fig. 6.2 are significantly lower than the mean value in the outer part of the system because of ordering effects arising due to the boundary conditions which foster crystallization of the outermost grains.

The behavior of the inner part of the system is different: The data presented for various $\bar{\nu}$ values clearly indicate a dilated region close to the inner wheel for both the experiment and the simulation, where those of the simulation are systematically smaller than the experimental ones.

These deviations are due to differences in obtaining local density data either from experiment or from simulation:

• In the simulations the data are averages over full rings around the symmetry center of the shear cell, whereas in the physical system a radial slice that corresponds to one quarter of the entire apparatus was used for averaging. Even though averages were computed over an extended time interval, a systematic error due to this procedure cannot be ruled out. Because of possible circumferential fluctuations associated with this averaging process, the area under the experimental curves is not necessarily constant, and not necessarily identical to the global density.

• In the experiment the local density is measured via optical intensity methods, where also some uncertainty is intrinsic due to light scattering and nonlinear transmission. In addition, calibration is complicated by the fact that the real particles are not perfect disks as assumed in the simulation. Specifically, data are obtained by using the fact that UV light is strongly attenuated on passing through the photoelastic disks. This technique is calibrated against packings with well known area fractions, such as square and hexagonal lattices. For details see the PhD thesis of HOWELL [43]. There are still some small systematic uncertainties in this procedure, and if one computes the packing fraction using the experimental data given in the upper part of Fig. 6.2, a packing fraction higher than the global one is found.

For that reason we shift the experimental local density data downward by a constant value of $\nu_{\text{shift}} = 0.08$.

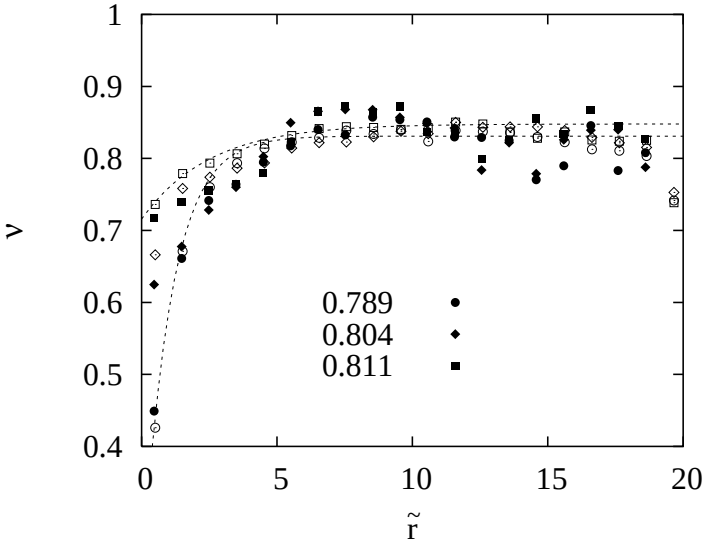

Fig. 6.3: *Volume fraction ν, plotted against the dimensionless distance from the origin $\tilde{r} = (r - R_i)/\tilde{d}$, for different initial global densities. The solid symbols show experimental data $\nu - \nu_{\text{shift}}$ shifted by $\nu_{\text{shift}} = -0.08$. The open symbols resemble simulation data with $\bar{\nu}$ as given in the legend. The dotted lines are exponential fits to the simulation data as obtained by Eq. 6.2.*

After shifting the local densities the data of Fig. 6.3 show good quantitative agreement between simulation and experiment within the fluctuations. Like in the time dependent density profiles of Fig. 6.1 there is again a clear difference in density between the dynamic, dilute shear zone and the static outer area for all $\bar{\nu}$.

In order to quantitatively determine the width of the shear zone the density profiles of the experimental as well as the simulation data are fitted with an exponential curve of the form:

$$\nu_f = \nu_0 - B \exp(-C(r - R_i)/\tilde{d}) \,, \tag{6.2}$$

where ν_0, B and C are fit parameters. For the fits to the simulation data the range of $0.5 \leq \tilde{r} \leq 8.5$ was used. The dotted lines of Fig. 6.3 show two exemplary fits to the simulation data for $\bar{\nu} = 0.789$ and 0.811, respectively. The variation of the fit parameters ν_0 and B with different $\bar{\nu}$ is shown in Fig. 6.4.

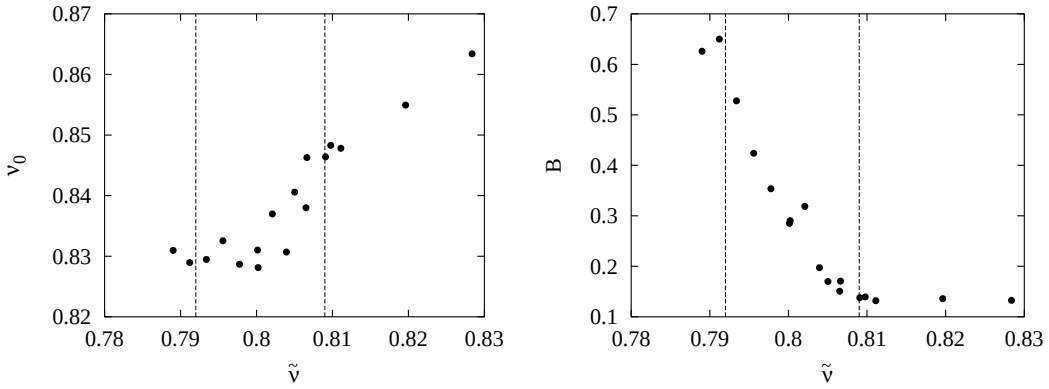

Fig. 6.4: *The plots show the fit parameters ν_0 and B of Eq. 6.2 vs. $\bar{\nu}$ the global packing fraction.*

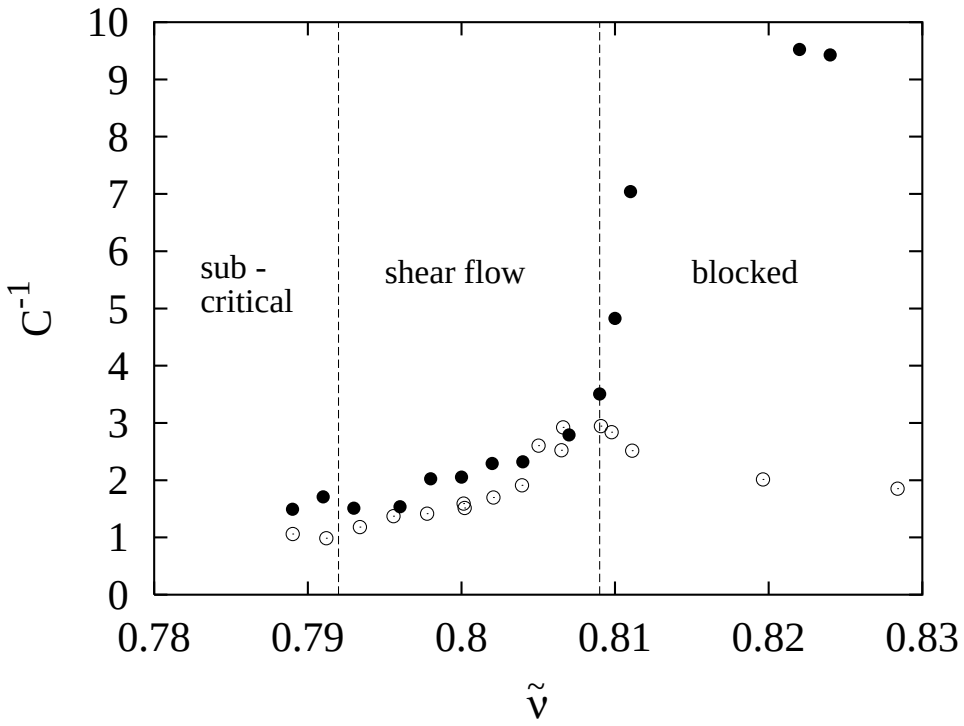

Fig. 6.5: *Exponential width of the shear band as obtained by Eq. 6.2 versus the global packing fraction. The solid symbols resemble experimental, the open symbols simulation data.*

The exponential width C^{-1} of the fits is shown in Fig. 6.5. For simulations with a volume fraction of $\bar{\nu} < \bar{\nu}_c$ a *sub critical* state is reached after some rotations of the inner shearing wheel. The innermost particles are pushed

away from the inner wall and remain at rest without further contact to the wall. While increasing the volume fraction from $\bar{\nu}_c$ further the width of the shear band decreases because the movement of the particles is more and more hindered. The system is in a *shear flow* regime. At $\bar{\nu} \approx 0.809$ a minimal width of the shear band is found, i.e. C^{-1} of the fit function Eq. 6.2 reaches a maximum for the simulation , as shown in Fig. 6.5. By increasing the packing fraction further the system is *blocked* and the determination of a clear shear zone becomes difficult. The experimental data hint a furthe decreasing shear band width up to $\bar{\nu} \approx 0.811$ before both simulation and experimental data seem to saturate at a specific shear band width.

6.3 Kinematic Quantities

In addition to the density, the mean velocity and the spin of the particles also evolve to a steady state. In this section these kinematic quantities are presented in the steady state and examined for different global packing fractions.

In order to check wether the particles are able to move radially or not, the radial velocity of the particles is plotted in Fig. 6.6. The data of the upper panel were taken from a ring of the width of 1 particle next to the inner ring for the indicated values of $\bar{\nu}$. The width of the Gauss distribution changes with $\bar{\nu}$, but not the mean, which is zero. In the outer parts of the shear cell even less dynamics is found as can be seen in the lower panel of Fig. 6.6.

6.3.1 Velocity Profiles

Because the particles are limited in their radial movements, we focus on the normalized azimuthal velocities, $v_\phi/(\Omega R_i)$, scaled by the angular speed of the inner shearing surface ΩR_i.

The mean of $v_\phi/(\Omega R_i)$ as a function of $\tilde{r}$ is shown in Figure 6.7. All data indicate a roughly *exponential profile* corresponding to a shear zone with a width of a few disk diameters. Additionally, the experimental data show a clear curvature in the outer part of the system were the *saturation level* is reached. This saturation level of fluctuations in the velocity is at a higher

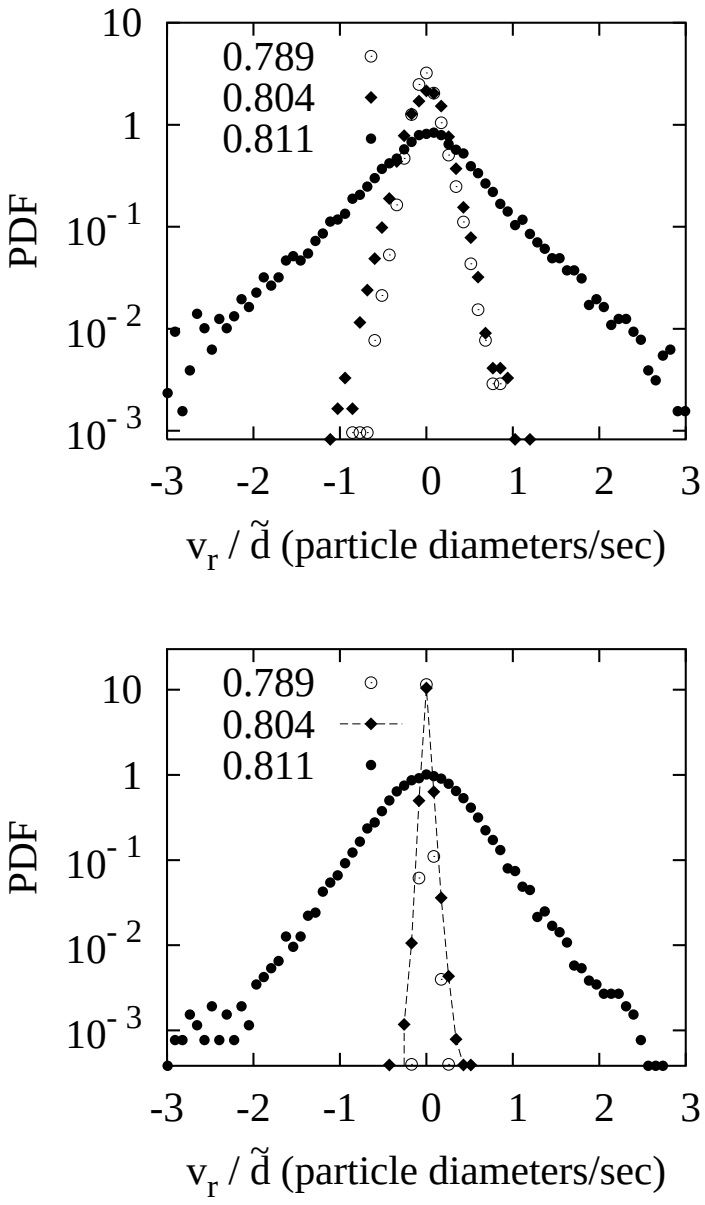

Fig. 6.6: *Radial velocity $v_r/\tilde{d}$ distribution in particle diameters per sec for a bin $0 < r/\tilde{d} < 1$ in the upper panel and $12 < r/\tilde{d} < 13$ in the lower panel. Data are shown for three different values of $\bar{\nu}$. The width of the distribution changes with $\bar{\nu}$, but not the mean, which is zero.*

level for the simulation data, possibly due to the systematically larger shear rate in simulations used to save CPU-time. However, the logarithmic scaling over-amplifies this very small quantity.

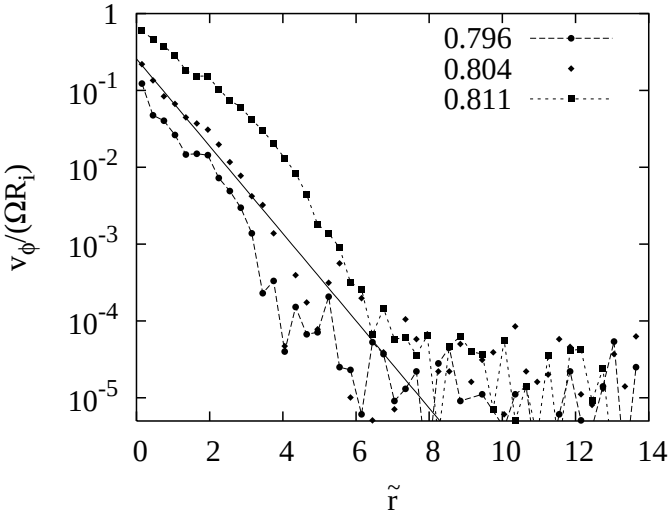

(a) experimental data

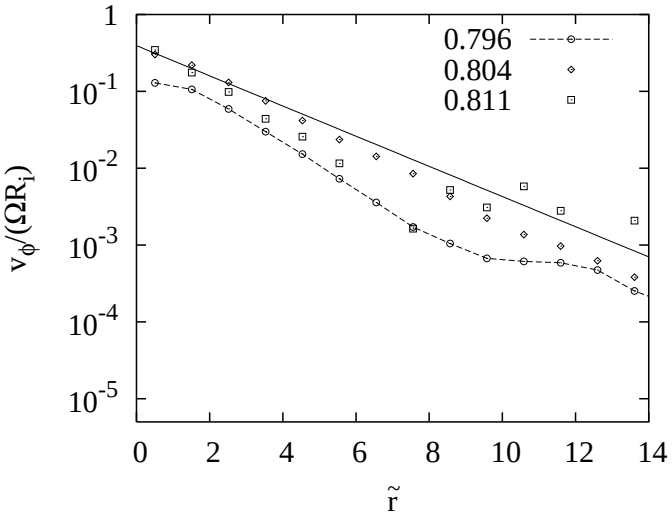

(b) simulation data

Fig. 6.7: *Velocity profiles for different packing fractions $\bar{\nu}$. The mean azimuthal velocities are normalized by the velocity of the shearing surface of the inner cylinder ΩR_i. The solid line is a fit of $A\exp(-((r-R_i)/\tilde{d})/B)$.*

The data of the experiment as well as the simulation data are fitted with $A\exp(-((r-R_i)/\tilde{d})/B)$ in the range of $0 < \ r/d \ < 6$. The amplitude of the exponential term (the velocity of the particles close to the inner wall,

v_0) decays steadily as $\bar{\nu}$ decreases towards ν_c. The simulation data show a weaker decay of the velocity at the inner wall with decreasing density. The values of $v_0/(\Omega R_i) \ll 1$ indicate that either slip or intermittent shear takes place at the inner wall. Only values of $v_0/(\Omega R_i) = 1$ would correspond to perfect shear in a sense that the particles are moving with the wall without slip and during all the time. For high densities the agreement is reasonable, but for low densities the magnitude of the velocities differs strongly. This may be due to either of the differences in bottom- or wall-friction, or due to different wall shape. Especially the more irregular and rough wall in the experiment can lead to stronger intermittency and thus reduced mean velocities.

Our observed profile differs from some recent observations by MUETH ET AL. [67] for 3D Couette shearing experiments, where they report a larger quadratic term relative to the linear one in the exponential. At this point, we do not know what causes this difference, but some obvious candidates are differences in dimensionality, shape of the particles, etc.

6.3.2 Spin Profiles

Another interesting quantity is the spin of the particles. In analogy to the azimuthal velocity we use a normalized spin $s = Sd/(\Omega D)$ with D the diameter of the inner wheel, so that $s = 1$ corresponds to the rolling of the inner particles on the inner shearing wheel. The mean profile for s is shown in Figure 6.8.

The particles adjacent to the wheel rotate backwards on average, i.e., in the direction opposite to the wheel rotation. However, the next layer rotates in the same direction as the wheel on average. These oscillations damp very quickly with distance from the wheel. In order to examine this damping, we fit the spin profile to $Sd/(\Omega D) = A\exp(-B(r - R_i)/d)\cos(\pi(r - R_i)/d + \phi)$. We chose this formula to combine an oscillatory part with an exponentially decaying function. The fit coefficients are $A = 0.24 \pm 0.02$, $B = 1.46 \pm 0.16$ and $\phi = 1.79 \pm 0.08$ for $\bar{\nu} = 0.796$ which means that the oszillations damp away really quick. This is related to the fact that the spin of the disks in a given layer is driven in one direction by neighboring disks that lie in a layer closer to the wheel, while at the same time impeded by neighboring disks that are a layer further from the wheel.

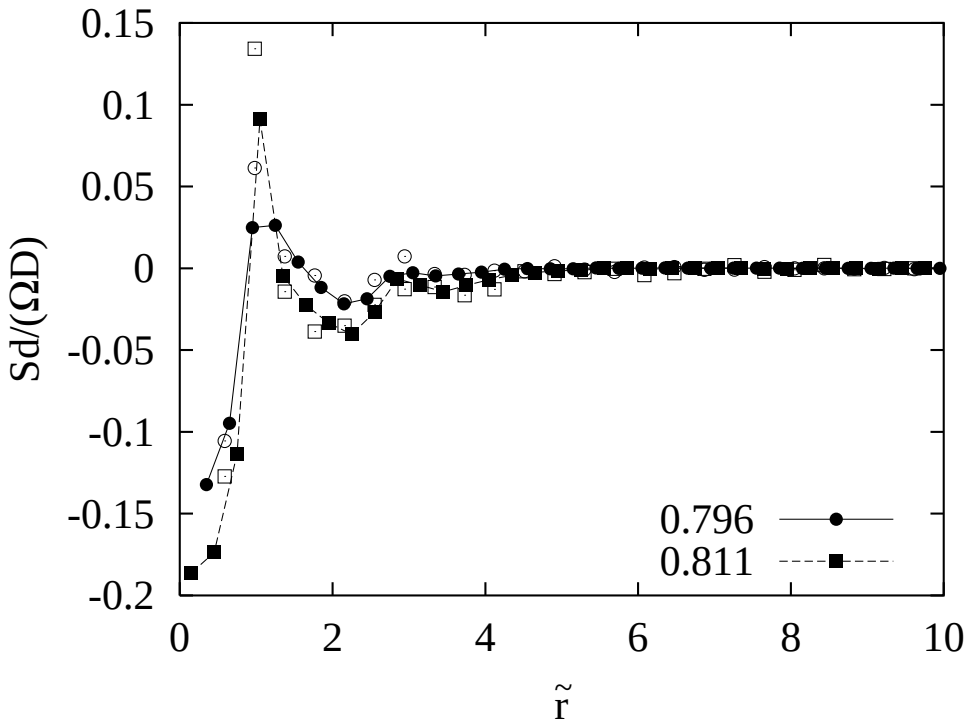

Fig. 6.8: *Spin Profiles for different values of $\bar{\nu}$.*

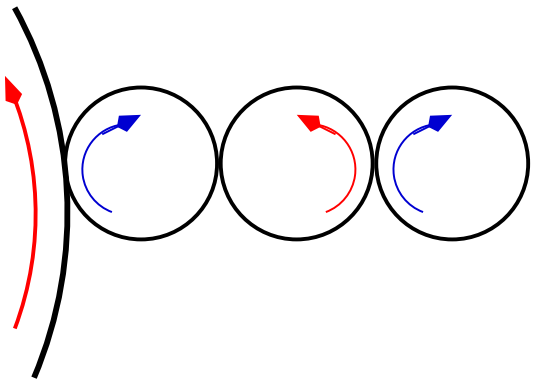

Fig. 6.9: *Schematic plot of the alternating rotation directions of the particles near the inner wheel.*

6.3.3 Velocity Distributions

From the previous section, it is clear that changing the packing fraction must not only change the profiles, but also the distributions of the velocity. In

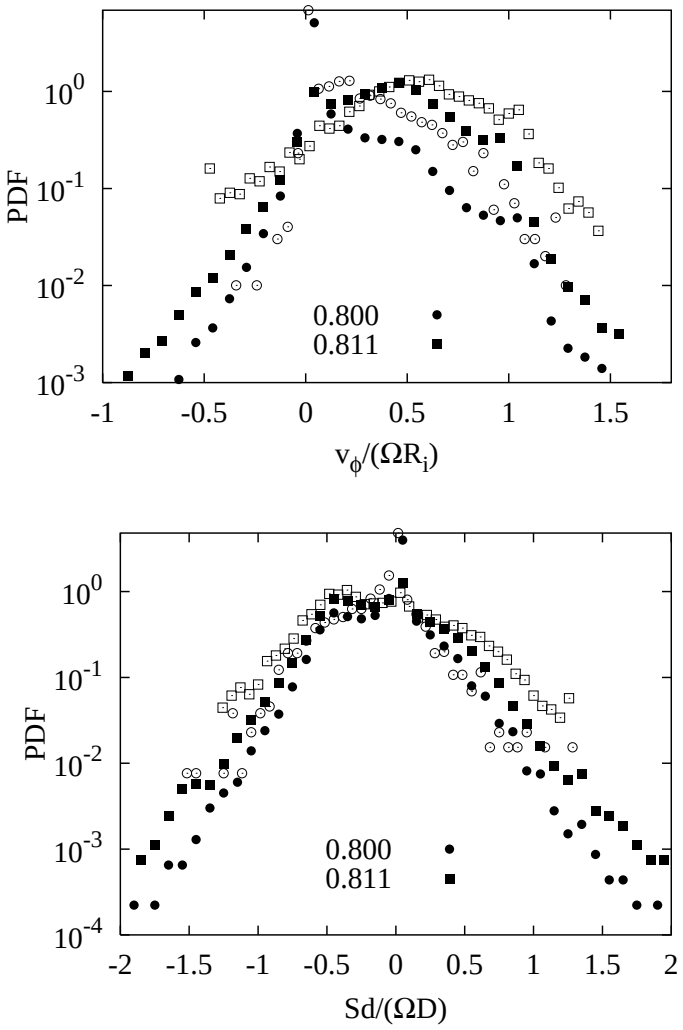

Fig. 6.10: *Velocity and spin distributions. The solid symbols denote experimental the open symbols simulation data.*

Fig. 6.10 the velocity distributions in a one-particle wide bin next to the inner wheel are shown for various $\bar{\nu}$-values from the experiment and the simulation.

The data clearly show that the peaks near zero, corresponding to non-rotating particles, become weaker with increasing density. Furthermore the corresponding regions with negative spin and nonzero v_ϕ grow with increasing $\bar{\nu}$. The fact that increasing $\bar{\nu}$ leading to a decreasing number of stationary particles is not surprising. But the formation of the second peak in the velocity distribution at $v_\phi \simeq 0.5$ is not as intuitive as the small peak at

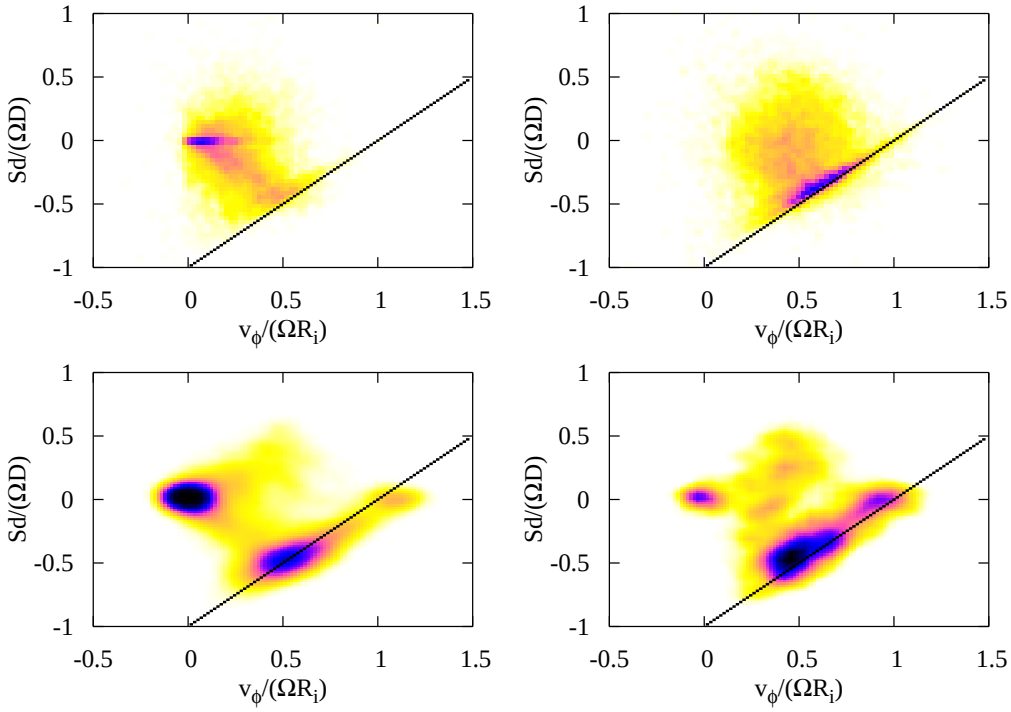

Fig. 6.11: *2D probability density for $v_\phi/(\Omega R_i)$ and $Sd/(\Omega D)$ for $0 < r/d < 1$. Dark is high probability density. The upper panels show simulation data, the lower experimental data for high (right) and low (left) densities $\bar{\nu}$, respectively.*

unity. Instead one might expect a simple broadening of the distribution.

A key to understanding this phenomenon is contained in the two-variable distribution $P(v_\phi/(\Omega R_i), Sd/(\Omega D))$. Examples for this distribution are shown in Fig. 6.11 for high (right) and low (left) density $\bar{\nu}$. The upper panel shows experimental the lower panel simulation data. The probability is coded in grayscale with dark denoting higher probability.

Looking at the figure one finds two distinct features, corresponding to two qualitatively different processes. The first feature is the concentration of probability around $(0, 0)$ which corresponds to a state where the disks are essentially at rest, without neither spin nor translation. The other feature is the clustering of probability around the line $v_\phi/(\Omega R_i) = 1 + Sd/(\Omega D)$. This line corresponds to a non-slip motion of grains relative to the wheel. No-slip here means that the particles execute a combination of backwards rolling and translation, such that the wheel surface and the disk surface remain in continuous contact. The peak at $v_\phi/(\Omega R_i) = 0$, which is strong for low $\bar{\nu}$,

but decreases for high $\bar{\nu}$, corresponds to particles that are so weakly compressed that they can easily slip with respect to the shearing wheel. With higher density, and hence greater forces at the contacts between the grains and the shearing ring, slipping becomes less likely and the combination of translation and backwards rolling is the preferred state.

6.4 Conclusion

We have reported parallel experimental studies and molecular dynamics simulations of shearing in a two-dimensional Couette geometry. Here, an important goal was to benchmark such simulations in a setting where it was possible to have good overlap between the parameters relevant to the simulations and the experiments. In most respects, the numerical results are in good qualitative, partially even quantitative agreement with the experimental results.[2]

Both methods show rate-independence within the statistical errors, and the range of rates that were studied. We have particularly focused on the dependence of the shearing states on the global packing fraction. Good agreement between simulation and experiment was found for the density profiles associated with the formation of a dilated shear band next to the inner shearing wheel and the width of the shear band of about 5-6 particle diameters.

Both simulation and experiment also showed a roughly exponential velocity profile. However, the simulations did not capture the density dependence of the experimental profiles, especially at the outer edge of the shear band. In this regard, further exploration if appropriate of the role of the roughness of the shearing surface and the effect of the particle-bottom friction are necessary. The former can lead to intermittent behavior, whereas the latter might explain the velocity-drop at the outer edge of the experimental shear band.

The alternating spin profiles in experiment and simulation agreed nicely, indicating a roling of the innermost particle layers (parallel to the walls) over

[2] This is astonishing when the possible discrepancies concerning particle shape and boundaries, as well as the partially huge differences between experimental reality and the particle-particle and particle-wall contact models in the simulation are considered.

each other. Outside of the shear band rotations are *not* activated, however. From the velocity- and spin-probability densities, a combination of roling and sliding with the inner wall is evidenced. With decreasing density more and more particles remain at rest – stopped by the bottom friction. With increasing density, more and more particles are dragged with the moving wall, but at the same time roll over each other – in layers with strongly decreasing amplitude away from the moving wall.

The present study is one step towards ending the ever-lasting discussion about the reliability of numerical simulations, and especially simplified molecular dynamics simulations, where only due to the very simple interaction force laws, a simulation with large particle numbers is possible. Even with many differences in details, a quantitative agreement could be achieved and the strong discrepancies could be (possibly) explained by differences that would make the simulations extremely more complicated and an arduous task. Examples therefore are a possible tilt of the particles out of their plane of motion, a possibly wrong modeling of the bottom friction, and a non-perfect cylindrical inner cylinder.

Thus, in conclusion, the appearingly "simple" experiment allows for a lot of discrepancies as compared to a "simple" simulation. There are two ways, either a real experiment is modeled with a more realistic simulation, that takes *all* details into account – a probably non practicable approach – or only the intrinsically unknown important details have to be corrected. In order to learn what these are, we propose to think first of even simpler model experiments that do not leave as much space for discrepancies. This, together with a strong effort in quantitative, and finally predictive, simulations should lead to a better understanding of the flow behavior of granular materials.

7 The Micro-Macro-Transition

In the previous part of this study we presented a MD simulation which is capable to resemble a physical experiment to some extend. Within the computer simulation the state of a granular ensemble is completely described and its development can be fully predicted. This is possible, because the position, the shape, the material properties and the displacement of every grain, as well as the contact forces acting on every grain are known. The behavior of the whole assembly under external forces can exactly be predicted on the *level of the individual grains*. Such a detail description is not necessary in general and in most cases this approach will also be too complicated for practical purposes.

Instead, the goal of the micro-macro-transition is to develop a theory which is capable to predict the macroscopic behavior of a deformable body without looking at all the discontinuous microscopic effects at each grain of the body. To be more precise, our aim is to provide a relationship between external loads acting on the material and the resulting displacements occurring in the sample.

Traditionally, the external loads are expressed in terms of *stresses* and the displacements are reflected by the *strain*. The relation between loads and stress is given in terms of the equilibrium conditions of the continuum, whereas the strain is derived via kinematic considerations. These necessary equations for the kinematics and the balance laws for the classical con-

tinuum theory will be shown in Sect. 7.1. A more detailed derivation can be found e.g. in the textbooks of BECKER AND BÜRGER [8], TRUESDELL [98] and MALVERN [59].

As stated, macroscopic continuum equations for the description of the behavior of granular media rely on constitutive equations for stress, strain, and other physical quantities describing the state of the system. In the classical continuum theory the microscopic (atomistic) structure of a material is not taken into account explicitly. However, the forces acting inside a granular material are transmitted from one particle to the next only at the contacts of the particles. Therefore, the description of the associated network of inter-particle contacts is essential, especially for the quasi-static mechanics of granular assemblies (COWIN [21]; GODDARD [35]). The fabric tensor $\boldsymbol{F}$ is a kind of a measure for the structure of the system. Although, the fabric tensor is not a quantity of the classical continuum theory it will be investigated in Sect. 7.2.

In order to perform the micro-macro-transition, a macroscopic state variable like the stress has to given in terms of microscopic variables. For the stress these variables are the forces acting between the grains and the vectors connecting the center of a particle with its contact points. The derivation for this relation is given in Sect. 7.3.

As an essential ingredient for practical purposes at least a stress-strain relationship should be given as a result of any theory. Therefore, in Sect. 7.4 a definition of the strain based on microscopic variables is given. The behavior of the fabric tensor, the stress tensor and of the strain tensor in our simulations are discussed each in the section where the quantity is defined.

We will close this section by using the stress and the strain to calculate different elastic moduli of our simulation. Therefore, a simple constitutive equation for isotropic, elastic materials of HOOKEs type is used which is elaborated in the next section. Its application we will show in Sect. 7.5 were we will also develop a simple constitutive law which relates the stress to the deformations and (via the fabric tensor) to the local structure of the granulate.

7.1 Classical Continuum Theory

In the following we will briefly summarize the kinematic basis of the classical continuum theory. For the derivation we limit ourself to the geometrically linear regime.

Kinematic Equations

Already the name "continuum" theory hints that matter in this kind of a theory is view as a continuum. The points which form the continuum are called material points X. More precise, every material point is denoted by a label X in a unique way. A body $\mathcal{B}$ is composed of a connected, compact

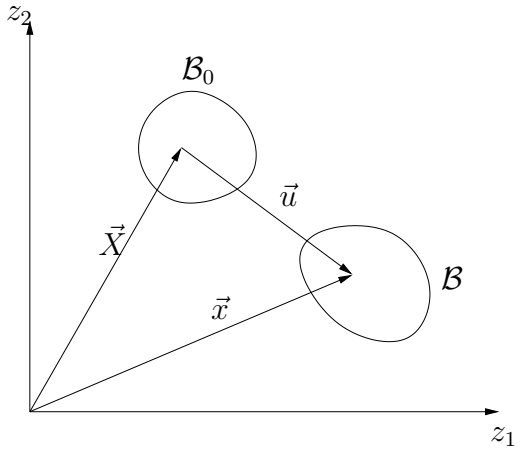

Fig. 7.1: *Schematic drawing of the reference and the actual configuration of a body $\mathcal{B}$.*

set of material points X. The position $\vec{x}$ of each of these points at time t is a function of its position in a chosen reference configuration, $\vec{X}$, and of the current time t

$$\vec{x} = \vec{x}(\vec{X}, t) \; . \tag{7.1}$$

Since neighboring points in the reference configuration are mapped to neighboring points in the actual configuration and due to the principle that at one place there can only be one point and one point can only be at one place, the inverse of Eq. 7.1 can be written as

$$\vec{X} = \vec{X}(\vec{x}, t) \; . \tag{7.2}$$

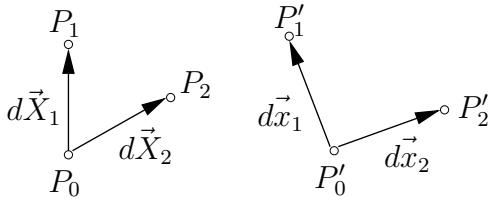

Fig. 7.2: *Schematic drawing of the transformation of two vectors.*

In order to calculate actual problems with the continuum theory a coordinate system has to be introduced. In the following we will use a rectangular Cartesian coordinate system. This coordinate system might be introduced in two different ways: First, the LAGRANGian description which relates the position of the actual configuration to the reference configuration, i.e. measurements are taken at a specific material point moving in space. The other way is to chose a fixed position in space yielding to a spatial (EULERian) formulation.

With this two points of view also two different definitions of the derivative of a quantity $Q = Q(\vec{x}, t)$ exist. At a fixed position in space one computes the *local* derivative

$$\frac{\partial Q}{\partial t} \,. \tag{7.3}$$

In the LAGRANGian formulation the material derivative

$$\frac{Df}{Dt} \,, \tag{7.4}$$

has to be used. These two formulations are related to each other via

$$\frac{DQ}{Dt} = \frac{\partial Q}{\partial t} + \vec{v}\,\mathrm{grad}\; Q \,. \tag{7.5}$$

By this expression the material derivative DQ/Dt equals the local derivative $\partial Q/\partial t$ plus a convective term which captures the influence of the velocity field $\vec{v}$.

For the following it is useful to introduce the displacement vector $\vec{u}$ which depends on the reference configuration and is defined as

$$\vec{u} = \vec{x} - \vec{X} \,. \tag{7.6}$$

For the derivation of material laws it is important to define deformations quantitatively. This is accomplished by the deformation gradient tensor

$$\boldsymbol{D} = \frac{\partial \vec{x}}{\partial \vec{X}} \,. \tag{7.7}$$

The tensor $\boldsymbol{D}$ transforms the vector $d\vec{X}$ connecting to points in the reference configuration into the vector $d\vec{x}$ connecting the same points in the actual configuration. Using Eq. 7.6 leads to

$$\boldsymbol{D} = \boldsymbol{I} + \text{grad } \vec{u} \,. \tag{7.8}$$

With $\boldsymbol{I}$ being the unity tensor. To quantitatively describe the deformation of a body the change of distance between two points may be used. Figure 7.2 shows the vectors $d\vec{X}_1$ and $d\vec{X}_2$ in the reference configuration and their counterparts $d\vec{x}_1$ and $d\vec{x}_2$ in the actual configuration. Taking the difference of the scalar product of these vectors yields

$$\begin{aligned} d\vec{x}_1 \cdot d\vec{x}_2 - d\vec{X}_1 \cdot d\vec{X}_2 &= (\boldsymbol{D} d\vec{X}_1) \cdot (\boldsymbol{D} d\vec{X}_2) - d\vec{X}_1 \cdot d\vec{X}_2 \\ &= d\vec{X}_1 \cdot ((\boldsymbol{D}^{\mathrm{T}} \boldsymbol{D} - \boldsymbol{I}) d\vec{X}_2) \\ &= 2 d\vec{X}_1 \cdot (\boldsymbol{G} d\vec{X}_2) \,. \end{aligned} \tag{7.9}$$

In this equation the GREENS deformation tensor

$$\boldsymbol{G} = \frac{1}{2}(\boldsymbol{D}^{\mathrm{T}} \boldsymbol{D} - \boldsymbol{I}) \tag{7.10}$$

was used. With the definition Eq. 7.8 Eq. 7.10 may be rewritten into

$$\boldsymbol{G} = \frac{1}{2} \left(\boldsymbol{I} + (\text{grad } \vec{u})^{\mathrm{T}} \right) (\boldsymbol{I} + \text{grad } \vec{u}) - \frac{1}{2} \boldsymbol{I} \tag{7.11}$$

$$= \frac{1}{2} \left((\text{grad } \vec{u}) + (\text{grad } \vec{u})^{\mathrm{T}} \right) + \frac{1}{2} (\text{grad } \vec{u})^{\mathrm{T}} \, \text{grad } \vec{u} \,. \tag{7.12}$$

The second term of Eq. 7.12 can be neglected if the gradients of the displacement are small, i.e.

$$\left| \frac{\partial u_i}{\partial X_j} \right| \ll 1 \,. \tag{7.13}$$

With this condition, $\boldsymbol{G}$ is linearized yielding the linearized deformation gradient or strain $\boldsymbol{\epsilon}$ with the components

$$G_{\alpha\beta} = \epsilon_{\alpha\beta} = \frac{1}{2} \left(\frac{\partial u_\alpha}{\partial X_\beta} + \frac{\partial u_\beta}{\partial X_\alpha} \right) \,. \tag{7.14}$$

Momentum Balance

All the previous considerations only affected the kinematics of the continuum. In order to describe the mechanics one has to include the forces acting on a body. A force acting on a body $\mathcal{B}$ can be decomposed

$$\vec{f} = \int_{\mathcal{B}} \vec{b}\, dV \; + \; \int_{\partial\mathcal{B}} \vec{s}\, dA \,, \tag{7.15}$$

into body forces $\int_{\mathcal{B}} \vec{b}\, dV$ and surface tractions $\int_{\partial\mathcal{B}} \vec{s}\, dA$. With the body forces all long range interactions between $\mathcal{B}$, its surroundings and the different parts of $\mathcal{B}$ are captured. The most common body force is the gravity $\vec{b} = -\varrho g \vec{e}_z$ with g the acceleration due to gravity and $\vec{e}_z$ the unit vector pointing vertical upwards.[1] The body force density $\vec{b}$ in this and most other cases is proportional to the mass density ϱ therefore, a mass force density $\vec{k} = \vec{b}/\varrho$ is introduced. Thus Eq. 7.15 can be rewritten as

$$\vec{f} = \int_{\mathcal{B}} \varrho \vec{k}\, dV \; + \; \int_{\partial\mathcal{B}} \vec{s}\, dA \,. \tag{7.16}$$

The second term of Eqs. 7.15 and 7.16 may be interpreted as the part governing the short range interactions of $\mathcal{B}$ and its surroundings. The stress vector $\vec{s}$ is a force per unit area in contrast to $\vec{b}$ which is a force per unit volume.

The momentum of a body $\mathcal{B}$ is defined as

$$\vec{I} = \int_{\mathcal{B}} \varrho \vec{v}\, dV \,. \tag{7.17}$$

Let the reference system be an inertial system. With

$$\frac{D\vec{I}}{Dt} = \vec{f} \tag{7.18}$$

and Eqs. 7.16 and 7.17 the momentum balance equation

$$\frac{D}{Dt} \int_{\mathcal{B}} \varrho \vec{v}\, dV \;=\; \int_{\mathcal{B}} \varrho \vec{k}\, dV \;+\; \int_{\partial\mathcal{B}} \vec{s}\, dA \tag{7.19}$$

is formulated. Without derivation in the following the CAUCHY stress tensor $\boldsymbol{\sigma}$ and its relation to the stress vector

$$\vec{s} = \boldsymbol{\sigma} \cdot \vec{n} \tag{7.20}$$

[1] In technical applications on earth $\vec{b}$ reflects only the interaction between the parts of $\mathcal{B}$ and the body of the earth itself. The gravitation acting between the different parts of $\mathcal{B}$ with each other are of importance e.g. in astrophysical problems. But even then they are described via a body force, as long as the relation "*actio equals reactio*" holds.

is used, i.e. the stress vector $\vec{s}$ is derived from $\vec{n}$ by application of a homogeneous, linear transformation. Therefore, Eq. 7.19 reads as follows

$$\int_{\mathcal{B}} \varrho \left(\frac{D}{Dt}\vec{v} - \vec{k} \right) dV \;=\; \int_{\partial\mathcal{B}} \boldsymbol{\sigma} \cdot \vec{n}\, dA \,. \tag{7.21}$$

By application of GAUSS theorem and the use of the definition of the material derivative of Eq. 7.5 the following final formulation for the momentum balance equation can be achieved

$$\varrho \frac{D}{Dt}\vec{v} \;=\; \varrho\vec{k} + \operatorname{div} \boldsymbol{\sigma} \,, \tag{7.22}$$

$$\varrho \frac{\partial}{\partial t}\vec{v}\varrho\vec{v} \cdot \operatorname{grad} \vec{v} \;=\; \varrho\vec{k} + \operatorname{div} \boldsymbol{\sigma} \,. \tag{7.23}$$

Angular Momentum Balance

Additional to the momentum balance a balance of angular momentum can be postulated. Starting with the angular momentum $\vec{L}$ of a body $\mathcal{B}$

$$\vec{L} = \int_{\mathcal{B}} \vec{x} \times \varrho\vec{v}\, dV \tag{7.24}$$

the time derivative of $\vec{L}$ is postulated as the moments of the body and surface forces

$$\frac{D}{Dt} \int_{\mathcal{B}} \vec{x} \times \varrho\vec{v}\, dV \;=\; \int_{\mathcal{B}} \vec{x} \times \varrho\vec{k}\, dV \;+\; \int_{\partial\mathcal{B}} \vec{x} \times \vec{s}\, dA \,. \tag{7.25}$$

Using that $D\vec{x}/Dt \times \vec{v} = \vec{v} \times \vec{v} = 0$ and by applying the definition of the CAUCHY stress tensor of Eq. 7.20 we obtain

$$\int_{\mathcal{B}} \vec{x} \times \varrho \frac{D}{Dt}\vec{v}\, dV \;=\; \int_{\mathcal{B}} \vec{x} \times \varrho\vec{k}\, dV \;+\; \int_{\partial\mathcal{B}} \vec{x} \times \boldsymbol{\sigma} \cdot \vec{n}\, dA \,. \tag{7.26}$$

Applying GAUSS' theorem to the equation above the surface integral can be converted into a volume integral as follows:

$$\int_{\mathcal{B}} \vec{x} \times \varrho \frac{D}{Dt}\vec{v}\, dV \;=\; \int_{\mathcal{B}} \left[\vec{x} \times (\varrho\vec{k} + \operatorname{div} \boldsymbol{\sigma}) + \vec{s}^{*} \right] dV \tag{7.27}$$

The vector $\vec{s}^{*}$ in this equation is the axial vector of $\boldsymbol{\sigma}$ with the components $e_{\alpha\beta\gamma}\sigma_{\beta\alpha}$ $(\gamma = 1, 2, 3)$ and $\boldsymbol{e}$ the permutation tensor. On the left hand side of Eq. 7.27 the momentum balance of Eq. 7.23 might be applied thus finally leading to

$$\int_{\mathcal{B}} \vec{s}^{*}\, dV = \vec{0} \,. \tag{7.28}$$

Due to the arbitrary choice of $\mathcal{B}$ the vector $\vec{s}^*$ has to obey $\vec{s}^* = 0$. Because of the meaning of $\vec{s}^*$ as an axial vector and due to the definition of $\boldsymbol{e}$ this is an equivalent formulation to

$$\sigma_{\alpha\beta} = \sigma_{\beta\alpha}, \quad \text{or} \quad \boldsymbol{\sigma} = \boldsymbol{\sigma}^{\mathrm{T}} \,. \tag{7.29}$$

In other words, the balance of the angular momentum demands the symmetry of the Cauchy stress tensor. This statement is know as the BOLTZMANN axiom, however it is only valid for classical continua. For polar media the balance equations have to be extended, as we will show in Sect. 8.1.

Constitutive Equations

The balance equations of the previous paragraphs in principle do not rely on any assumptions of the material behavior itself. However, in the kinematic paragraph the material points were only allowed to perform translational movements, thus polar materials are not captured by this type of theory. The balance equations however are universal for all non-polar kinds of materials. They prove useful for gases, fluids and solids which deform by a finite amount under external forces. Because different materials behave different under the same external forces, it is quite clear that the balance equations are not enough to completely describe the behavior of a given material. The missing equations are the *constitutive equations*. In a purely mechanical description of a material these equations relate the stresses acting on the material with its movements.

In the following we summarize the constitutive equations of an elastic material. We call a material elastic if its relation between the stress tensor and the deformation gradient may be formulated as:

$$\sigma_{\alpha\beta} = \sigma_{\alpha\beta}\left(D_{11}(\vec{X},t), \ldots, D_{33}(\vec{X},t)\right) \,. \tag{7.30}$$

The components of the stress tensor at point $\vec{X}$ at time t only depend on the elements $D_{\alpha\beta}(\vec{X},t)$ of the deformation gradient at this point and at this time. Specifically, this leads to *homogeneity* of the material because otherwise the position $\vec{X}$ would have to occur on the right side not only implicit in $D_{\alpha\beta}$ but also explicit. Additionally Eq. 7.30 uses time independence of the material law as t also enters the equation only implicit.

For an isotropic material Eq. 7.30 takes the form of HOOKEs law:

$$\boldsymbol{\sigma} = 2\mu\boldsymbol{G} + \lambda \operatorname{tr} \boldsymbol{G}\boldsymbol{I} \tag{7.31}$$

$$= 2\mu\boldsymbol{\epsilon} + \lambda \operatorname{tr} \boldsymbol{\epsilon}\boldsymbol{I} \, . \tag{7.32}$$

7.2 The Micro-Mechanical Fabric Tensor

In the classical continuum theory the microscopic (atomistic) structure of a material is not taken into account explicitly. For example, the lattice structure of metals or the movement of the molecules of a gas do not enter the constitutive equations directly. In assemblies of grains, the forces are transmitted from one particle to the next only at the contacts of the particles. Therefore, the description of the associated network of inter-particle contacts is essential, especially for the quasi-static mechanics of granular assemblies (COWIN [21]; GODDARD [35]).

In the general case of non-spherical particles, a packing network is characterized by the vectors connecting the particle centers with their contacts and by the geometry at each contact. For spherical particles the contact normal equals the direction of the center-center vector of the connected particles. Therefore, the information of the contact normals suffices to characterized the inner structure of the granular material to some extent. The fabric tensor $\boldsymbol{F}$ accomplishes this and is therefore a measure for the anisotropy of the system. Although, the fabric tensor is not a quantity of the classical continuum theory it will be investigated in this section. The way the fabric tensor is derived will show the basic principles how to measure tensorial quantities with our averaging formalism. After defining the fabric tensor for one particle and for an ensemble of grains we will demonstrate how the fabric tensor may be used to test for the isotropy of the granular structure of a material. The fabric tensor is a measure of the contact number density in a given direction in the granulate. Thus the fabric tensor may be used to test whether the grains in the material are placed in an isotropic way or if there exists some kind of ordering.

For all following derivations we limit ourself to the description of disk shaped particles.[2]

[2] Which is the equivalent to spherical particles in 3D, in the sense that contact normal

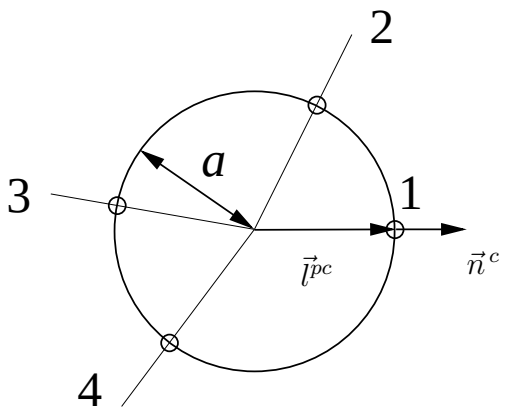

Fig. 7.3: *Schematic plot of a particle with radius a and four contacts as indicated by the small circles. The branch vector $\vec{l}^{pc}$ and the normal unit vector $\vec{n}^{\,c}$ are displayed at contact $c = 1$.*

7.2.1 The Fabric Tensor for one Particle

One quantity that describes the local configuration of the grains to some extent is the fabric tensor (GODDARD [35]) of second order

$$\boldsymbol{F}^p = \sum_{c=1}^{\mathcal{C}^p} \vec{n}^{\,c} \otimes \vec{n}^{\,c} \,, \tag{7.33}$$

where $\vec{n}^{\,c}$ is the unit normal vector at contact c of particle p. Other definitions of the fabric use the so-called branch vector $\vec{l}^{pc}$ from the center of particle p to its contact c, however, the unit normal and the unit branch vector are identical in the case of spherical particles.

Using the identity $a_p \vec{n}^{\,c} = \vec{l}^{pc}$, one has an alternative definition of the fabric tensor

$$\boldsymbol{F}^p = \frac{1}{a_p^2} \sum_{c=1}^{\mathcal{C}^p} \vec{l}^{pc} \otimes \vec{l}^{pc} \,. \tag{7.34}$$

From Eqs. 7.33 and 7.34 one obtains the number of contacts of particle p

$$\mathrm{tr}\ \boldsymbol{F}^p = \sum_{c=1}^{\mathcal{C}^p} \vec{n}^{\,c} \otimes \vec{n}^{\,c} = \mathcal{C}^p \,, \tag{7.35}$$

because the scalar product of $\vec{n}^{\,c}$ with itself is unity.

and center-center vector share the same direction.

7.2.2 The Averaged Fabric Tensor

The fabric tensor is a quantity that describes the contact network in a given volume V. Assuming that all particles lie inside V and thus contribute to the fabric tensor with a weight V^p, which can be seen as the area occupied by particle p, the fabric tensor reads as

$$\bar{\boldsymbol{F}} = \frac{1}{V} \sum_{p \in V} V^p \boldsymbol{F}^p = \frac{1}{V} \sum_{p \in V} \frac{V^p}{a_p^2} \sum_{c=1}^{\mathcal{C}^p} \vec{l}^{pc} \otimes \vec{l}^{pc} \, . \tag{7.36}$$

We can imagine different possibilities for V^p: One is to divide the volume in polygons with a VORONOI tessellation (VORONOI [106])[3] with only one particle per polygon such that the polygons cover the whole volume; in that case V^p is the volume of the polygon that contains particle p. However, we will use another possibility, i.e. we use the volume of particle p so that $V^p = \pi h a_p^2$. Inserting our definition of V^p into Eq. 7.36 leads to the averaged fabric tensor

$$\bar{\boldsymbol{F}} = \frac{\pi h}{V} \sum_{p \in V} \sum_{c=1}^{\mathcal{C}^p} \vec{l}^{pc} \otimes \vec{l}^{pc} \, . \tag{7.37}$$

In analogy to the trace of the fabric for a single particle, the trace of the averaged fabric is

$$\mathrm{tr} \; \bar{\boldsymbol{F}} = \frac{\pi h}{V} \sum_{p \in V} a_p^2 \mathcal{C}^p \, . \tag{7.38}$$

In the case of a regular, periodic contact network of identical particles (i.e. $a_p = a$), Eq. 7.38 reduces to $\mathrm{tr} \; \bar{\boldsymbol{F}} = \nu \bar{\mathcal{C}}$, where ν is the volume fraction, defined as the ratio of the volume covered by particles and the total volume:

$$\nu = \frac{1}{V} \sum_{p \in V} V^p \tag{7.39}$$

and $\bar{\mathcal{C}}$ the averaged number of contacts. This combination of Eqs. 7.38 and 7.39

$$\mathrm{tr} \; \bar{\boldsymbol{F}} = \bar{\mathcal{C}} \nu \, . \tag{7.40}$$

can be used as a test for the averaging procedure. When plotting $\mathrm{tr} \; \bar{\boldsymbol{F}}$ against $\nu \bar{\mathcal{C}}$ all points should collapse onto the identity curve. In Fig. 7.4 various simulations with different global density are found to collapse on the

[3] In 2D the plane is subdivided into polygonal domains, each of them containing exactly one particle. The borders of the domain are the bisecting lines of the straight lines connecting the centers of neighboring particles.

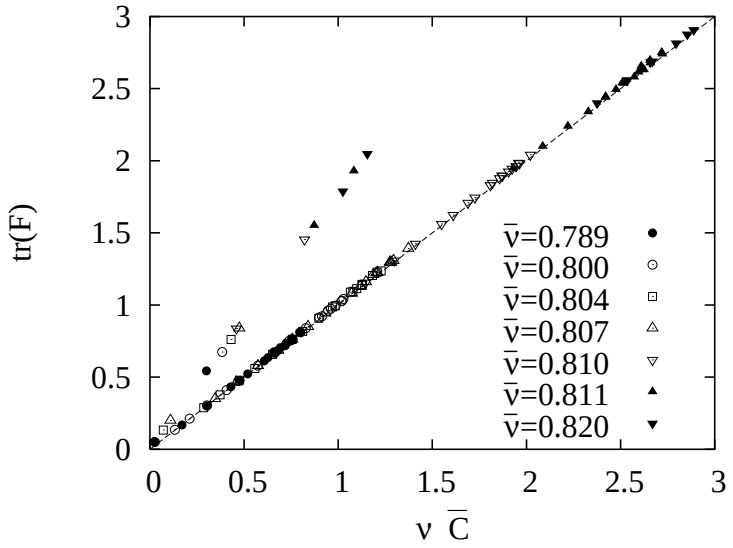

Fig. 7.4: *As a test of the averaging procedure the trace of the fabric* $\mathrm{tr}\,\bar{\boldsymbol{F}}$ *is plotted versus the mean number of contacts* $\bar{C}$ *times the volume fraction* ν*. All data points from simulations with different global density collapse on the identity curve. The deviating points result from the averaging bins adjacent to the walls, where contacts with the wall occur.*

identity curve. The points deviating from the identity curve are the points adjacent to the walls, where due to contacts with the wall $\mathrm{tr}\,(\boldsymbol{F})$ leads to higher values than $\nu\bar{C}$.

7.2.3 Properties of the Fabric Tensor

The fabric tensor in Eq. 7.33 is symmetric by definition and thus consists of up to three independent scalar quantities in two dimensions.

The first of them, the trace $F_V = \mathrm{tr}\;\boldsymbol{F} = F_{\alpha\alpha} = F_{\max} + F_{\min}$, is the number of contacts of particle p, with the major and the minor eigenvalues $F_{\max}$ and $F_{\min}$, respectively. The trace of the averaged fabric is shown in Fig. 7.5 for six simulations with different global densities. In the shear band the number of contacts is lowest and increases with increasing distance from the inner wheel. In the vicinity of the outer wall the trace of the fabric is again lowered because of ordering effects of the particles. With increasing global density the particles are packed more dense, thus the average number of contacts for the particles increases likewise.

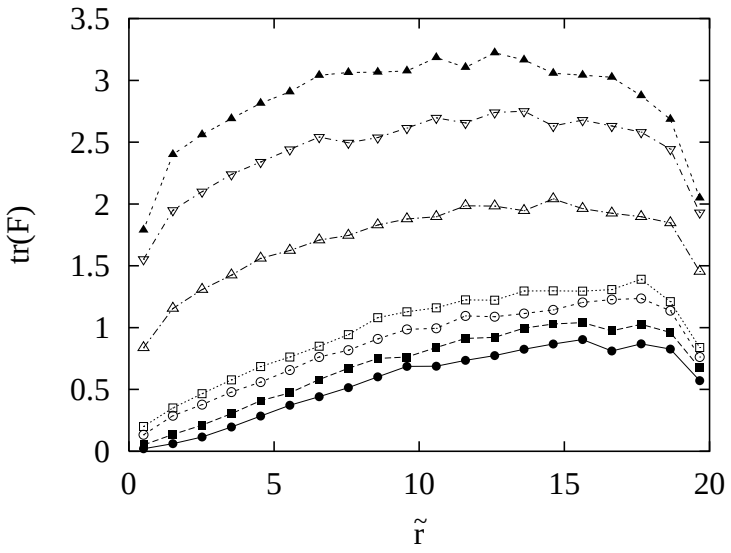

Fig. 7.5: *The trace of the fabric tensor* $\mathrm{tr}\,\boldsymbol{F}$ *plotted against the dimensionless distance from the inner wheel for different global densities. The symbols refer to the same simulations as given in Fig. 7.6.*

The second independent scalar quantity of the fabric tensor accounts for the magnitude of the anisotropy of the contact network in first order $F_D = F_{\max} - F_{\min}$ and is called the deviator. In order to compare the deviator of different simulations the deviatoric fraction F_D/F_V is used and plotted in Fig. 7.6. The deviatoric fraction seems to decrease while increasing the mean density. This means that a denser system is slightly more isotropic concerning the fabric. Figure 7.6 also indicates that the fabric is more anisotropic in the inner part of the shear device and more isotropic in the outer part where fewer reorganizations take place. This behavior will also be shown in the next section by means of the contact probability distribution.

As third independent scalar quantity of the fabric tensor the angle ϕ that gives the orientation of the major eigenvector with respect to the radial outwards direction is examined. The major eigendirection is shown in Fig. 7.7. The eigendirection is tilted counterclockwise[4] by somewhat more than $\pi/4$ from the radial outward direction, except for the innermost layer and for the strongly fluctuating outer region. However, these fluctuations of the eigendirection in the outer part are due to the more isotropic structure of the fabric, i.e. for a perfect isotropic fabric the eigendirection is not well defined.

[4] In direction of the shear motion.

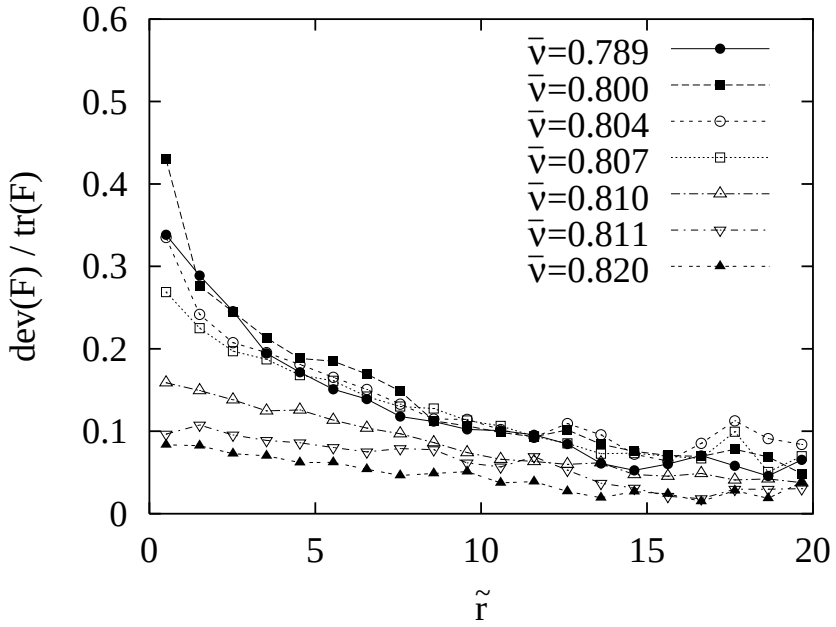

Fig. 7.6: *The deviatoric fraction of the fabric is plotted versus the dimensionless distance from the inner wheel for different global densities.*

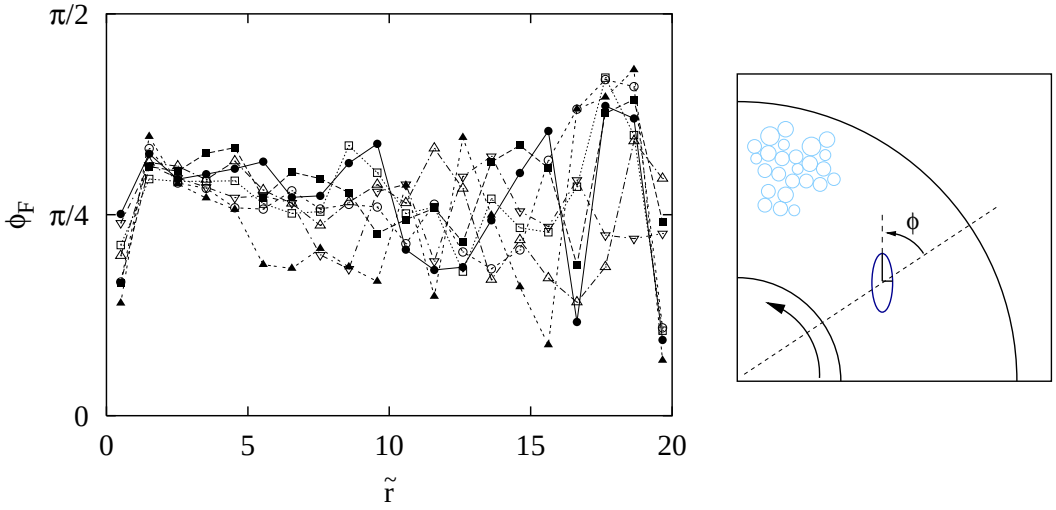

Fig. 7.7: *The figure shows the orientation of the major eigenvector of the fabric with respect to the radial outwards direction. The definition of ϕ is shown in the right panel.*

As already mentioned the question of the isotropy of the fabric can be addressed in more detail by the contact probability distribution of the fabric, as done in the next section.

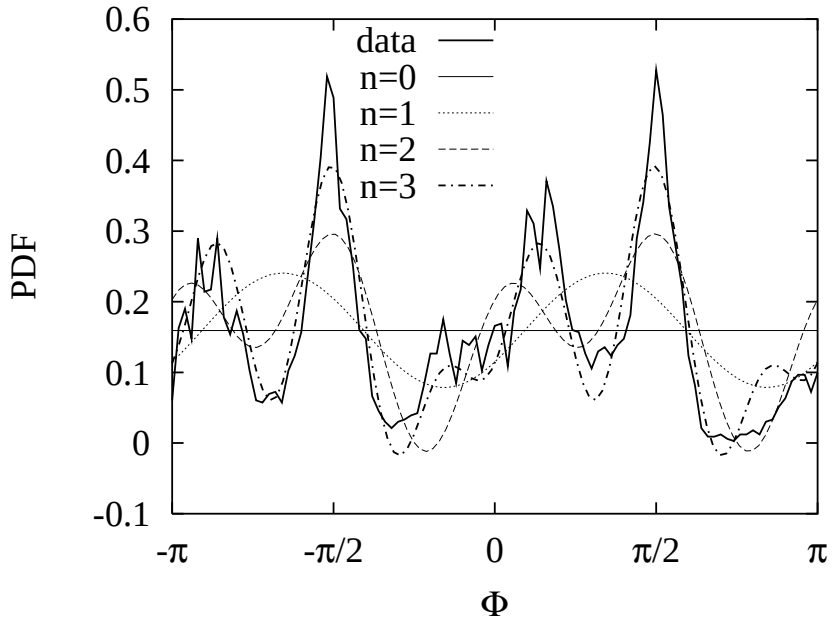

Fig. 7.8: *Probability distribution of contacts in a given direction of the particles in a one particle wide ring at the inner ring of the shearing device. The data are obtained from a simulation with* $\bar{\nu} = 0.804$. $\Phi = 0$ *denotes the radial outward direction like defined in Fig. 7.7. The lines are fits to the data taking into account terms of the form* $\sin(2n * x + \psi)$ *with* $n = 0, 1, 2, 3$.

7.2.4 Contact Probability Distribution

The fabric tensor was used in the previous section to describe the inner structure of the contact network of the particles. In particular the major eigendirection of the fabric may be used to predict in which direction to find most of the contacts of the particles.

To test whether a system is isotropic or anisotropic it is helpful to plot the probability distribution to find a contact in a given direction of a particle. In Fig. 7.8 this probability is plotted for the particles in a one particle wide ring at the inner shearing wheel for a simulation with $\bar{\nu} = 0.804$. Because of the rotational symmetry of the system the probability distribution is 2π-periodic, where $\Phi = 0$ denotes the radial outward direction. The straight line in the plot at 0.16 is the mean value given by $1/(2\pi)$. If the data of Fig. 7.8 are plotted in polar coordinates (see Fig. 7.9a)) the mean resembles a circle. With the second rank tensor used throughout this thesis only dipole moments of the contact probability function are taken into account. Thus

the shape of the probability distribution is approximated by the dotted line in Fig. 7.8. To fully describe the structure of the probability distribution higher order fabric tensors have to be used

$$\boldsymbol{F}^p = \sum_{c=1}^{\mathcal{C}^p} \vec{n}^{\,c} \otimes \vec{n}^{\,c} \otimes \vec{n}^{\,c} \otimes \vec{n}^{\,c} \otimes \cdots \,, \tag{7.41}$$

thus also considering quadrupole, octupole, ... moments (GODDARD [35]; MEHRABADI ET AL. [62]) as shown by the dashed and dashed-dotted line in Fig. 7.8.[5]

This approach is beyond the scope of this thesis. For clarity we plot representative contact probabilities from a simulation with $\bar{\nu} = 0.804$. The system reveals a complex structure which changes from the inner to the outer part of the shear device. This transition is shown in the subfigures of Fig. 7.9 and reveals distinct differences between different radial areas.

In the shear zone (Fig. 7.9a) and Fig. 7.9b)) a triangular structure with preferred angles $\pi/2$ is obvious together with an underpopulation at $5\pi/6$ and an overpopulation at $\pi/6$. Farther outside, this structure softens (Fig. 7.9c)) and the distribution is more homogeneous (see Fig. 7.9d) and Fig. 7.9e)). Near the outer ring (Fig. 7.9f)), again a very distinct triangular structure occurs, but now, additional peaks at $-\pi/6$ occur with comparable probability as at $\pi/6$.

The angles $-\pi/6$, $\pi/6$ and $\pi/2$ correspond to an annular triangular lattice or, in other words, the disks are located in annular layers. Inside the shear zone, this structure is reasonable because it may allow sliding of the layers. Outside the shear zone neither dilation nor geometrical order due to a wall foster the forming of structures, therefore a more homogeneous distribution is found. The repeated occurrence of the annular triangular lattice near the outer boundary cannot be ascribed to the shearing and following dilation. It is formed during the initial compression of the shear cell, and resembles the "remembering" of the triangular lattice due to the near mono-disperse size distribution of the particles as a near-order wall-effect close to the almost flat outer wall.

[5] Actually the lines in Fig. 7.8 are fits with $f^0(x) = a_0$, $f^2(x) = a + b * \sin(2 * x + c)$, $f^4(x) = a + b * \sin(2 * x + c) + d * \sin(4 * x + e)$ and $f^6(x) = a + b * \sin(2 * x + c) + d * \sin(4 * x + e) + f * \sin(6 * x + g)$ each taking into account a moment of higher order than the previous one.

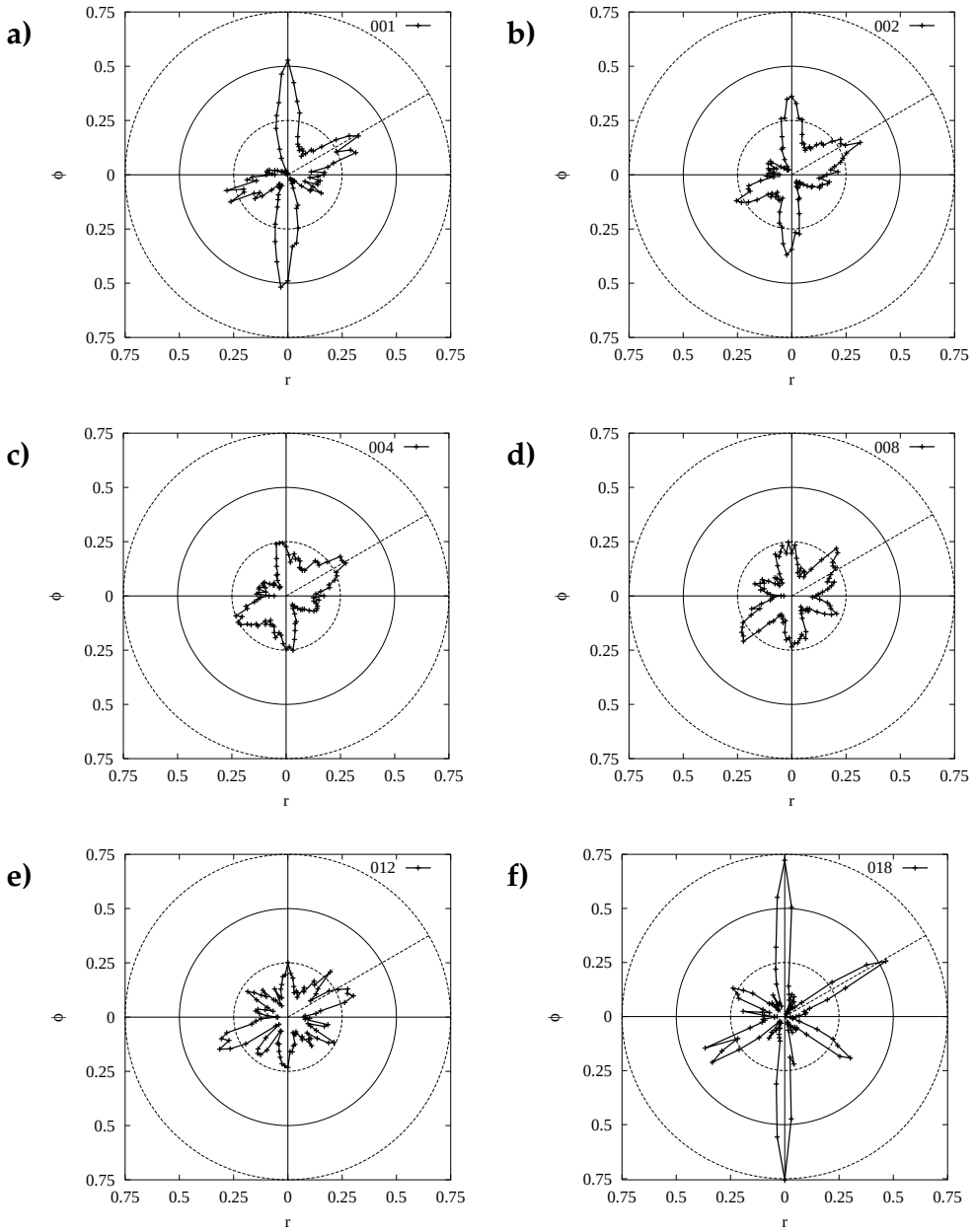

Fig. 7.9: *Probability to find a contact in a given direction of a particle. An angle of* $\Phi = 0$ *denotes the radial outwards direction, the dashed line resembles an angle of* $\Phi = \pi/6$*. The data are shown for an area of width one particle directly at the shearing device in plot* **a)**. *In the subplots* **b)-e)** *averaging areas* $2, 4, 8$ *and* 12 *particle diameters away from the inner ring are investigated, whereas the data of plot* **f)** *are taken at the outer ring. All data stem from a simulation with* $\bar{\nu} = 0.804$.

7.3 The Dynamical Micro-Mechanical Stress Tensor

The micro-mechanical approach models the material as an assembly of (semi)-rigid particles interacting by contact forces. In order to describe the behavior of the assembly under external loading the aim of the micro-mechanical approach is to find macroscopic state variables through a proper averaging of microscopic variables. In the following a definition of the stress based on microscopic variables is given, following this route. In contrast to previous work (BAGI [5]; CAMBOU ET AL. [14]; CHRISTOFFERSON ET AL. [18]; KRUYT AND ROTHENBURG [47]; LIAO ET AL. [51]; ROTHENBURG AND SELVADURAI [83]) in this field we derive the *complete dynamical* micro-mechanical stress tensor.

For an arbitrary volume V with surface ∂V, the mean stress is defined as

$$\bar{\boldsymbol{\sigma}} = \frac{1}{V} \int_V dV' \, \boldsymbol{\sigma} \, , \tag{7.42}$$

where $\boldsymbol{\sigma} = \boldsymbol{\sigma}(\vec{x})$ is a function of the position of volume element dV' inside V which might strongly fluctuate.

In the framework of the theory of porous media the stress in the pore space might be neglected, e.g. if it is occupied by gas. We adopt this for our granulate, i.e. only the grains are able to carry stresses. Therefore, the above integral turns into a sum over the stresses pre-averaged for particles p. This operation enables us to deal with particle averages instead of volume averages later on. Eq. 7.42 thus reads

$$\bar{\boldsymbol{\sigma}} = \frac{1}{V} \sum_{p \in V} \int_{V^p} dV' \, \boldsymbol{\sigma} \, , \tag{7.43}$$

$$= \frac{1}{V} \sum_{p \in V} V^p \boldsymbol{\sigma}^p \, . \tag{7.44}$$

The integral signifies the pre-averaging of $\boldsymbol{\sigma}$ over the particles. The averaged stress

$$\boldsymbol{\sigma}^p = \frac{1}{V^p} \int_{V^p} dV' \boldsymbol{\sigma} \tag{7.45}$$

of one particle is derived in the following, before the averaging procedure is used on it, in order to finally achieve the averaged stress in the sample. The properties of the stress in our system are shown in Section 7.3.3 and are being compared to the stresses predicted by a continuum approach.

7.3.1 The Mean Stress for one Particle

For the sake of simplicity the superscript p indicating a particle quantity will be dropped, though we deal with one specified particle. It will turn out more handy to start with the transposed stress tensor $\boldsymbol{\sigma}^T$ instead of $\boldsymbol{\sigma}$. By introducing the unit tensor $\boldsymbol{I} = \text{grad } \vec{x}$ the transposed stress becomes

$$\boldsymbol{\sigma}^T = \text{grad } \vec{x}\boldsymbol{\sigma}^T = \text{div } (\vec{x} \otimes \boldsymbol{\sigma}) - \vec{x} \otimes \text{div } \boldsymbol{\sigma} \, . \tag{7.46}$$

The law of momentum balance (see Eq. 7.23) in the EULERian reference frame, for the volume occupied by particle p at time t, reads

$$\varrho\ddot{\vec{x}} + \varrho\vec{v} \cdot \text{grad } \vec{v} = \text{div } \boldsymbol{\sigma} + \varrho\vec{k} \, , \tag{7.47}$$

where the dots denote the partial derivatives with respect to time and $\vec{k}$ represents an external acceleration, e.g. gravity. Inserting Eqs. 7.46 and 7.47 in Eq. 7.45 yields

$$\bar{\boldsymbol{\sigma}}^T = \frac{1}{V^p} \left[\underbrace{\int_{\partial V^p} \vec{x} \otimes \boldsymbol{\sigma} \cdot d\vec{A}}_{\bar{\boldsymbol{\sigma}}_s^T} - \underbrace{\int_{V^p} \vec{x} \otimes \varrho(\ddot{\vec{x}} - \vec{k}) dV'}_{-\bar{\boldsymbol{\sigma}}_v^T} - \underbrace{\int_{V^p} \vec{x} \otimes \varrho(\vec{v} \cdot \text{grad } \vec{v}) dV'}_{-\bar{\boldsymbol{\sigma}}_d^T} \right] \tag{7.48}$$

and the three parts namely the surface integral $\bar{\boldsymbol{\sigma}}_s^T$, the volume integral $\bar{\boldsymbol{\sigma}}_v^T$ and the kinetic part $\bar{\boldsymbol{\sigma}}_d^T$ will be addressed separately below.

The Surface Integral

Using the CAUCHY theorem $\vec{s} = \boldsymbol{\sigma} \cdot \vec{n}$ and the definition $d\vec{A} = \vec{n}dA$, with $\vec{n}$ the normal to the boundary ∂V^p of particle p, the first part of Eq. 7.48 transforms into a sum

$$\bar{\boldsymbol{\sigma}}_s^T = \frac{1}{V^p} \int_{\partial V^p} (\vec{x} \otimes \vec{s} \,) \, dA = \frac{1}{V^p} \sum_{c=1}^{\mathcal{C}} \vec{x}^c \otimes \vec{f}^c \, , \tag{7.49}$$

after replacing the surface stresses active at the contacts by the corresponding forces $\vec{f}^c$.[6]

[6] Here we assume a small contact area δs with constant $\vec{s} = f/(\delta s)$.

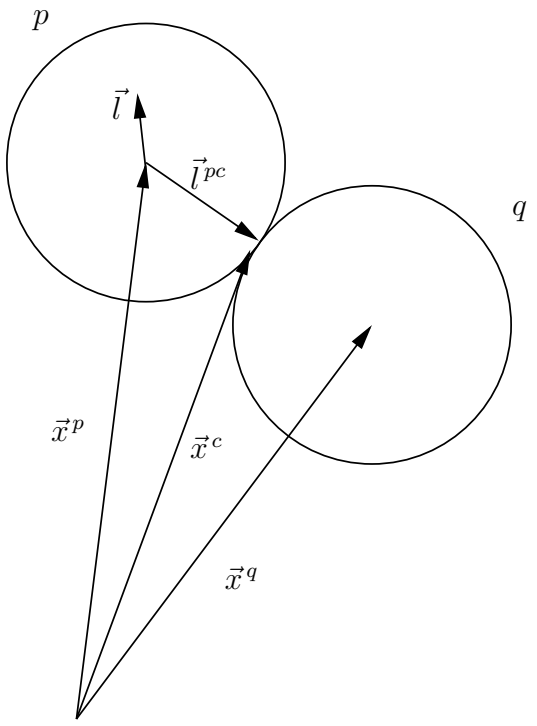

Fig. 7.10: *Schematic plot of two particles p and q with their common contact c.*

Introducing the branch vector $\vec{l}^{pc}$ by the vector addition $\vec{x}^{c} = \vec{x}^{p} + \vec{l}^{pc}$, as shown in Fig. 7.10, leads to

$$\bar{\boldsymbol{\sigma}}_s^T = \frac{1}{V^p}\left[\vec{x}^{p} \otimes \sum_{c=1}^{\mathcal{C}} \vec{f}^{\,c} + \sum_{c=1}^{\mathcal{C}} \vec{l}^{pc} \otimes \vec{f}^{\,c}\right] . \tag{7.50}$$

With NEWTONs law for the motion of particle p with mass m,

$$m\ddot{\vec{x}}^{p} = \sum_{c=1}^{\mathcal{C}} \vec{f}^{\,c} + m\vec{k} \,, \tag{7.51}$$

we finally derive

$$\bar{\boldsymbol{\sigma}}_s^T = \frac{1}{V^p}\left[m\vec{x}^{p} \otimes (\ddot{\vec{x}}^{p} - \vec{k}) + \sum_{c=1}^{\mathcal{C}} \vec{l}^{pc} \otimes \vec{f}^{c}\right] \tag{7.52}$$

for the first integral in Eq. 7.48. For static equilibrium both acceleration (2^{nd} term) and torque (4^{th} term) vanish.

The Volume Integral

The volume integral

$$\bar{\boldsymbol{\sigma}}_v^T = -\frac{1}{V^p}\int_{V^p}\left(\vec{x}\otimes\varrho\ddot{\vec{x}} - \vec{x}\otimes\varrho\vec{k}\right)dV' \tag{7.53}$$

contains those terms acting on all material points of particle p. Therefore, one has to introduce a vector $\vec{l}$ which points from the center of mass of the particle to the material points inside so that $\vec{x} = \vec{x}^p + \vec{l}$, see Fig. 7.10.

This leads to

$$\bar{\boldsymbol{\sigma}}_v^T = -\frac{1}{V^p}\int_{V^p}(\vec{x}^p + \vec{l})\otimes\varrho\left(\ddot{\vec{x}}^p + \ddot{\vec{l}} - \vec{k}\right)dV' \,, \tag{7.54}$$

where the vectors $\vec{x}^p$ and $\vec{k}$ are constant, so that they can be taken out of the integral. The integral $\int_{V^p}\varrho dV'$ is the mass m of the particle as implied in the following. In separate terms the stress reads

$$\begin{aligned}
\bar{\boldsymbol{\sigma}}_v^T = -\ \tfrac{1}{V^p}\Big[\ & +m\vec{x}^p\otimes\ddot{\vec{x}}^p && (7.55)\\
& +\vec{x}^p\otimes\int_{V^p}\varrho\ddot{\vec{l}}dV' && (7.56)\\
& -m\vec{x}^p\otimes\vec{k} && (7.57)\\
& +\left(\int_{V^p}\varrho\vec{l}dV'\right)\otimes\ddot{\vec{x}}^p && (7.58)\\
& +\int_{V^p}\varrho\vec{l}\otimes\ddot{\vec{l}}dV' && (7.59)\\
& -\left(\int_{V^p}\varrho\vec{l}dV'\right)\otimes\vec{k}\ \Big] && (7.60)
\end{aligned}$$

The fourth term, Eq. 7.58, and the sixth term, Eq. 7.60, vanish due to the fact that $\int_{V^p}\varrho\vec{l}dV'$ is the definition of the center of mass and $\vec{l}$ is defined relative to the center of mass. For the rotational motion of a rigid body with angular velocity ω around its center of mass one has

$$\begin{aligned}
\dot{\vec{l}} &= \vec{\omega}\times\vec{l}\,, \text{ and}\\
\ddot{\vec{l}} &= \dot{\vec{\omega}}\times\vec{l} + \vec{\omega}\times\dot{\vec{l}}\\
&= \dot{\vec{\omega}}\times\vec{l} + \vec{\omega}\times(\vec{\omega}\times\vec{l})\,,
\end{aligned} \tag{7.61}$$

so that also the second term, Eq. 7.56, equals zero because both $\vec{\omega}$ and $\dot{\vec{\omega}}$ are constant over the rigid particle and thus can be drawn out of the integral. Finally, using $\vec{\omega}\times(\vec{\omega}\times\vec{l}) = \vec{\omega}(\vec{\omega}\cdot\vec{l}) - \vec{l}(\omega^2) = -\vec{l}(\omega^2)$, since $\vec{\omega}$ and $\vec{l}$ are

perpendicular in 2D disks rotating around their axis of rotational symmetry, one obtains

$$\bar{\boldsymbol{\sigma}}_v^T = -\frac{1}{V^p}\left[m\vec{x}^p \otimes (\ddot{\vec{x}}^p - \vec{k}) + \int_{V^p} \varrho\vec{l} \otimes (\dot{\vec{\omega}} \times \vec{l} - \omega^2\vec{l})dV'\right] . \tag{7.62}$$

Using the identity $\vec{l} \otimes (\dot{\vec{\omega}} \times \vec{l}) = -(\vec{l} \otimes \vec{l}) \times \dot{\vec{\omega}}$ and drawing the constants out of the integrals, yields

$$\bar{\boldsymbol{\sigma}}_v^T = -\frac{1}{V^p}\left[m\vec{x}^p \otimes (\ddot{\vec{x}}^p - \vec{k}) - \boldsymbol{\theta} \times \dot{\vec{\omega}} - \omega^2\boldsymbol{\theta}\right] , \tag{7.63}$$

after introducing the symmetric tensor $\boldsymbol{\theta} := \int_{V^p} \varrho\vec{l} \otimes \vec{l}$.

The Dynamic Stress

The integral

$$\bar{\boldsymbol{\sigma}}_d^T = -\frac{1}{V^p}\int_{V^p} \varrho\,(\vec{x} \otimes \vec{v} \cdot \mathrm{grad}\ \vec{v})\,dV' \tag{7.64}$$

can be simplified by transforming the components of the term in brackets

$$-\,x_\alpha v_\gamma v_{\beta,\gamma} = -(x_\alpha v_\gamma v_\beta)_{,\gamma} + x_{\alpha,\gamma} v_\gamma v_\beta \; + x_\alpha v_{\gamma,\gamma} v_\beta \; , \tag{7.65}$$

where the $,\gamma$ is an abbreviation for the gradient. The last term on the r.h.s. vanishes due to the assumed incompressibility of the particles $v_{\gamma,\gamma} = 0$. The first term can be transformed into a surface integral using the CAUCHY theorem. However, it vanishes because the surface integral of the normal velocity, $\vec{v} \cdot \vec{n} = \vec{v}^p \cdot \vec{n}$, vanishes due to the symmetric particle shape. The second integral survives and, after replacing $\mathrm{grad}\ \vec{x}$ by the unit tensor, has to be treated in a way similar to the volume integral in the previous subsection. Therefore, we replace the vector $\vec{v}$ by $\dot{\vec{x}} = \dot{\vec{x}}^p + \dot{\vec{l}}$, so that

$$\bar{\boldsymbol{\sigma}}_d^T = \frac{1}{V^p}\int_{V^p} \left(\varrho(\dot{\vec{x}}^p + \dot{\vec{l}}) \otimes (\dot{\vec{x}}^p + \dot{\vec{l}})\right) dV' . \tag{7.66}$$

Since the mixed terms contain $\dot{\vec{x}}^p \otimes \dot{\vec{l}}$ they vanish due to the definition of $\vec{l}$. The dyadic velocity tensor $\varrho\dot{\vec{x}}^p \otimes \dot{\vec{x}}^p$ can be easily integrated so that the remaining integral contains

$$\dot{\vec{l}} \otimes \dot{\vec{l}} = (\vec{\omega} \times \vec{l}) \otimes (\vec{\omega} \times \vec{l}) = \omega^2(l^2\boldsymbol{I} - \vec{l} \otimes \vec{l}) . \tag{7.67}$$

The integral over the term in brackets is the definition for the moment of inertia tensor $\boldsymbol{J}$. For our disk shaped particles the integral leads to $\boldsymbol{J} = (m/4)a^2\boldsymbol{I}$. Therefore, the the dynamic stress is

$$\bar{\boldsymbol{\sigma}}_d^T = \varrho\left[\vec{v}^p \otimes \vec{v}^p + \frac{1}{4}a^2\omega^2\boldsymbol{I}\right] \tag{7.68}$$

The Combined Stress

Inserting Eqs. 7.52, 7.63, and 7.68 in Eq. 7.48, finally leads to

$$\bar{\boldsymbol{\sigma}}^T = \frac{1}{V^p}\left[\sum_{c=1}^{\mathcal{C}} \vec{l}^{pc} \otimes \vec{f}^c + m\vec{v}^p \otimes \vec{v}^p + \boldsymbol{\theta} \times \dot{\vec{\omega}} + \boldsymbol{J}\omega^2 + \boldsymbol{\theta}\omega^2\right], \tag{7.69}$$

For axisymmetric particles like our disks the two last term are the same, thus the final equation reads

$$\bar{\boldsymbol{\sigma}}^T = \frac{1}{V^p}\left[\sum_{c=1}^{\mathcal{C}} \vec{l}^{pc} \otimes \vec{f}^c + m\vec{v}^p \otimes \vec{v}^p + \boldsymbol{\theta} \times \dot{\vec{\omega}} + 2\boldsymbol{J}\omega^2\right], \tag{7.70}$$

Note that the term containing $\ddot{\vec{x}}^p - \vec{k}$ cancels in the combination of the stresses.

The first term in Eq. 7.70 is the well-known, static contribution to the stress tensor and the second term is the dynamic contribution due to the particle motion with respect to the Eulerian reference frame (for details see the kinetic theory of gases (HANSEN AND MCDONALD [38]; PÖSCHEL AND LUDING [78])), i.e. a kinetic energy density.

The third, asymmetric term is related to the change of angular velocity and, thus, couples the translational degrees of freedom to the rotational motion via torques. For disks application of the integral yields

$$\boldsymbol{\theta} \times \dot{\vec{\omega}} = \boldsymbol{I} \times \sum_{c=1}^{\mathcal{C}} \vec{l}^{pc} \times \vec{f}^{t\,c} \tag{7.71}$$

with $\dot{\vec{L}} \equiv \boldsymbol{J} \cdot \dot{\vec{\omega}} = \sum_{c=1}^{\mathcal{C}} \vec{l}^{pc} \times \vec{f}^{t\,c}$ and $\vec{f}^{t\,c}$ the tangential forces at the contact for disks the integral over $\boldsymbol{\theta}$ equals $\boldsymbol{J}$. By using the contraction of indices[7] on the cross product the combined stress tensor finally reads

$$\bar{\sigma}^T_{\alpha\beta} = \frac{1}{V^p}\left[\sum_{c=1}^{\mathcal{C}} l^{pc}_\alpha f^c_\beta + m v^p_\alpha v^p_\beta + \sum_{c=1}^{\mathcal{C}} \left(l^{pc}_\beta f^t_\alpha - l^{pc}_\alpha f^t_\beta\right) + \frac{1}{2} m a^2 \omega^2 \delta_{\alpha\beta}\right]. \tag{7.72}$$

By decomposing the force vector of the first sum into normal and tangential parts we write

$$\bar{\sigma}^T_{\alpha\beta} = \frac{1}{V^p}\left[\sum_{c=1}^{\mathcal{C}} (l^{pc}_\alpha f^{n\,c}_{\ \beta} + l^{pc}_\beta f^{t\,c}_{\ \alpha}) + m v^p_\alpha v^p_\beta + \frac{1}{2} m a^2 \omega^2 \delta_{\alpha\beta}\right]. \tag{7.73}$$

[7] $\sigma^{\text{torque}}_{\alpha\beta} = e_{\beta\gamma\delta}\theta_{\alpha\gamma}\dot{\omega}_\delta = e_{\beta\gamma\delta}\delta_{\alpha\gamma}e_{\delta\epsilon\phi}l^{pc}_\epsilon f_\phi = \delta_{\alpha\gamma}l^{pc}_\epsilon f_\phi e_{\beta\gamma\delta}e_{\delta\epsilon\phi} = \delta_{\alpha\gamma}l^{pc}_\epsilon f_\phi e_{\beta\gamma\delta}e_{\epsilon\phi\delta}$. Contraction of indices yields $\sigma^{\text{torque}}_{\alpha\beta} = \delta_{\alpha\gamma}l^{pc}_\epsilon f_\phi(\delta_{\beta\epsilon}\delta_{\gamma\phi} - \delta_{\beta\phi}\delta_{\gamma\epsilon}) = (\delta_{\alpha\phi}l^{pc}_\beta f_\phi - \delta_{\alpha\epsilon}l^{pc}_\epsilon f_\beta) = (l^{pc}_\beta f_\alpha - l^{pc}_\alpha f_\beta)$.

In our case of a linear force law in normal as well as in tangential direction we finally find

$$\bar{\sigma}^T_{\alpha\beta} = \frac{1}{V^p}\left[\sum_{c=1}^{\mathcal{C}}(l^{pc}k^n(\delta n_\alpha n_\beta + \delta^{\text{tangential}}\frac{k^t}{k^n}t_\alpha n_\beta)) + mv^p_\alpha v^p_\beta + \frac{1}{2}ma^2\omega^2\delta_{\alpha\beta}\right] . \tag{7.74}$$

7.3.2 The Averaged Stress Tensor

For the sake of simplicity in the following only the first part of Eq. 7.70 is taken into account. This corresponds to a case with slow motions $\vec{v} \approx 0$, $\omega \approx 0$ and quasi steady state $\dot{\omega} \approx 0$. Still, the averaging procedure holds also for the complete equation.

Inserting Eq. 7.70 in Eq. 7.44 gives a double sum over all particles with center inside the averaging volume V, and all their contacts

$$\bar{\boldsymbol{\sigma}} = \frac{1}{V}\sum_{p\in V}\sum_{c=1}^{\mathcal{C}^p}\vec{f}^c \otimes \vec{l}^{pc} . \tag{7.75}$$

Note that Eq. 7.70 uses the transposed stress tensor, thus the order of the force and the branch vector changes in the above equation.

With our averaging formalism the weight factor w^p_V has to be added so that finally

$$\boldsymbol{\sigma} = \bar{\boldsymbol{\sigma}} = \frac{1}{V}\sum_{p\in V} w^p_V \sum_{c=1}^{\mathcal{C}^p}\vec{f}^c \otimes \vec{l}^{pc} \tag{7.76}$$

is obtained.

To that end we can summarize: The "static equilibrium" stress tensor is proportional to the dyadic product of the force $\vec{f}^c$ acting at a contact c with its branch vector $\vec{l}^{pc}$, which accounts for the distance over which the force is transmitted.

7.3.3 Behavior of the Stress

In this section the properties of the stress tensor obtain in our simulations are shown.

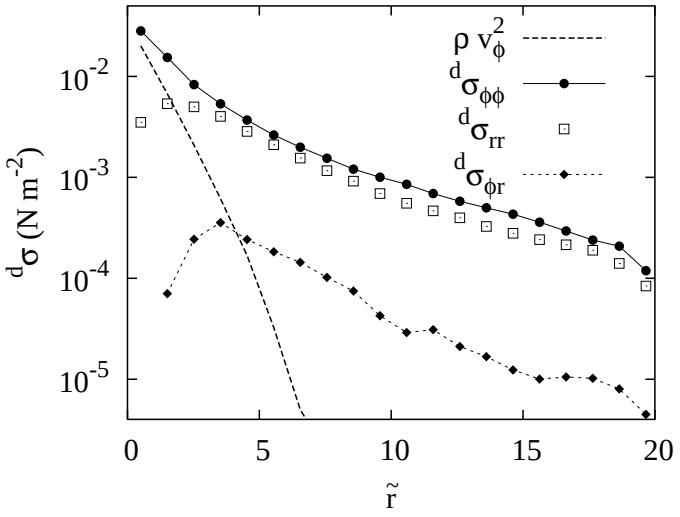

Fig. 7.11: *The dynamic stress $^d\boldsymbol{\sigma}$, and the fluctuation contribution ϱv_ϕ^2, plotted against the dimensionless distance from the center $\tilde{r}$.*

As a first test the influence of the dynamical part of the stress tensor as given by Eq. 7.68 is investigated. For the sake of simplicity and because the terms involving ω are by orders of magnitude smaller than the remaining dynamical component of the stress tensor we use

$$\boldsymbol{\sigma}_d = \langle \boldsymbol{\sigma}_d^p \rangle = \frac{1}{V} \sum_{p \in V} w_V^p V^p \rho^p \vec{v}^p \otimes \vec{v}^p \; . \tag{7.77}$$

This tensor has two contributions: (i) the stress due to velocity fluctuations around the mean and (ii) the stress $^d\sigma_{\phi\phi} \sim \rho v_\phi^2$ due to the mean mass transport in ϕ-direction.[8] In Fig. 7.11, the dynamic contribution to the stress tensor is plotted. From the dynamic stress tensor, one obtains $^d\sigma_{\phi\phi} >^d \sigma_{rr} >^d \sigma_{\phi r}$; the velocity fluctuations lead to a small stress in all components, decreasing exponentially with increasing r. The angular velocity in the shear zone strongly contributes to $^d\sigma_{\phi\phi}$, however, the dynamic stress is two orders of magnitude smaller than the static stress, as can be seen by comparison with Fig. 7.12. Therefore, when referring to the stress tensor, we only address the static part of the stress tensor and neglect the dynamical influence. In Fig. 7.12, the static contributions of the stress are plotted. In our system, the diagonal elements of the static stress are almost constant,

[8] For better readability we shifted the index ^{d} in front of the tensor in order to address components $_{\alpha\beta}$ by subscripts so that the tensor reads $^d\sigma_{\alpha\beta}$.

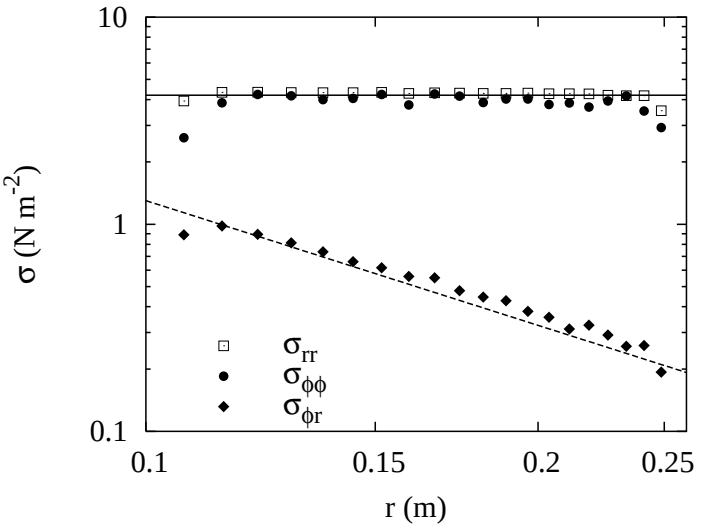

Fig. 7.12: *Components of the static stress $\boldsymbol{\sigma}$ plotted against the distance from the center r. The diagonal elements of the static stress are almost constant, whereas the off-diagonal elements decay proportional to r^{-2}, as indicated by the lines.*

whereas the off-diagonal elements decay proportional to r^{-2}, as indicated by the solid and dashed lines, respectively. This behavior is in complete agreement with the predictions of a linear elastic continuum theory as outlined in the following.

Imposing a steady state situation ($\partial/\partial t = 0$) and using the axial symmetry of the shear cell ($\partial/\partial\phi = 0$), the divergence of the stress tensor in the 2D system yields:

$$\vec{\nabla} \cdot \boldsymbol{\sigma} = \left[\frac{1}{r}\frac{\partial(r\sigma_{rr})}{\partial r} - \frac{1}{r}\sigma_{\phi\phi}\right]\vec{e}_r + \left[\frac{1}{r}\frac{\partial(r\sigma_{r\phi})}{\partial r} + \frac{1}{r}\sigma_{\phi r}\right]\vec{e}_\phi \ , \tag{7.78}$$

with the unit vectors $\vec{e}_r$ and $\vec{e}_\phi$ in radial outwards and in tangential direction, respectively. The indices r and ϕ denote the corresponding components of $\boldsymbol{\sigma}$. In static equilibrium, both components should vanish independently of each other, so that one obtains

$$\frac{\partial(r\sigma_{rr})}{\partial r} = \sigma_{\phi\phi} \qquad \text{and} \qquad \frac{\partial(r\sigma_{r\phi})}{\partial r} = -\sigma_{\phi r} \ . \tag{7.79}$$

If the diagonal and the off-diagonal elements of $\boldsymbol{\sigma}$ depend on r pairwise in the same way, the above equations lead to

$$\sigma_{rr} \propto \sigma_{\phi\phi} \propto r^0 \qquad \text{and} \qquad \sigma_{r\phi} \propto \sigma_{\phi r} \propto r^{-2} \ . \tag{7.80}$$

This result is consistent with the numerical data presented in Fig. 7.12 as indicated by the lines.

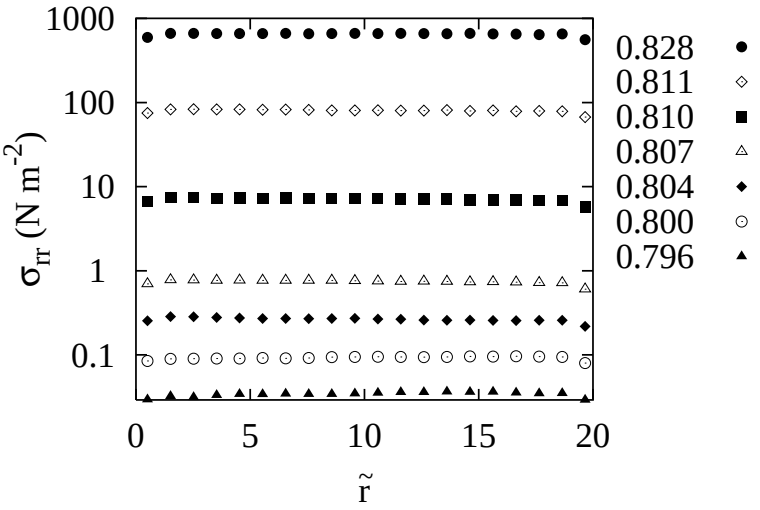

(a) The σ_{rr} components of the static stress.

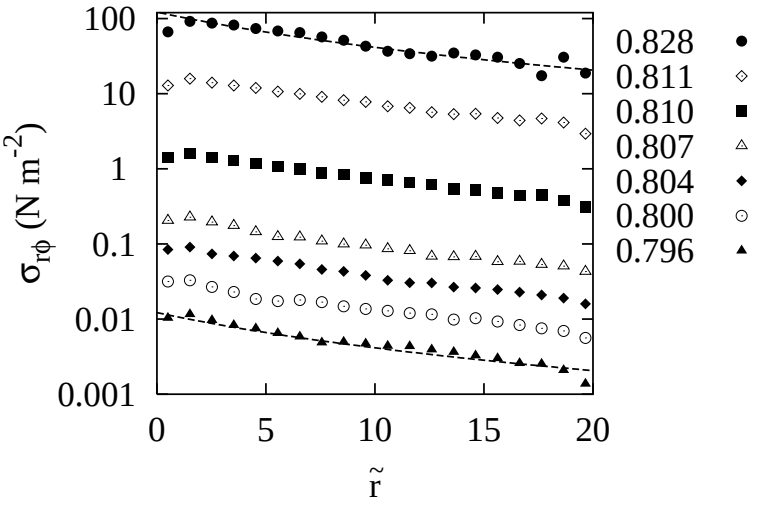

(b) The $\sigma_{r\phi}$ components of the static stress

Fig. 7.13: *The components of the static stress plotted against the dimensionless distance from the center $\tilde{r}$ for different initial densities $\bar{\nu}$.*

Another question is how the stress depends on the initial packing fraction. Figure 7.13 shows the σ_{rr} and $\sigma_{r\phi}$ components for various initial packing

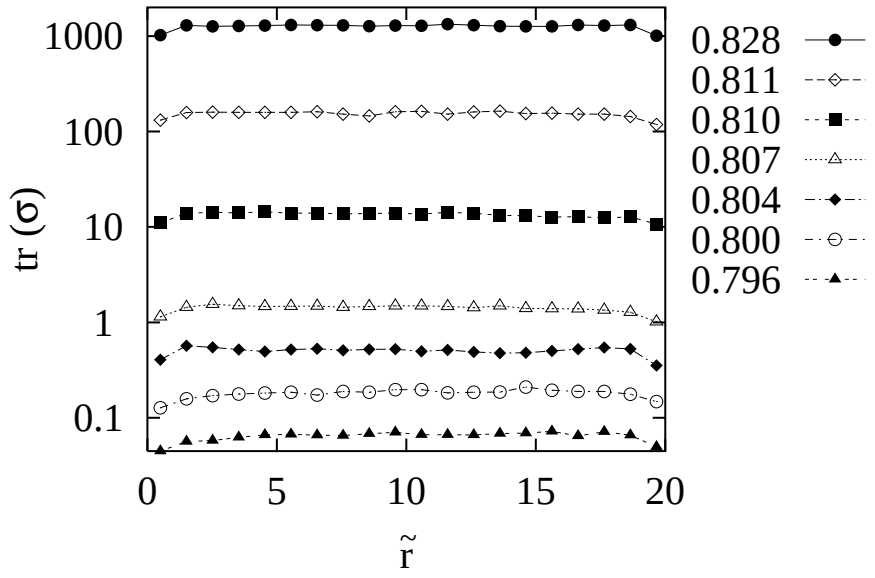

Fig. 7.14: *The trace of the stress tensor* $\mathrm{tr}\,(\boldsymbol{\sigma})$ *versus the dimensionless distance from the inner ring for various global densities.*

fractions. The stress of the diagonal elements of the stress tensor, as well as the off-diagonal elements increase with increasing initial packing fraction, as shown in Figure 7.13. This behavior is obvious, as more and more particles should lead to a more "stressed" packing.

As in the section on the fabric tensor we close this section with a look on the eigen values of the stress tensor. Figure 7.14 shows the trace of the stress tensor versus the distance from the inner wall for various simulations. The dependence on $\tilde{r}$ is the same as in Fig. 7.13(a) namely $\mathrm{tr}\,(\boldsymbol{F})$ remains constant over the whole shear cell.

The deviatoric fraction decreases while increasing the mean density. Like the fabric a denser system yields a slightly more isotropic stress tensor than a dilute system. Figure 7.15 also indicates that the stress is more anisotropic in the inner part of the shear device and more isotropic in the outer part.

7.3.4 Conclusion

In the literature various approaches can be found on how the macroscopic stress tensor may be obtained from microscopic discrete variables. Ho-

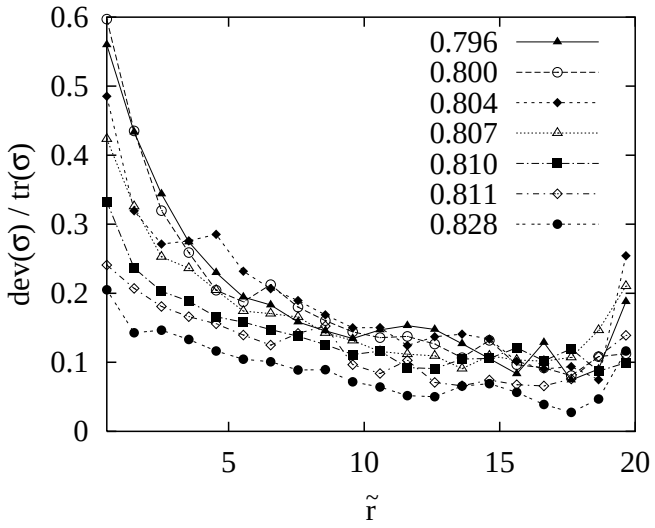

Fig. 7.15: *The deviatoric fraction* $\mathrm{dev}\,(\boldsymbol{\sigma})/\,\mathrm{tr}\,(\boldsymbol{\sigma})$ *of the stress versus the dimensionless distance from the inner ring for various global densities.*

wever, non of these approaches derives the complete dynamical stress tensor as done in this section. The above calculations were performed with the constrain of rigid disks in a two-dimensional, quasi-static system. The generalization for the more general case of three-dimensional, possibly non-spherical, objects with internal degrees of freedom like vibrational modes remains an open question. While the generalization to 3D spheres seems straightforward, the consequences of a non-spherical geometry and some non-rigidity might complicate the integrals too much to allow for a comparatively straightforward approach.

7.4 Total Elastic Deformation Gradient

Due to the duality of stress and strain, and the duality of contact forces and relative displacements, one would expect that the micro-mechanical definition of the strain tensor is easy to find. Unfortunately this is not the case.

In the literature mainly two ways for deriving an averaged strain in an assembly of grains exist: First the *equivalent continua* theories (BAGI [4]; SATAKE [84]) and second the *least square fit* theories (LIAO ET AL. [51]).

In this thesis a least-square-fit theory is considered. We, generally, follow the approach of LIAO ET AL. [51], but use $\vec{l}^{pc}$ instead of $\vec{l}^{pq}$.

To obtain a stress-strain relationship a kinematic hypothesis relating displacements and strains is used. The least-square-fit theory is based on the application of "VOIGT's hypothesis" assuming that the deformation is uniform and that every particle displacement conforms to the corresponding mean displacement field. Thus the movement of a particle p in an assembly of grains is in accordance with the mean displacement field. Under a given strain ε_{ij}[9] the mean field of particle displacement is given by

$$\vec{u}^{p} = \boldsymbol{\varepsilon} \cdot \vec{x}^{p} \; . \tag{7.81}$$

With $\vec{u}^{p}$ the displacement and $\vec{x}^{p}$ the position of the center of particle p.

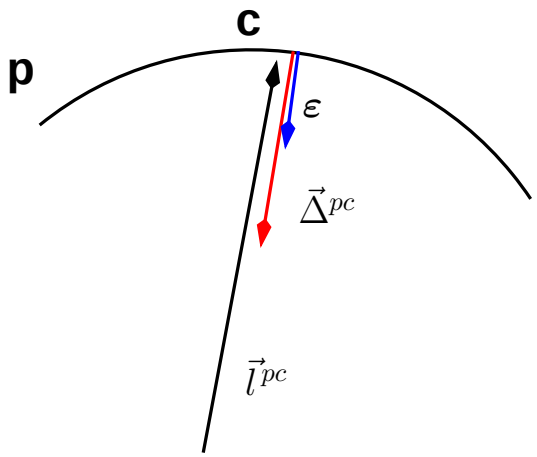

Fig. 7.16: *Definition of the quantities used for the description of the displacement.*

Now we consider two particles in contact at point c according to Fig. 7.16. The branch vector connecting the centroid of particle p with the contact point is denoted $\vec{l}^{pc}$. Then the expected displacement at contact c, relative to the force free situation, and due to the mean total elastic displacement gradient $\boldsymbol{\varepsilon}$, is

$$\vec{\Delta}^{pc} = \boldsymbol{\varepsilon} \cdot \vec{l}^{pc} \; . \tag{7.82}$$

With the simple and plausible assumption that particles are relatively rigid and discontinuities are allowed at inter-particle contacts, the relative displacement $\vec{\Delta}^{pc}$ represents the discontinuity at the inter-particle contact c.

[9] Note that the linear, symmetric strain $\boldsymbol{\epsilon} = \frac{1}{2}(\boldsymbol{\varepsilon} + \boldsymbol{\varepsilon}^{\mathrm{T}})$ is not identical to the displacement gradient, in general.

However, the VOIGT-hypothesis restricts the movement of the particles and thus corresponds to an upper-bound solution for the analysis. In our least-square-fit approach the VOIGT-hypothesis is extended by postulating that the actual displacement field does not coincide with the mean displacement field, but fluctuates about it. The difference between the actual (contact) displacement $\vec{\Delta}^{pc}$ and the expected displacement is

$$\vec{\chi}^{pc} = \boldsymbol{\varepsilon} \cdot \vec{l}^{pc} - \vec{\Delta}^{pc} \,. \tag{7.83}$$

The actual displacement is directly related to the simulations via $\vec{\Delta}^{pc} = \delta^c \vec{n}^c$ with δ^c the overlap between the two particles at contact c and $\vec{n}^c$ the normal vector from the center of the particle to the contact.

If one assumes that the mean displacement field best approximates the actual displacement, one can apply a "least square fit" to the total fluctuation, represented by the sum of square of $\vec{\chi}^{pc}$ for all individual contacts $\mathcal{C}$

$$S = \sum_{c=1}^{\mathcal{C}^p} (\vec{\chi}^{pc})^2 \;=\; \sum_{c=1}^{\mathcal{C}^p} (\boldsymbol{\varepsilon} \cdot \vec{l}^{pc} - \vec{\Delta}^{pc})^2 \,. \tag{7.84}$$

Thus minimizing S so that the partial derivatives with respect to the mean displacement gradient are zero, i.e. ,

$$\frac{\partial S}{\partial \boldsymbol{\varepsilon}} \stackrel{!}{=} \mathbf{0} \tag{7.85}$$

leads to

$$\frac{\partial S}{\partial \boldsymbol{\varepsilon}} = \sum_{c=1}^{\mathcal{C}^p} (\boldsymbol{\varepsilon} \cdot \vec{l}^{pc} - \vec{\Delta}^{pc}) \cdot \frac{\partial}{\partial \boldsymbol{\varepsilon}} (\boldsymbol{\varepsilon} \cdot \vec{l}^{pc} - \vec{\Delta}^{pc}) \,. \tag{7.86}$$

These four equations for the four components of $\boldsymbol{\varepsilon}$ in 2D can be transformed into a relation for the mean displacement tensor as a function of the contact displacements and the branch vectors, by assuming that $\partial \vec{\Delta}^{pc} / \partial \boldsymbol{\varepsilon} = \vec{0}$,

$$\boldsymbol{\varepsilon} = \frac{1}{a^2} \sum_{c=1}^{\mathcal{C}^p} \vec{\Delta}^{pc} \vec{l}^{pc} \cdot \boldsymbol{A} \,. \tag{7.87}$$

The tensor $\boldsymbol{A}$ denotes the inverse of the fabric tensor $\boldsymbol{F} = \sum_{c=1}^{\mathcal{C}^p} \vec{n}^c \vec{n}^c$ as defined in Sect. 7.2.

By applying the averaging formalism of Chapter 5 on the above derivation of Eq. 7.87 the equations look as follows:

$$S = \frac{1}{V} \sum_{p \in V} w_V^p V^p \sum_{c=1}^{\mathcal{C}^p} (\vec{\chi}^{pc})^2 \,, \tag{7.88}$$

$$\frac{2}{V}\sum_{p\in V} w_V^p V^p \sum_{c=1}^{\mathcal{C}^p}(\boldsymbol{\varepsilon}\cdot\vec{l}^{pc}-\vec{\Delta}^{pc})\cdot\frac{\partial}{\partial\boldsymbol{\varepsilon}}(\boldsymbol{\varepsilon}\cdot\vec{l}^{pc}-\vec{\Delta}^{pc})=\mathbf{0}\,, \tag{7.89}$$

$$\bar{\boldsymbol{\varepsilon}}=\frac{2\pi h}{V}\left(\sum_{p\in V} w_V^p \sum_{c=1}^{\mathcal{C}^p}\vec{\Delta}^{pc}\vec{l}^{pc}\right)\cdot\boldsymbol{A}\,. \tag{7.90}$$

This relates the actual deformations to a "virtual stress-free" reference state where all contacts start to form, i.e. particles are just touching with $\delta = 0$. The result is a non-symmetric tensor $\boldsymbol{\varepsilon}$, which is *not* the strain, instead we refer to it as the total elastic deformation gradient.

In principle one should distinguish between three different formulations: First, our "total elastic deformation gradient" $\boldsymbol{\varepsilon} = f(\vec{\Delta})$ which is total in the sense that $\vec{\Delta}$ is relative to the stress free state. Second, the deformation rate tensor $\dot{\boldsymbol{\varepsilon}} = f(\dot{\vec{\Delta}})$ and third, the differential deformation gradient $\delta\boldsymbol{\varepsilon} = f(\delta\vec{\Delta})$. Because of our chosen force laws, we assume linearity in the sense that $\int \delta\vec{\Delta} = \vec{\Delta}$. Therefore, we are allowed to use our total elastic deformation gradient in the same way as the traditional strain (see also Sect. 7.5).

7.4.1 Behavior of the Total Elastic Deformation Gradient

We investigated the strain by looking at the eigenvalues of the strain tensor. In Fig. 7.17 the volumetric part of the elastic deformation gradient is localized in the shear zone where it is largest. This effect is stronger for lower global density. It is easier to compress the dilute material closer to the inner ring due to dilation, as compared to the denser material in the outer part. For higher global densities the density in the shear zone does not change that strong as compared with the outer parts, therefore also the volumetric strain becomes nearly constant.

The deviatoric fraction of $\boldsymbol{\varepsilon}$, as shown in Fig. 7.18, behaves in a similar way. It is decaying with increasing distance from the center, similar to the deviatoric fractions of fabric and stress. From the figure it is also evident, that the strain, like the fabric and stress, becomes more isotropic with increasing mean density. However, $\mathrm{dev}\,(\boldsymbol{\varepsilon})/\,\mathrm{tr}\,(\boldsymbol{\varepsilon})$ is *not* much dependent $\bar{\nu}$ in contrast to $\mathrm{dev}\,(\boldsymbol{F})/\,\mathrm{tr}\,(\boldsymbol{F})$.

In Fig. 7.19 we show the orientation of the deformation gradient with respect to the radial outwards direction. The orientation of the major eigenvectors is almost constant for different simulations up to a value of about

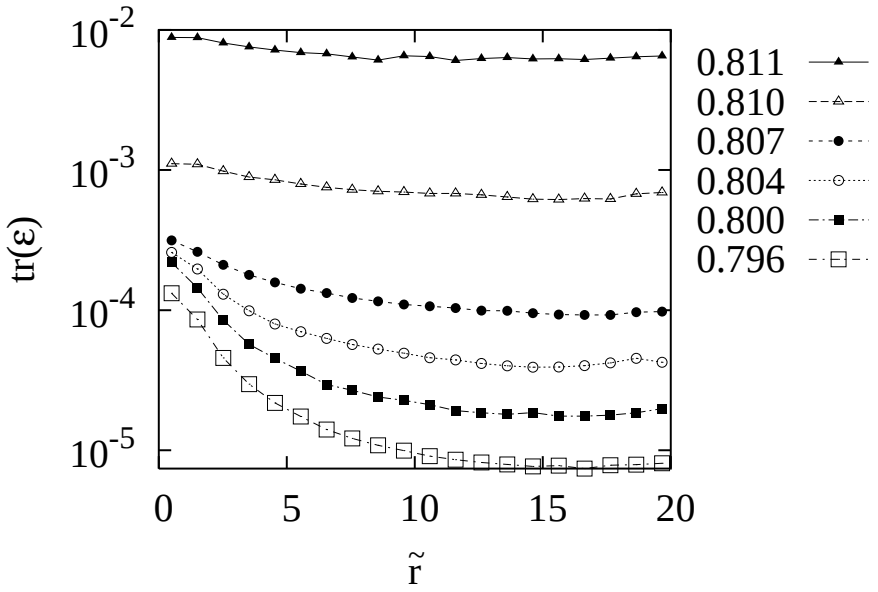

Fig. 7.17: *The trace of the strain tensor* $\mathrm{tr}\ \boldsymbol{\varepsilon}$ *plotted against the dimensionless distance from the inner wheel for different global densities.*

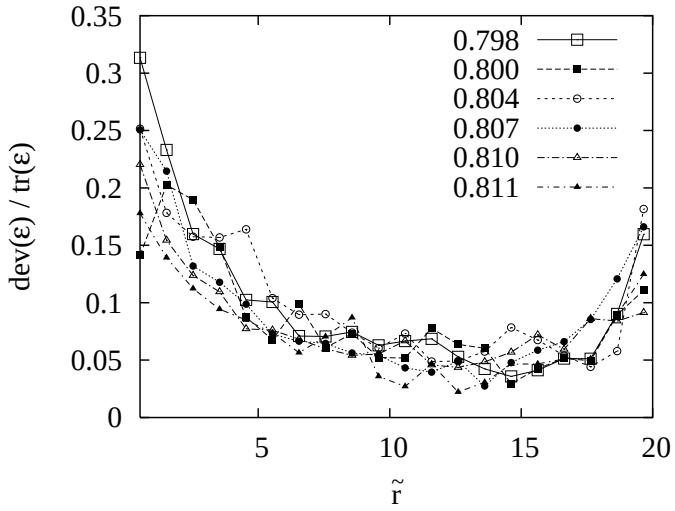

Fig. 7.18: *The deviatoric fraction of the strain is plotted versus the dimensionless distance from the inner wheel for different global densities.*

10 layers of particles counted from the inner ring. In the region between 10 and 17 layers of particles the peaks in ϕ_ε are correlated to very small $\mathrm{dev}\,(\boldsymbol{\varepsilon})/\,\mathrm{tr}\,(\boldsymbol{\varepsilon})$ where the orientation is not well defined. In the outermost part ϕ_ε decreases as $\mathrm{dev}\,(\boldsymbol{\varepsilon})/\,\mathrm{tr}\,(\boldsymbol{\varepsilon})$ increases clearly.

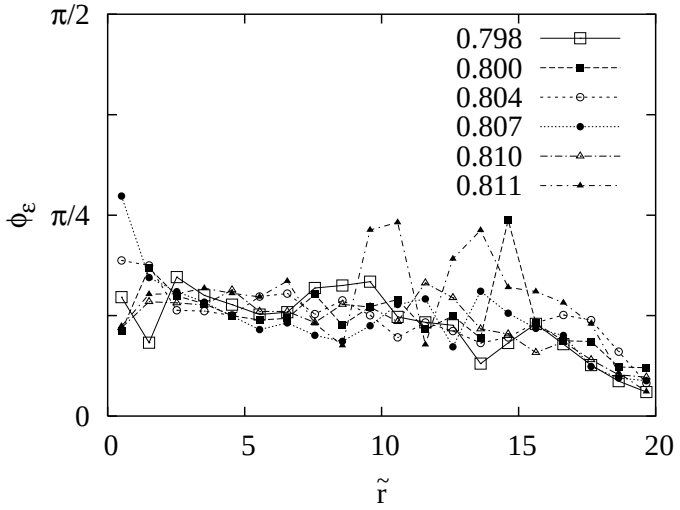

Fig. 7.19: *The figure shows the orientation of the major eigenvector of the strain tensor with respect to the radial outwards direction.*

7.4.2 Conclusion

The derivation of a strain tensor is not that straightforward as for the stress tensor. In our work we followed the least square fit approach of LIAO ET AL. and calculated the total elastic deformation gradient. By limiting ourselves to only describe the elastic behavior of a granulate and because of the used linear force laws we are allowed to relate the total elastic deformation gradient to the actual strain tensor. By observation of the volumetric part of the gradient we demonstrated that it is easier to compress the material in the more dilute inner part of the shear cell than in the outer part. For the deviatoric fraction of the strain a behavior similar to that of the fabric tensor was found, yet $\mathrm{dev}\,(\boldsymbol{\varepsilon})/\,\mathrm{tr}\,(\boldsymbol{\varepsilon})$ does not depend that strongly on the volume fraction ν than the fabric.

Despite the nice results for the total elastic deformation gradient the question of how to compute also plastic strain remains an open question. A formulation incorporating plastic deformations has to take care of the opening and closing of contacts during the time of observation. An other approach might be the commutation of the strain rate from two consecutive snapshots of the simulation. However, we were interested in a definition of the strain which is capable to compute the strain from one snapshot of the system. A task which is fulfilled by our definition.

7.5 Material Properties

In order to use a continuum model to describe a granular material, one needs to know the coefficients of the constitutive model used. The constitutive model relates the stress to the strain tensor in the simplest linear elastic approach. The situation is shown in Fig. 7.20 for the linear and the non-linear case. The plots show the relationship between stress and strain, starting from the virtual stress free reference frame. In the linear case (left panel (a)) the ascending slope of σ shows the proportionality between stress and strain, thus the differential and the total formulation of the relationship are equivalent. In the non-linear case shown in the right panel of Fig. 7.20, the stress is not proportional to the strain everywhere. Therefore, the relationship is locally defined by $\partial\sigma/\partial\varepsilon$ instead. However, we restrict ourself to the linear approach.

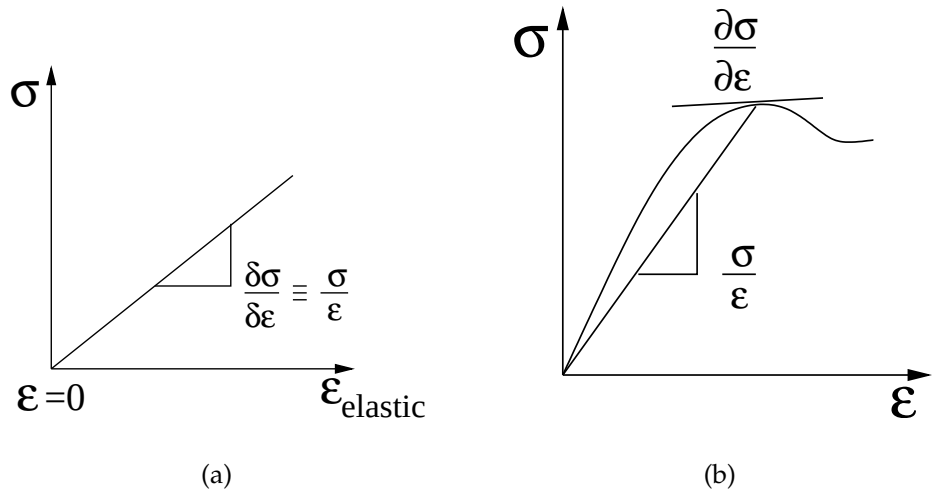

Fig. 7.20: *Schematic plot of the stress-strain relation in a* **(a)** *linear and a* **(b)** *non-linear case. For the linear case the differential and the total formulation are equivalent, whereas in the non-linear case they are different.*

In a simple isotropic theory the stress and the strain tensor are assumed to be co-linear, which means they share the same orientation.

In Fig. 7.21 the orientations of the fabric, stress and deformation gradient tensor are plotted against the distance from the inner wheel. In the outer

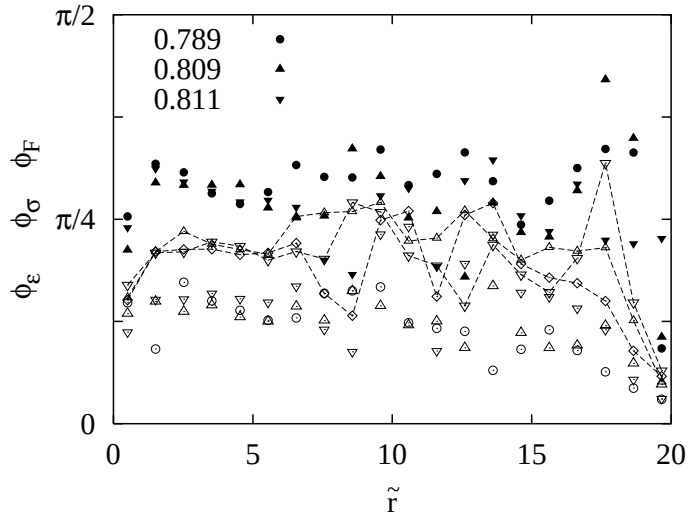

Fig. 7.21: *Orientation of the tensors $\boldsymbol{F}$, $\boldsymbol{\sigma}$, and $\boldsymbol{\varepsilon}$, plotted against the distance from the inner ring for three different simulations. Solid symbols are fabric, solid symbols connected by lines are stress, and open symbols are elastic deformation gradient data.*

part, the deviatoric fraction is usually around 10 per-cent, i.e. so small that the orientations become too noisy to allow for a proper definition. We find that all orientation angles ϕ show the same qualitative behavior, however, the fabric is tilted more than the stress which, in turn, is tilted more than the deformation gradient. Thus, the three tensorial quantities examined are *not* co-linear. Still, in the following we will examine the bulk stiffness as well as the shear stiffness of a classical isotropic material model, keeping in mind that the anisotropy is neglected here.

We first compute mean field expectation values for $\boldsymbol{\sigma}$ and $\boldsymbol{\epsilon}$ to get a rough estimate for the orders of magnitude of the material constants E, the material stiffness, and G, the granular shear resistance.

With the proposed averaging procedure the stress tensor was computed via

$$\boldsymbol{\sigma} = \frac{1}{V} \sum_{p \in V} w_V^p \sum_{c=1}^{\mathcal{C}^p} \vec{f}^{\,c} \otimes \vec{l}^{\,pc} \,. \tag{7.91}$$

Replacing $\vec{f}^{\,c}$ by its mean $\bar{\vec{f}} = k^n \bar{\delta} \vec{n}^{\,c}$ and $\vec{l}^{\,pc}$ by the mean branch vector $\bar{a}\vec{n}^{\,c}$ one gets

$$\bar{\boldsymbol{\sigma}} = (k^n \bar{\delta} / h\pi a)\, \boldsymbol{F} \,. \tag{7.92}$$

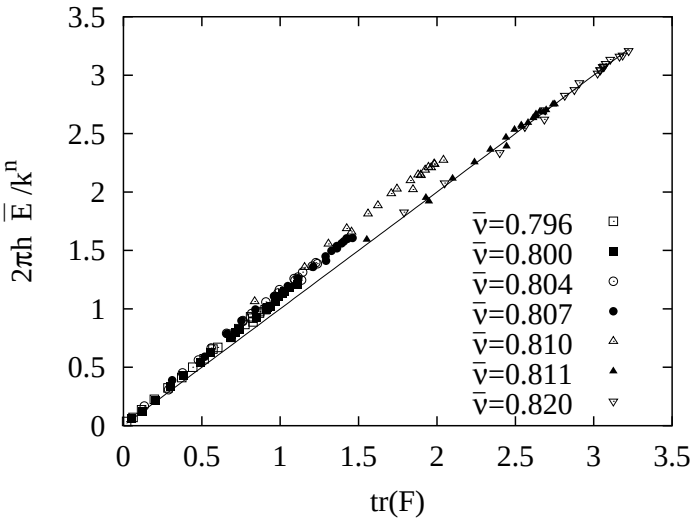

Fig. 7.22: *Granular stiffness* $2\pi h\bar{E}/k^n = \mathrm{tr}\,(\boldsymbol{\sigma})/\,\mathrm{tr}\,(\boldsymbol{\varepsilon})$*, plotted against* $\mathrm{tr}\,(\boldsymbol{F})$ *for different simulations. Every point corresponds to one ring of 150, i.e.* $\Delta r \approx (1/8)\tilde{d}$*.*

For the strain

$$\boldsymbol{\epsilon} = \frac{2\pi h}{V}\left(\sum_{p\in V} w_V^p \sum_{c=1}^{\mathcal{C}^p} \vec{\Delta}^{pc} \otimes \vec{l}^{pc}\right) \cdot \boldsymbol{A}\ . \tag{7.93}$$

similar replacements lead to

$$\bar{\boldsymbol{\epsilon}} = (\bar{\delta}/a)\,\boldsymbol{I}\ , \tag{7.94}$$

equivalent to

$$\bar{\boldsymbol{\epsilon}} = (2\pi h/k^n)\,\bar{\boldsymbol{\sigma}} \cdot \boldsymbol{A}\ . \tag{7.95}$$

The material stiffness, $\bar{E}$, can be defined as the ratio of the volumetric parts of stress and strain, so that one obtains from Eq. 7.92 and 7.94

$$\bar{E} = (k^n/2\pi h)\ \mathrm{tr}\,(\boldsymbol{F})\ . \tag{7.96}$$

In Fig. 7.22 the rescaled stiffness of the granulate is plotted against the trace of the fabric for some simulations. Note that all data collapse almost on a line, but the mean-field value (solid line) underestimates the simulation data by a few per-cent. Simulation data for different k^n and even data from simulations with neither bottom- nor tangential friction collapse with the data for fixed k^n and different volume fractions, shown here. The deviations from the identity curve are closely related to shear, as the two highly blocked simulations with $\bar{\nu} = 0.811$ and $\bar{\nu} = 0.820$ are fitted nicely by the line.

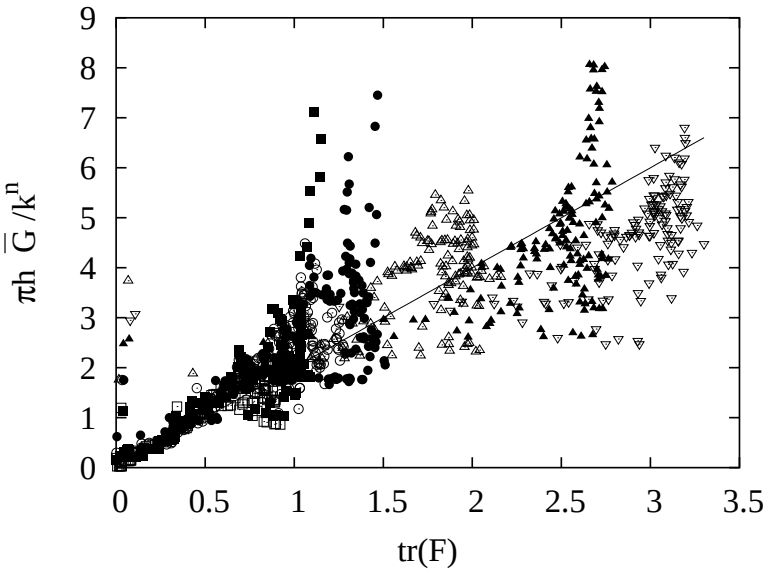

Fig. 7.23: *Scaled granulate shear resistance* $\pi h\bar{G}/k^n = \mathrm{dev}\,(\boldsymbol{\sigma})/\,\mathrm{dev}\,(\boldsymbol{\epsilon})$ *plotted against* $\mathrm{tr}\,(\boldsymbol{F})$ *for various simulations. The symbols refer to the same simulations as in Fig. 7.22.*

In Fig. 7.23 the ratio of the deviatoric parts of stress and strain is plotted against the trace of the fabric. We did not use the traditional definition of the shear modulus (KRUYT AND ROTHENBURG [47]), since our tensors are not co-linear as shown in Fig. 7.21. Like the material stiffness, both quantities are proportional, for points near or within the shear band. In the outer part of the shear-cell the particles are strongly inter-locked and thus resist much more against shear, and therefore $\bar{G}$ diverges. For increasing global density, the critical contact number density also grows, at a critical density.

7.6 Constitutive Law

With the derived material constants we are able to formulate a constitutive law for sheared $2D$ granular media which takes also into account the micro-structure of the assembly. As a starting point it is convenient to decompose the stress tensor as

$$2\boldsymbol{\sigma} = \mathrm{tr}\,(\boldsymbol{\sigma})\boldsymbol{I} + \widetilde{\phi_\sigma}\,\mathrm{dev}\,(\boldsymbol{\sigma}) \tag{7.97}$$

into an isotropic and a deviatoric (trace-free) part with

$$\widetilde{\boldsymbol{\phi}_\sigma} = \boldsymbol{R} \begin{pmatrix} 1 & 0 \\ 0 & -1 \end{pmatrix} \boldsymbol{R}^{-1} \tag{7.98}$$

being the deviatoric unit tensor rotated by an angle ϕ_σ and $\boldsymbol{R} = \boldsymbol{R}(\phi_\sigma)$. This equation could be rewritten with $p = \frac{1}{2}\operatorname{tr}(\boldsymbol{\sigma})$ as follows

$$\boldsymbol{\sigma} = p\boldsymbol{I} + \widetilde{\boldsymbol{\phi}_\sigma}(\operatorname{dev}(\boldsymbol{\sigma})/2) , \tag{7.99}$$

$$= p\left[\boldsymbol{I} + \widetilde{\boldsymbol{\phi}}_\sigma(\operatorname{dev}(\boldsymbol{\sigma})/\operatorname{tr}(\boldsymbol{\sigma}))\right] , \tag{7.100}$$

$$= p\left[\boldsymbol{I} + \widetilde{\boldsymbol{\phi}}_\sigma(q)\right] , \tag{7.101}$$

with the deviatoric fraction q. In order to formulate a constitutive law we request $\boldsymbol{\sigma}$ to be a function of the deformations in terms of $\boldsymbol{\varepsilon}$ and the local structure as expressed by $\boldsymbol{F}$

$$\boldsymbol{\sigma} \stackrel{!}{=} f(\boldsymbol{\varepsilon}, \boldsymbol{F}) . \tag{7.102}$$

By introducing the material laws found in the previous section for the isotropic modulus

$$\bar{E} \equiv \frac{\operatorname{tr}(\boldsymbol{\sigma})}{\operatorname{tr}(\boldsymbol{\varepsilon})} = \frac{k^n}{2\pi h}\operatorname{tr}(\boldsymbol{F}) , \tag{7.103}$$

and the non-dimensional shear modulus

$$G^* = \frac{\bar{G}}{\bar{E}} \equiv \frac{\operatorname{dev}(\boldsymbol{\sigma})\operatorname{tr}(\boldsymbol{\varepsilon})}{\operatorname{dev}(\boldsymbol{\varepsilon})\operatorname{tr}(\boldsymbol{\sigma})} = \begin{cases} \frac{k^n}{\pi h}\operatorname{tr}(\boldsymbol{F}) & \leq \operatorname{tr}(\boldsymbol{F})^{\text{div}} \\ \infty & > \operatorname{tr}(\boldsymbol{F})^{\text{div}} \end{cases} \tag{7.104}$$

we obtain

$$\boldsymbol{\sigma} = \varepsilon_0 \bar{E}\left[\boldsymbol{I} + G^* \widetilde{\boldsymbol{\phi}}_{\varepsilon,F}(\varepsilon_1)\right] \tag{7.105}$$

as final constitutive law. Herein the constants are the isotropic strain

$$\varepsilon_0 = \operatorname{tr}(\boldsymbol{\varepsilon})/2 , \tag{7.106}$$

and the deviatoric strain fraction

$$\varepsilon_1 = \operatorname{dev}(\boldsymbol{\varepsilon})/\operatorname{tr}(\boldsymbol{\varepsilon}) . \tag{7.107}$$

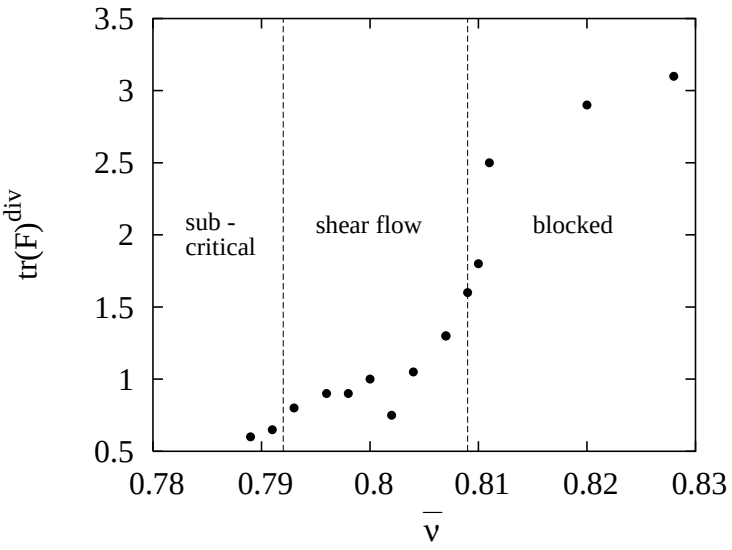

Fig. 7.24: *The plot shows* $\mathrm{tr}\,(\boldsymbol{F})^{\mathrm{div}}$

From Fig. 7.21 we "guess"

$$\widetilde{\phi_\sigma} = \widetilde{\phi}_{\varepsilon,F} \cong (\phi_\varepsilon + \phi_F)/2\,. \tag{7.108}$$

The value of $\mathrm{tr}\,(\boldsymbol{F})^{\mathrm{div}}$ at which the shear modulus $\bar{G}$ starts to diverge as shown in Fig. 7.23 is plotted in Fig. 7.24 against the global packing fraction $\bar{\nu}$. The different regimes separated by the dotted lines are the same as in Fig. 6.5. The functional behavior of $\mathrm{tr}\,(\boldsymbol{F})^{\mathrm{div}}$ is still an open question and should be subject to further investigations.

Thus due to Eq. 7.102 we finally find

$$\boldsymbol{\sigma} = \varepsilon_0 \frac{k^n}{2\pi h}\,\mathrm{tr}\,(\boldsymbol{F})\left[\boldsymbol{I} + G^*\widetilde{\boldsymbol{\phi}}_{\varepsilon,F}(\varepsilon_1)\right]\,. \tag{7.109}$$

This linear isotropic constitutive law relates the stress tensor with the strain tensor, but also accounts for the internal structure of the granulate by including the trace of the fabric and therefore the mean number of contacts of the granular ensemble. With the shear modulus $\bar{G}$ the divergence of the fabric tensor enters the equations. This term is coupled with the local and the global density of the system.[10] However, a closer examination of this relationship would be of value.

[10] This can easily seen for the limit $\varepsilon_1 = 0$ meaning isotropic compression where we obtain $p = \frac{k^n}{2\pi}\mathcal{C}\nu\varepsilon_0$ and in the case of pure deviatoric shear $\varepsilon_0 = 0$ where $q = G^*(\mathcal{C}\nu)\varepsilon_1$ is evidenced.

7.7 Conclusion

The final goal of the mechanics of granular media is to gain knowledge of the behavior of granular materials under external loads or under externally applied deformations. This goal is often tackled via continuum mechanics relating external loads on the material to the resulting displacements by constitutive relations or vice versa.

In this section after a brief introduction on classical continuum theory we used our proposed averaging formalism to compute different tensorial quantities. Continuum theories homogenize the heterogeneous and discrete nature of granular material. However, we are interested also in the structural properties of the assembly and therefore investigated the fabric tensor as one possible measure for the degree of anisotropy of the assembly. The probability distribution to find a contact in a given direction of a particle shows that near the inner wall there are more contacts in tangential direction due to ordering influenced by the wall layering. Additionally there exists an overpopulation of particle contacts in the direction of $\phi = 60^o$ measured in the shearing direction because the grains resist against the shear or, with other words, contacts are opened due to shear in the opposite direction $-\phi$ were an underpopulation is found. Farther away from the shearing wall, the distribution became more homogeneous. At the outer part it became again inhomogeneous, this time due to crystallization effects during the initial compression phase where the grains formed a triangular lattice. The dynamics in this outer part is slow, therefore this structures survive over long times.

To compute the macroscopic variables stress and strain, we derived those quantities from the microscopic variables: forces, contact vectors and contact displacements. For the stress tensor we also took care of the components related to the dynamics of the granulate. However, these components were by orders of magnitude smaller than the stresses due to the forces. Therefore, the dynamical part was neglected in the rest of this section as well as components related with the rotations of the grains. These components only appear in the innermost part of the device and are strongly correlated with the shear zone, thus they might be of interest for further studies.

We predicted the behavior of the stress tensor by continuum theoretical con-

siderations. These predictions, the diagonal elements of the stress tensor are constant, whereas the off-diagonal elements related to the shear stress decay proportionally to $1/r^2$ when increasing the distance to the inner wall are in agreement with the simulations. They also explain why the shear band is always found at the inner wall where the shear stress is largest.

The definition of the strain tensor is a controversial topic of current research. In this section we derived the total elastic deformation gradient based on a least square fit approach. Because we use a linear force law and limit ourself to the description of the elastic behavior of the granulate, we are allowed to relate this tensor to the actual strain. With the stress and the strain at hand we computed the granular stiffness E and the shear stiffness G in the framework of an isotropic elastic material law of Hooke type. Even if the assumption of an isotropic material is wrong in large parts of the material we were able to collapse the computed stiffness for various packing fractions on one curve when plotted against the trace of the fabric tensor. This result is in agreement with mean field considerations. The shear modulus of different simulations also collapsed on one curve when plotted against the trace of the fabric for points near or within the shear band. In the outer part of the shear-cell the particles are strongly inter-locked and thus resist much more against shear, so that G diverges. For increasing global density, the critical contact number density also grows. By using this dependence of the material constants on the local structure (given in terms of the fabric tensor) we formulated a constitutive law relating the stress tensor with the deformations and the micro structure of the granulate.

8 Rotational Degrees of Freedom

The classical continuum theory introduced in Section 7.1 and used in the previous chapter, is, according to its name, the currently accepted theory of continua. Nevertheless, other descriptions exist to incorporate phenomena, like rotations, not captured by the classical theory.

Granular media are characterized by the discrete nature of their grains. These grains possess the a priori independent degrees of freedom, rotation and translation. However, in a continuum approximation of the behavior of granular media, usually the degree of freedom of rotation is suppressed or neglected, as already at relatively low stresses, the grains behave more or less as rigid bodies. The assumption of a continuum whose material points displace only (BOLTZMANN continuum) leads usually to a rather good approximation of the behavior of a granular assembly, and is almost always adopted in soil mechanics. This approach was used in Chapter 7.

However, looking for example at shearing experiments, there is a class of deformation patterns, termed localization modes, where the grain rotations as additional degrees of freedom in the continuum description are paramount (ASTRØM ET AL. [2]). In our setup we also find this kind of localizations in the shear zone at the inner wheel, as already reported in Sect. 6 while comparing the simulations to the physical system.

Because of the evident importance of the rotational degree of freedom, we

use the theoretical framework of a COSSERAT continuum (COSSERAT AND COSSERAT [19]; ERINGEN [29]; ZERVOS ET AL. [110]) to extend our continuum description. In addition to the stress and the displacement gradient a couple stress $\boldsymbol{M}$ and a curvature $\boldsymbol{\kappa}$ have to be defined.

In the following section we will briefly introduce the concept of the Cosserat continuum. Thereafter, we will use our averaging formalism to compute the quantities used within the Cosserat theory. We further calculate the macroscopic quantities the couple stress and the curvature and calculate a new material property, the *torque resistance*.

8.1 Cosserat Theory

Continuum theories including non-standard degrees of freedom, are called generalized continuum theories. In the case of independent rotational degrees of freedom one speaks of a COSSERAT continuum. This type was first described by the COSSERAT brothers (COSSERAT AND COSSERAT [19]) and later rediscovered by GÜNTHER [37] and SCHAEFER [85]. For a more fundamental derivation see also the book of ERINGEN AND KAFADAR [30]. The extensions of the kinematics and the balance laws, as shown in the following, can be found in detail for example in (BESDO [9]; DE BORST [25]; EHLERS AND VOLK [28]; MÜHLHAUS ET AL. [72]; STEINMANN [89]; VOLK [105])

In continuum mechanical terms the "Cosserat continuum" is a continuum of material points, where each of them is provided with an additional space-direction.[1] So the Cosserat theory of elasticity, additionally to the translation assumed in the classical theory, incorporates a local rotation of the points. Analogous to stress and deformation gradient in the classical theory a couple stress (torque per unit area) and a curvature (gradient of the "rotation" variable) are introduced.

In the following again only a linear theory will be used, but the Cosserat theory in general is not restricted to that.

[1] Because of this orientation, such medias are often referred to as micropolar.

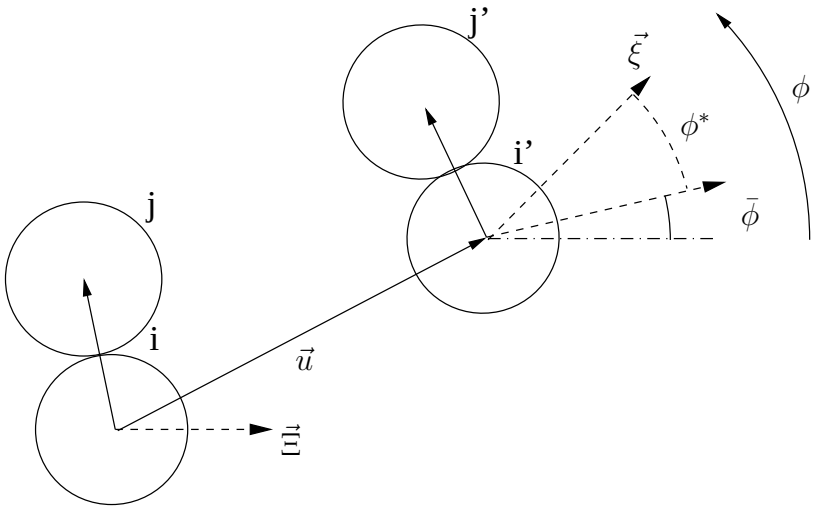

Fig. 8.1: *Definition of the quantities used for the Cosserat approach. $\vec{\Xi}$ and $\vec{\xi}$ are the so called directors in the reference and the actual configuration, respectively. The rotation of the joint from particle i to j depends on the movement of the system and therefore equals the continuum rotation $\bar{\phi}$. Additionally the particles might rotate freely and thus add an independent rotation ϕ^* to the total rotation ϕ.*

Kinematics

Because of the rotations as an additional degree of freedom every material point in a COSSERAT continuum yields not only a displacement vector $\vec{u}$ but also a rotation vector ϕ. In the linear formulation of the theory, considered here displacements as well as rotations are infinitesimal. The infinitesimal rotation leads to a rotation vector ϕ which can be decomposed, according to Fig. 8.1, into a continuum rotation $\bar{\phi}$ and an independent rotation ϕ^*

$$\phi = \bar{\phi} + \phi^* \,. \tag{8.1}$$

The continuum rotation is related with the displacements via

$$\bar{\phi} = -\frac{1}{2}\mathrm{rot}\,\vec{u}\,. \tag{8.2}$$

The deformation tensor is now non-symmetric in general

$$\epsilon_{\alpha\beta} = \partial_\alpha u_\beta + e_{\alpha\beta\gamma}\phi_\gamma \,, \tag{8.3}$$

where $e_{\alpha\beta\gamma}$ is the permutation tensor. The symmetric part of ϵ

$$\epsilon_{(\alpha\beta)} = \frac{1}{2}(u_{\beta,\alpha} + u_{\alpha,\beta}) = \epsilon_{\text{classical}} \tag{8.4}$$

equals the classical deformation tensor. The skew symmetric part

$$\epsilon_{[\alpha\beta]} = \frac{1}{2}(u_{\beta,\alpha} - u_{\alpha,\beta}) + e_{\alpha\beta\gamma}\phi_\gamma = e_{\alpha\beta\gamma}\phi^*_\gamma \tag{8.5}$$

is directly related with the independent rotations of the material points. Therefore, for vanishing independent rotations the classical theory is restored.

In the micropolar theory an additional quantity the also non-symmetric curvature is introduced

$$\kappa_{\alpha\beta} = \partial_\alpha \phi_\beta \; . \tag{8.6}$$

Balance Equations

In the following a brief outline of the balance equations of the Cosserat continuum is given. The mass balance equation

$$\frac{\partial \rho}{\partial t} + \mathrm{div}\,(\rho \vec{v}) = 0 \tag{8.7}$$

and the momentum balance equation

$$\rho \frac{D}{Dt}\vec{v} \;=\; \rho\vec{k} + \mathrm{div}\;\boldsymbol{\sigma} \tag{8.8}$$

of the standard continuum (cf . Eq. 7.19) and the Cosserat continuum are identical.

As a result of the angular momentum balance in the classical theory Eq. 7.28

$$\int_{\mathcal{B}} \vec{s^*} dV = \vec{0} \tag{8.9}$$

and due to the fact, that this equation should hold under all values of $\mathcal{B}$ the stress tensor had to be symmetric $\vec{s^*} = \vec{0}$.

In the Cosserat theory every material point has not only translational degrees of freedom but an additional orientation. So the angular momentum balance has to be extended by a volume moment $\vec{m}$ and a surface moment $\vec{\mu}$.[2] On the left hand side of the balance equation 7.25 the spin $\mathcal{I}\vec{\omega}$ of every material point has to be added which finally leads to

$$\frac{D}{Dt}\int_{\mathcal{B}} \rho(\vec{x} \times \vec{v} + \mathcal{I}\vec{\omega}) dV = \int_{\mathcal{B}} (\vec{x} \times \rho\vec{k} + \vec{m}) dV + \int_{\partial\mathcal{B}} (\vec{x} \times \vec{s} + \vec{\mu}) dA \; . \tag{8.10}$$

[2] As an example for a volume moment one may think of a magnetic material in an external magnetic field.

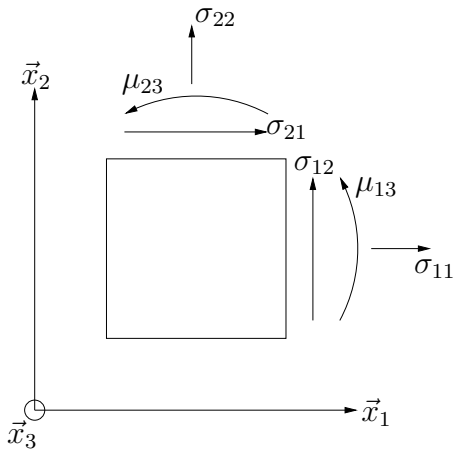

Fig. 8.2: *Components of a two-dimensional Cosserat element. The arrows indicate our convention for positive values.*

Analogous to the CAUCHY definition 7.20 of the stress tensor $\boldsymbol{\sigma} \cdot \vec{n} = \vec{s}$ the couple stress tensor $\boldsymbol{M}$ with $\vec{\mu} = \boldsymbol{M} \cdot \vec{n}$ is introduced. Applying GAUSS theorem Eq. 8.10 reads

$$\int_{\mathcal{B}} \rho \left(\vec{x} \times \frac{D\vec{v}}{Dt} + \frac{D\mathcal{I}\vec{\omega}}{Dt} \right) dV = \int_{\mathcal{B}} \left[\vec{x} \times (\operatorname{div} \boldsymbol{\sigma} + \rho\vec{k}) + \vec{s^*} + \vec{m} + \operatorname{div} \boldsymbol{M} \right] dV \ . \tag{8.11}$$

Due to the momentum balance (Eq. 8.8) and by taking into account that the integral should not depend on the value of $\mathcal{B}$

$$\rho \frac{D\mathcal{I}\vec{\omega}}{Dt} = \vec{s^*} + \vec{m} + \operatorname{div} \boldsymbol{M} \tag{8.12}$$

is obtained. In this equation the symmetry of the stress tensor can no longer be deduced. Though symmetry could be retained if $\boldsymbol{M}$, $\vec{\mu}$ and $\mathcal{I}\vec{\omega}$ were to form an equilibrated system by themselves. Thus the non-symmetry might not be of importance in applications where the exchange of momentum between translational and rotational degrees of freedom is weak.

Constitutive Equations

With the relations of the two previous sections only the constitutive equations are missing in order to have a closed set of equations for a micropolar continuum theory. From the deformation and the curvature tensors

we claim the existence of an elastic potential

$$\Phi = \Phi(\boldsymbol{\epsilon}, \boldsymbol{\kappa}) \tag{8.13}$$

and define the stresses as

$$\sigma_{\alpha\beta} = \frac{\partial \Phi}{\partial \epsilon_{\alpha\beta}}, \qquad \text{and} \qquad M_{\alpha\beta} = \frac{\partial \Phi}{\partial \kappa_{\alpha\beta}} \, . \tag{8.14}$$

From a theoretical point of view the stress $\boldsymbol{\sigma}$ in principle could also depend on $\boldsymbol{\kappa}$ but this is excluded by our constitutive relation. Likewise, $\boldsymbol{M}$ is assumed to be independent of $\boldsymbol{\epsilon}$.

In a linear theory the potential energy Φ is a homogeneous function of second order of $\epsilon_{\alpha\beta}$ and $\kappa_{\alpha\beta}$ so

$$\Phi = \frac{1}{2}\left(\frac{\partial \Phi}{\partial \epsilon_{\alpha\beta}} \epsilon_{\alpha\beta} + \frac{\partial \Phi}{\partial \kappa_{\alpha\beta}} \kappa_{\alpha\beta} \right) = \frac{1}{2}(\sigma_{\alpha\beta}\epsilon_{\alpha\beta} + M_{\alpha\beta}\kappa_{\alpha\beta}) \, . \tag{8.15}$$

Besides the geometrical linear theory in the following linearity also applies for the material law used. For an isotropic material we therefore use a modified HOOKEs law like the one of Eq. 7.32. A detailed derivation of the material law can be found in (DE BORST [25]; VOLK [105]).

$$\begin{aligned} \boldsymbol{\sigma} &= 2\mu \boldsymbol{\epsilon}_{\text{sym}} + \lambda(\text{tr}\boldsymbol{\epsilon})\boldsymbol{I} + 2\mu_c \boldsymbol{\epsilon}_{\text{skew}} \\ \boldsymbol{M} &= 2\mu^* \boldsymbol{\kappa}_{\text{sym}} + \lambda^*(\text{tr}\boldsymbol{\kappa})\boldsymbol{I} + 2\mu_c^* \boldsymbol{\kappa}_{\text{skew}} \end{aligned} \tag{8.16}$$

As a result of the Cosserat considerations instead of the two Lamé constants μ and λ in the classical theory there are six Cosserat parameters in general ($\mu, \lambda, \mu_c, \mu^*, \lambda^*$ and μ_c^*). According to de Borst (DE BORST [25]) one can simplify the coupling between $\boldsymbol{M}$ and $\boldsymbol{\kappa}$ by assuming direct proportionality

$$\boldsymbol{M} = 2\mu_c(\ell^2)\boldsymbol{\kappa} \, . \tag{8.17}$$

Unlike in classical continuum theory with Eq. 8.17 a length scale ℓ enters the set of equations. There is a lot of controversy on how this length is related to the material specific properties like e.g. the grain diameter (MÜHLHAUS AND VARDOULAKIS [73]; VOLK [105]).

8.2 Rotational Degree of Freedom in the Simulation

In Sect. 6 we showed the oscillating behavior of the spin of the particles in a localized shear zone near the inner wall of the shearing device. The spin density of the particles was defined as:

$$\nu\omega = \frac{1}{V}\sum_{p\in V} w_V^p V^p \omega^p \,. \tag{8.18}$$

The spin considered so far describes the total rotation ϕ of the particles. Following Eq. 8.1 of the previous section the total rotation can be decomposed in two parts, a rotation due to the movement of the material as whole in the given geometry and an excess rotation of the single particles. The first one, the continuum rotation $\bar{\phi}$, is obtained from the displacement gradient according to Eq. 8.2. The associated angular velocity is therefore calculated from the deformation rate tensor $\vec{\nabla}\vec{v}$.

In our geometry, the deformation rate $\vec{\nabla}\vec{v}$ has only two entries, namely

$$[\vec{\nabla}\vec{v}]_{r\phi} = \frac{\partial v_\phi}{\partial r} \quad \text{and} \quad [\vec{\nabla}\vec{v}]_{\phi r} = -\frac{v_\phi}{r}\,, \tag{8.19}$$

from which one can derive the continuum rotation velocity $\bar{\omega}$:

$$\bar{\omega} = \frac{1}{2}\left[\frac{\partial v_\phi}{\partial r} + \frac{v_\phi}{r}\right] \,. \tag{8.20}$$

In Fig. 8.3 the macroscopic particle spin ω and the continuum rotation $\bar{\omega}$, are displayed. In the figure both the total particle rotation and the continuum rotation decay exponentially with increasing $\tilde{r}$, similar to the velocity v_ϕ. Figure 8.4 shows an oscillation of the excess rotation ω^* near the inner wheel, from one disk layer to the next. This is due to the fact that the disks in adjacent layers are able to roll over each other in the shear zone.

In order to obtain the macroscopic quantities of the Cosserat theory from our simulations our provided averaging formalism has to be applied also for the couple stress and the curvature. We define these quantities in analogy to the stress and the strain tensor. Following the derivation of the stress tensor in Sect. 7.3 the couple stress tensor reads as:

$$\boldsymbol{M} = \frac{1}{V}\sum_{p\in V} w_V^p \sum_{c=1}^{\mathcal{C}^p} \left(\vec{l}^{pc} \times \vec{f}^{c}\right) \otimes \vec{l}^{pc} \,. \tag{8.21}$$

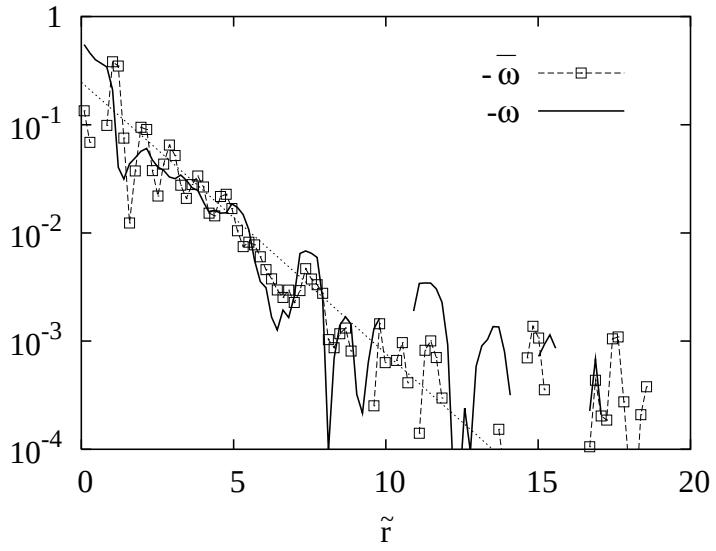

Fig. 8.3: *Angular velocities ω (solid line) of the particles and of the continuum $\bar{\omega}$ (symbols), plotted against the scaled radial distance $\tilde{r}$. The dotted line is $\bar{\omega}$ as obtained from the fit to v_ϕ, see subsection 6.3.1.*

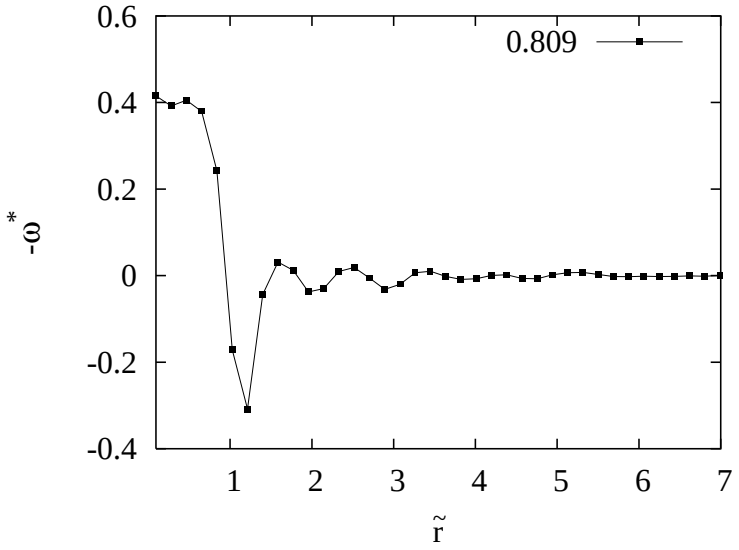

Fig. 8.4: *The data show the excess rotation ω^* of the particles for a global packing fraction $\bar{\nu} = 0.809$ against the scaled radial distance $\tilde{r}$.*

The force in the formulation of the stress tensor is replaced by the torque exerted by the tangential component of the force acting on the branch vector. The '$\times$' denotes the vector-product.

In a two-dimensional system, only the two components M_{zr} and $M_{z\phi}$ of the tensor are non-zero. The values of M_{zr} as a function of $\tilde{r}$ are shown in Fig. 8.5. Note that $\boldsymbol{M} = \mathbf{0}$, when the sum of the torques acting on one particle vanishes in static equilibrium. In our steady state shear situation $\boldsymbol{M}$ fluctuates around zero, except for a large value in the shear band, close to the inner wall.

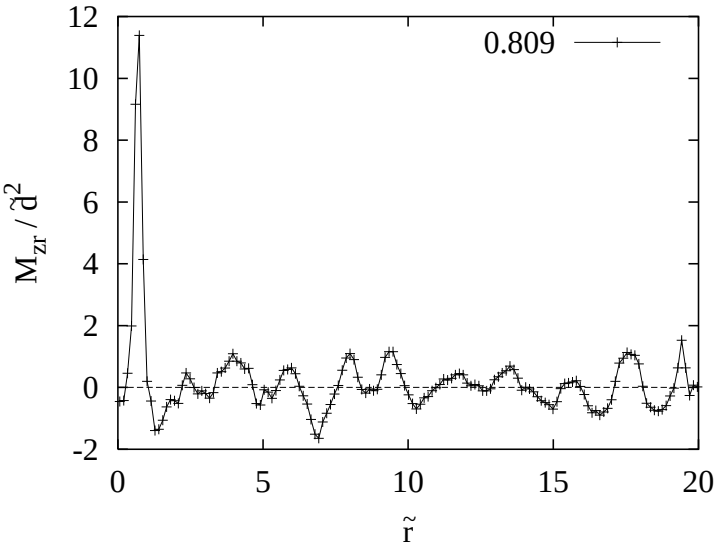

Fig. 8.5: *Plot of the couple stress $M_{zr}/\tilde{d}^2$ against $\tilde{r}$.*

In analogy to $\boldsymbol{\varepsilon}$ we define

$$\boldsymbol{\kappa} = \frac{\pi h}{V} \left(\sum_{p \in V} w_V^p \sum_{c=1}^{C^p} (\vec{l}^{pc} \times \vec{\Delta}^{pc}) \otimes \vec{l}^{pc} \right) \cdot \boldsymbol{A} \,, \tag{8.22}$$

where the local contact displacement $\vec{\Delta}^{pc}$ is replaced by the corresponding angular vector $\vec{l}^{pc} \times \vec{\Delta}^{pc}$. The values of the curvature κ_{zr} are plotted in Fig. 8.6 against $\tilde{r}$ with similar qualitative behavior as M_{zr}. The other components $M_{z\phi}$ and $\kappa_{z\phi}$ lead to no new insights and are omitted here.

Since we are interested in the role the rotational degree of freedom plays for the constitutive equations, we define the "torque resistance" $\mu_c \ell^2$ as the ratio of the magnitudes of the couple stress and the curvature components (see Eq. 8.17). This quantity describes how strongly the material resists against applied torques in analogy to $\bar{E}$ and $\bar{G}$. In Fig. 8.7 the torque resistance is plotted for three simulations with different packing fraction $\bar{\nu}$. In the dilute

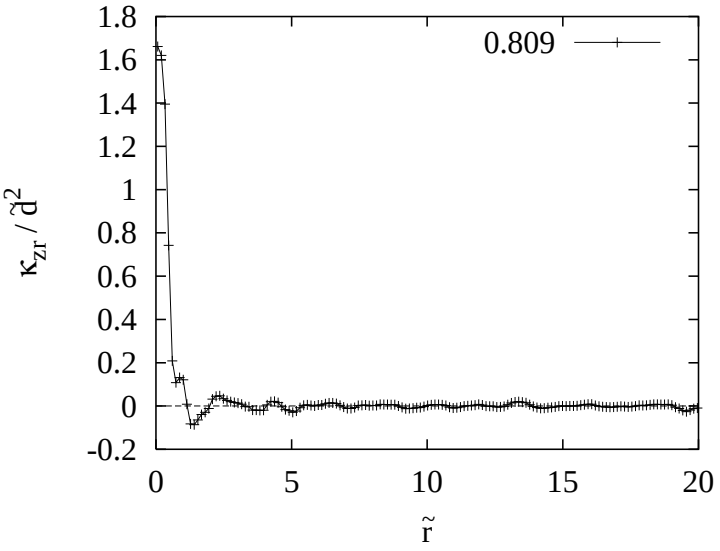

Fig. 8.6: *Plot of the curvature $\kappa_{zr}/\tilde{d}^2$ against $\tilde{r}$.*

regions near the inner wheel, where the particles are less dense packed and are able to rotate more easily because of this dilatancy, μ_c is smaller than in the dense outer part, where the particles are interlocked and thus frustrated. This behavior is consistent with the results for increasing global densities, i.e. the torque resistance increases with density. Note that the strongest fluctuations are due to the division by small κ_{zr} values and have no physical meaning in our interpretation.

8.3 Conclusion

In shear experiments rotations of the grains play an important role in order to foster the ball bearing behavior of adjacent layers of grains. These rotations are not taken into account by classical continuum theories. By using a Cosserat type of continuum theory we extended the previously used continuum theory by rotational degrees of freedom. The total rotation of the particles, as measured experimentally can be decomposed into a continuum rotation and an excess rotation. The continuum rotation can be derived from the continuum theory by means of the velocity gradient and is in good agreement with the simulation results. We calculated the curvature and the

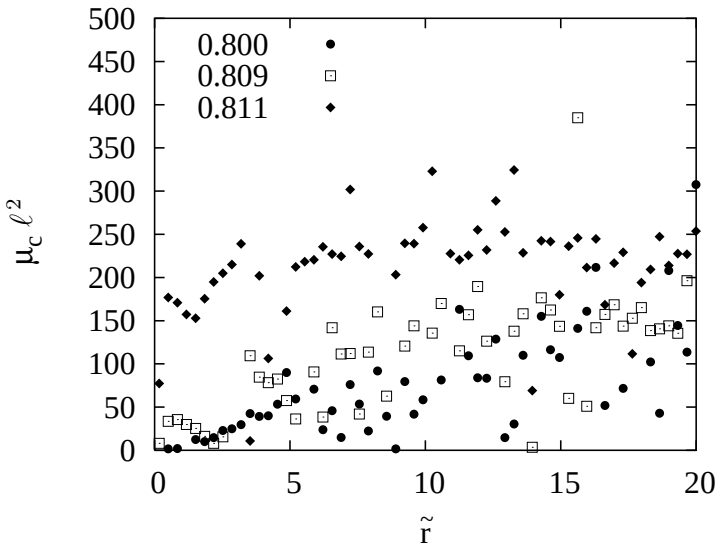

Fig. 8.7: *Torque resistance $\mu_c \ell^2 = M_{zr}/\kappa_{zr}$ plotted against $\tilde{r}$ for various packing fractions.*

couple stress tensor which extend the constitutive equations of the classical continuum theory. The computation of the ratio of the couple stress and the related curvature lead to a new material parameter which we termed torque resistance. It depicts how strongly a material responds to small applied torques. Our results showed that the torque resistance is small in the shear zone due to a small local density and increases in the outer part where the particles are frustrated due to the higher densities. A dense material resists to an applied torque stronger than a dilute system.

9 Frictional Cosserat Model

Shearing experiments of granular material show that the deformation of the material localizes in narrow zones of a width of a few grain diameters. The particles in these shear zones also rotate strongly. The behavior of the granulate in this kind of experiments can not be described properly by classical continuum mechanical models as in Sect.7.1. Especially the width of the shear zone can not be calculated with classical approaches.

One approach to model a granulate under shear are models of Cosserat type. In this kind of models the fields of a classical continuum are supplemented by a couple stress and an intrinsic angular velocity field.

Cosserat plasticity models have been applied to problems in granular flow earlier (MÜHLHAUS [69]; MÜHLHAUS AND VARDOULAKIS [73]; TEJCHMAN AND GUDEHUS [91]; TEJCHMAN AND WU [92, 93]) but the models in these studies are posed in terms of strain increments as they only address unsteady flows, and no results are reported for steady flow. Recently MOHAN ET AL. [66] presented a rigid-plastic Cosserat model for slow frictional flow.

The effects of a Cosserat continuum like asymmetric stress tensors or the deviation of the rotations from the continuum rotations have, to our knowledge, not been directly measured in the laboratory so far. Experiments in this direction would be of value to test the use of a Cosserat continuum as

a description of slow granular flow. However, our simulations enable us to calculate the necessary quantities involved in a Cosserat type continuum theory and thus we have the opportunity to compare the simulation results with the model proposed by Mohan.

9.1 Mohan's Model

The model of Mohan is based on the concept of a Cosserat continuum. Therefore, additional to the stress and the deformation rate tensor as macroscopic field variables of a classical continuum model couple stresses and intrinsic angular velocities are taken into account. The granulate is treated as a material which deforms plastically. In order to solve the balance equations of a Cosserat type theory an associated flow rule is used.

In the following the model of MOHAN ET AL. will briefly be summarized. After the introduction of the basic equations the model will be used to solve a viscometric flow in a Couette shear device as used in this thesis.

Balance Equations in the Absence of Gravity

The model is based on the balance equations of a Cosserat continuum as given in Sect. 8.1. The model is developed in the absence of gravity, therefore no body forces and volume moments appear in the equations:

$$\frac{\partial \rho}{\partial t} + \operatorname{div}(\rho \vec{v}) = 0 \,, \tag{9.1}$$

$$\rho \frac{D\vec{v}}{Dt} - \operatorname{div} \boldsymbol{\sigma} = 0 \,, \tag{9.2}$$

$$\rho \frac{D(\mathcal{I}\vec{\omega})}{Dt} - \operatorname{div} \boldsymbol{M} - \vec{s^*} = 0 \,. \tag{9.3}$$

Where D/Dt is the usual material derivative and $\vec{s^*}$ is the axial vector of the stress tensor. In general, the distribution of size, shape, and orientation of the particles is required to determine the intrinsic inertia tensor $\mathcal{I}$. As the present work is confined to steady, fully developed flow, the term involving $\mathcal{I}$ in Eq. 9.3 vanishes.

Constitutive Equations

These balance equations have to be accompanied by constitutive equations relating the applied stresses and the resulting deformations. In contrast to the constitutive equations used in Sect. 7.1 and Sect. 8.1 Mohan's model treats the material not only as an elastic one but an elasto-plastic material. Therefore, the material deforms elastically under stress, as long as the stress is lower than a specific threshold. If the stress exceeds the threshold value, the material deforms plastically, i.e. in a non reversible way.

Yield Condition

In Sect. 4.2.2 we presented the Coulomb force as the shear force f^t acting on a block sliding on a plane. The shear force f^t is proportional to the normal force f^n with μ_C the friction coefficient being the constant of proportionality. When the block is at rest $f^t < \mu_C f^n$ holds. A continuum analog of this relation is the yield condition F which relates the shear stresses and the stresses acting on a block at rest.

In a classical continuum for elastic material the yield condition is of the form $F(\boldsymbol{\sigma}, \nu) < 0$, where F is a scalar function of the stress tensor $\boldsymbol{\sigma}$ and the volume fraction ν. If $F = 0$, either plastic or irrecoverable deformation occurs.

In order to model this behavior different yield conditions are proposed. Mohan's model is based on an extended VON MISES condition which reads as

$$F = \tau(J_2) - Y(J_1, \nu) \; , \tag{9.4}$$

where τ is the shear stress depending on J_2 the second invariant of the deviatoric stress tensor. Y in Eq. 9.4 is the so called yield function, which depends on J_1, the first invariant (i.e. the trace) of $\boldsymbol{\sigma}$.

To generalize Eq. 9.4 for a Cosserat continuum, additionally τ has to be a function of the couple stress $\boldsymbol{M}$. Following (BESDO [9]; DE BORST [25]) τ is defined as

$$\tau \equiv \left(a_1 \sigma'_{\alpha\beta}\sigma'_{\alpha\beta} + a_2 \sigma'_{\alpha\beta}\sigma'_{\beta\alpha} + \frac{1}{(Ld_p)^2} M_{\alpha\beta} M_{\alpha\beta} \right)^{1/2} \; . \tag{9.5}$$

Here

$$\sigma'_{\alpha\beta} = \sigma_{\alpha\beta} - \frac{1}{3}\sigma_{\gamma\gamma}\delta_{\alpha\beta} \; , \tag{9.6}$$

and $\delta_{\alpha\beta}$ resembles the KRONECKER delta. The parameter L determines the characteristic material length scale, and is perhaps related to the length of force chains (HOWELL ET AL. [42]), d_p is the diameter of the grains and a_1 and a_2 are material constants. These constants are set to equal

$$a_1 + a_2 = 1/2, \tag{9.7}$$

without loss of generality following MÜHLHAUS AND VARDOULAKIS [73]. In the following

$$L = 10, \qquad A \equiv a_2/a_1 = 1/3\,, \tag{9.8}$$

are used just because they nicely fitted experimental data for flow down vertical channels as reported in (MOHAN ET AL. [65]).

In his work DE BORST [25] assumed that the yield function Y depends on the mean stress $\sigma = \sigma_{\gamma\gamma}/3$ and a hardening parameter which is taken as the solids fraction ν thus $Y = Y(\sigma, \nu)$ here. When using $\sigma_c(\nu)$ the mean stress in the critical state (for details, see JACKSON [45]) and ψ the internal friction angle the yield condition might be rewritten as

$$Y = Y_1(\alpha)\sigma_c(\nu)\sin(\psi), \qquad \alpha = \sigma/\sigma_c \tag{9.9}$$

In this study the material is assumed to be in a critical state everywhere, therefore, $\alpha = \sigma/\sigma_c$ is set to 1. Hence, Eq. 9.4 becomes

$$F = \tau - \sigma_c(\nu)\sin(\psi) = 0; \qquad \sigma = \sigma_c(\nu) \tag{9.10}$$

when setting $Y_1(\alpha)$ equal 1 without loss of generality.

In his model Mohan assumes the stress in the critical state $\sigma_c(\nu)$ to vanish when the grains are no longer in sustained contact, and to increase as ν increases. For the sake of simplicity the material is assumed incompressible. Therefore, σ_c is taken as constant and treated as a primitive variable and an explicit expression for $\sigma_c(\nu)$ is not required. The assumption of an incompressible material contradicts the findings in the experiments and the simulations. However, the conclusion of σ_c being constant is rectified by the simulation results shown in Sect. 7.3.3.

Flow Rule

The flow rule relates the deformation rate tensor to the stress tensor. A commonly used flow rule in classical frictional models is the plastic potential

flow rule, which is expressed as

$$D_{\alpha\beta} \equiv \frac{1}{2}\left(\frac{\partial v_\alpha}{\partial x_\beta} + \frac{\partial v_\beta}{\partial x_\alpha}\right) = \lambda' \frac{\partial \Pi}{\partial \sigma_{\beta\alpha}} \,. \tag{9.11}$$

Here $D_{\alpha\beta}$ is the deformation rate tensor, $\Pi(\boldsymbol{\sigma}, \nu)$ is a scalar function called the plastic potential, and λ' is a scalar factor (LAGRANGE multiplier) which must be determined as a part of the solution. As detailed information on the plastic potential Π is usually not available, an associated flow rule[1]

$$\Pi \equiv F = \tau - Y \,, \tag{9.12}$$

is used. This form for the flow rule, in conjunction with a yield condition defined by Eqs. 9.4 and 9.10, accounts for density changes accompanying a deformation. Together, they constitute a rate-independent constitutive relation, which is a desirable feature for slow granular flows.

The flow rule of Eq. 9.11 has to be extended in order to account for a Cosserat continuum. Based on the work of TEJCHMAN AND WU [92] and MÜHLHAUS [69] the flow rule is written as

$$\boldsymbol{D}^* \equiv \vec{\nabla}\vec{v} + \boldsymbol{e} \cdot \vec{\omega} = \lambda' \frac{\partial F}{\partial \boldsymbol{\sigma}^T} \,, \qquad \boldsymbol{W} \equiv \vec{\nabla}\vec{\omega} = \lambda' \frac{\partial F}{\partial \boldsymbol{M}^T} \,. \tag{9.13}$$

The deformation rate tensor $\boldsymbol{D}^*$ is extended by the angular velocities analogous to the deformation tensor $\boldsymbol{\epsilon}$ of Eq.8.3. The second term the angular velocity tensor $\boldsymbol{W}$ relates the rotation rate with the couple stresses.

Coordinate System

In order to compare the results of Mohan's model with the results of our simulations and due to the geometry of the setup cylindrical coordinates are used. Thus, the velocity field for steady axisymmetric flow is of the form

$$v_r = 0, \quad v_z = 0, \quad v_\phi = v_\phi(r) \,. \tag{9.14}$$

Because the grains are two-dimensional disks the angular velocity has only one non-zero component

$$\omega_r = \omega_\phi = 0, \quad \omega_z = \omega_z(r) \,. \tag{9.15}$$

[1] In an associated flow rule the vector of the deformation rate is perpendicular to the flow plane described by the yield condition.

Finally, as a consequence of the incompressibility the diagonal components of $\boldsymbol{\sigma}$ are assumed to be equal and constant

$$\sigma_{rr} = \sigma_{\phi\phi} = \sigma_{zz} = \sigma_c(\nu) = \text{const.} \,. \tag{9.16}$$

In order to compare different sets of data, the variables are rewritten in a dimensionless form.

$$\xi = \frac{r - R_i}{H}, \quad u = \frac{v_\phi}{v_0}, \quad \omega = \frac{\omega_z H}{v_0} \,, \tag{9.17}$$

$$\bar{\sigma}_c = \frac{\sigma_c}{\rho_p g H}, \quad \bar{\sigma}_{\alpha\beta} = \frac{\sigma_{\alpha\beta}}{\rho_p g H \bar{\sigma}_c}, \quad m = \frac{1}{d_p L\sqrt{2(A+1)}} \frac{M_{rz}}{\rho_p g H \bar{\sigma}_c} \,, \tag{9.18}$$

with R_i and v_0 are the radius and the velocity of the inner cylinder, respectively. H denotes the width of the shear cell (the Couette gap).

Set of Equations

Using the symmetries of the Couette device on the Yield condition Eq. 9.10 one obtains

$$(\bar{\sigma}_{r\phi}^2 + \bar{\sigma}_{\phi r}^2) + 2A\bar{\sigma}_{\phi r}\bar{\sigma}_{r\phi} + 4(A+1)^2 m^2 = 2(A+1)(\bar{\sigma}_c \sin(\psi))^2 \,. \tag{9.19}$$

This equation is solved for $\bar{\sigma}_{\phi r}$ as

$$\bar{\sigma}_{\phi r} = -A\bar{\sigma}_{r\phi} \pm \sqrt{((A^2-1)\bar{\sigma}_{r\phi}^2 - 4(A+1)^2 m^2 + 2(A+1)(\bar{\sigma}_c \sin(\psi))^2)} \,. \tag{9.20}$$

With the use of the symmetries of the device and after solving the flow rule of Eq. 9.13 for the factor λ'/τ one obtains:

$$\frac{du}{d\xi} - \frac{u}{(\bar{R}_i + \xi)} = -\left(\omega + \frac{u}{(\bar{R}_i + \xi)}\right) \frac{(A+1)(\bar{\sigma}_{\phi r} + \bar{\sigma}_{r\phi})}{(\bar{\sigma}_{\phi r} + A\bar{\sigma}_{r\phi})}, \tag{9.21}$$

$$\epsilon\alpha \frac{d\omega}{d\xi} = -\left(\omega + \frac{u}{(\bar{R}_i + \xi)}\right) \frac{2(A+1)m}{(\bar{\sigma}_{\phi r} + A\bar{\sigma}_{r\phi})}, \tag{9.22}$$

By applying the dimensionless variables on the balance equations 9.1-9.3 the following set of non dimensional differential equations is obtained:

$$\frac{\partial \bar{\sigma}_{r\phi}}{\partial \xi} + \frac{\bar{\sigma}_{r\phi} + \bar{\sigma}_{\phi r}}{(\bar{R}_i + \xi)} = 0, \tag{9.23}$$

$$\epsilon \left(\frac{\partial m}{\partial \xi} + \frac{m}{(\bar{R}_i + \xi)}\right) = \bar{\sigma}_{r\phi} - \bar{\sigma}_{\phi r} \,. \tag{9.24}$$

Here $\epsilon = d_p/H$ is the non-dimensional particle size and $\bar{R}_i = R_i/H$ is the ratio of the radius of the inner cylinder and the Couette gap.

9.2 Comparison

Using the set of differential equations of the previous section, we compare the theoretical results of the model with those of our molecular dynamic (MD) simulations of a Couette shear cell. The simulation data fit the experimental data of HOWELL (HOWELL ET AL. [42]; VEJE ET AL. [102]) very well as we demonstrated in Sect. 6. Since the simulation and the experiment are performed in slow flow and assumed to have reached a steady state it is reasonable to compare the results with the model.

Parameters

In the current study the parameters $L = 10$ and $A = 1/3$ of the model were retained according to the theory of MOHAN ET AL. [65]. The setup of the Couette shear device was $R_i = 0.1032$ cm and $H = 0.1492$ cm, see Sect. 3. Therefore, $\bar{R}_i = 0.6916$. For the particle diameter we use $d_p = 0.008$ m thus $\epsilon = 0.0536$.

In order to solve the differential equations of the model, one has to specify the boundary conditions of the problem. At the outer wall $(\xi = 1)$ the velocity of the particles is assumed to equal zero $u(\xi = 1) = 0$ as the particles are essentially at rest. The Cosserat effect is assumed to have vanished at the outer boundary so that the stress is symmetric like in the classical continuum $\bar{\sigma}_{r\phi}(\xi = 1) = \bar{\sigma}_{\phi r}(\xi = 1)$.

At the inner cylinder $(\xi = 0)$ the boundary conditions are applied as follows:

$$\bar{\sigma}_{r\phi}(\xi = 0) = -\tan(\delta), \qquad u(\xi = 0) = u_0, \text{ and } \omega(\xi = 0) = \Omega_0 \,. \tag{9.25}$$

The velocity and the angular velocity at the inner shearing wheel have to be taken from the simulation data.

The internal friction angle ψ was chosen to be equal to 22.6^o and for the wall friction a value of $\delta = 9.8^o$ was used in order to fit the data to the theory.

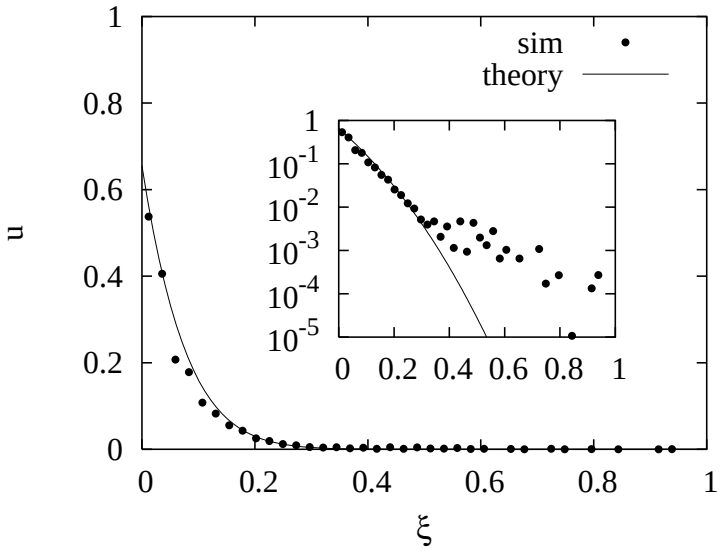

Fig. 9.1: *Velocity profile from the simulation and the calculations of the model (solid line).*

The value for δ seems to be too small, but because of the roughness of the wall and due to the fact that only very few particles are in contact with the wall it could be reasonable.

The resulting *Boundary Value Problem* was solved with the use of MATLAB 6 [60].

The obtained solutions are quite stable against variation of the boundary conditions. In particular, even when changing the boundary values the qualitative behavior inside the shear device stays the same.

Results

The solid line in Fig. 9.1 is the prediction of the model. The value for u_0 was chosen in a way that the velocity of the model matches the simulation data at the inner ring. At the outer ring the model velocity was forced to drop to zero, whereas the simulation data saturates on a small, finite noise-level. Nevertheless, the model fits the simulation data nicely, as can be seen more clearly in the logarithmic inset of Fig. 9.1. As the data of the simulation the velocity of the model also decays. However, the simulation data decay exponentially whereas the model decays even faster.

The other quantity we used to fit the model to the simulation data was the

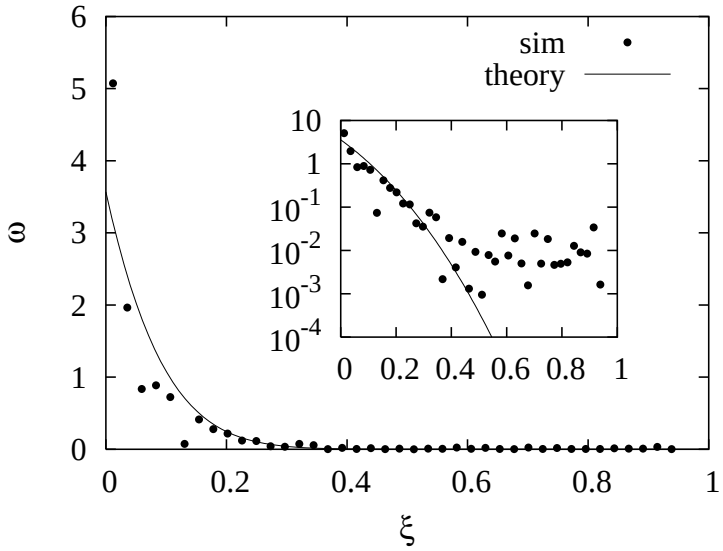

Fig. 9.2: *Angular velocity from simulation and theory. Instead of the oscillating ω in the simulations the absolute value of ω is plotted.*

angular velocity ω. So Ω_0 was obtained from the simulations and put into the model. To compare the model with the simulation data the wall friction angle δ in the model was chosen in a way to match ω at the inner wall. As ω is oscillating in the simulations and this effect is not captured by the model, we used $|\omega|$ to compare to the model. As for the velocity this matching is enough to derive a qualitatively good agreement with the provided data as can be seen in Fig. 9.2.

When comparing the off-diagonal elements of the stress tensor qualitative agreement is found on the first glance. The simulation and the model show an asymmetric stress tensor at the inner wall decaying when moving away from the inner wall. The difference between the two stress components also decreases and fluctuates around zero in the simulations. In the model the difference does not decrease as strong as in the simulations even if forced to equal zero at the outer wall. However, the oscillating behavior of the stress components in the simulations make a quantitative comparison rather difficult, as the difference between the two stress components depends on the radial position and fluctuates quite strongly.

As a last quantity we examine the couple stresses $\boldsymbol{m}$ in Fig. 9.4. Here the model predictions and the results of the simulations show totally different behavior. The couple stresses in the model increases from the inner wall

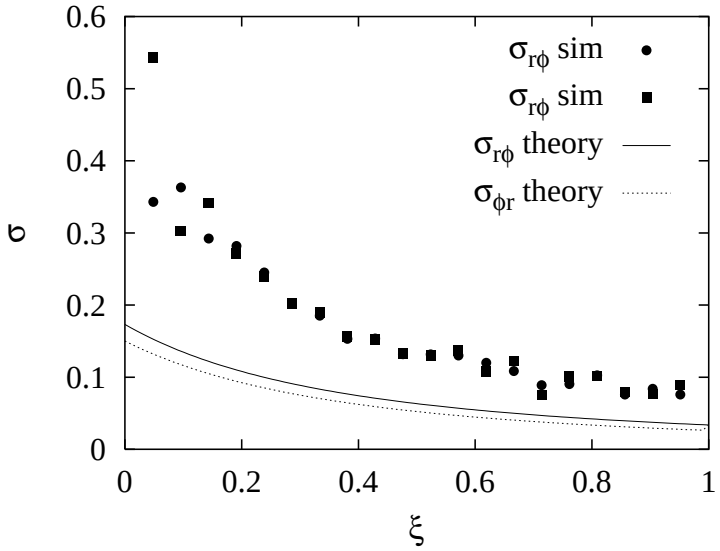

Fig. 9.3: *Plot of the off diagonal elements of the stress in the simulation and the model.*

while moving radial outwards. The couple stress has therefore its maximum value at the outer part of the system. This is contradicted by the results of the simulation. In the simulation the couple stress is highest in the shear zone at the inner wheel and decreases rapidly when moving away from the inner wall. In the outer part the couple stresses of the simulations fluctuate around zero. To us this behavior seems reasonable, as in the inner part the particles are able to rotate and exert stresses onto each other. In the outer part the particles stay at rest and Cosserat effects should not be visible. Therefore the couple stresses should also vanish in the outer region.

9.3 Conclusion

In this section we introduced the frictional Cosserat model of MOHAN ET AL. As there are only experimental data available to verify parts of the model, our simulations resemble an opportunity to test the whole model. The comparison between the simulation results and the model predictions showed good agreement concerning the velocity profiles as well as the angular velocity profiles. The model also predicts the asymmetry of the stress tensor in a similar way as obtained from the simulations. However, the

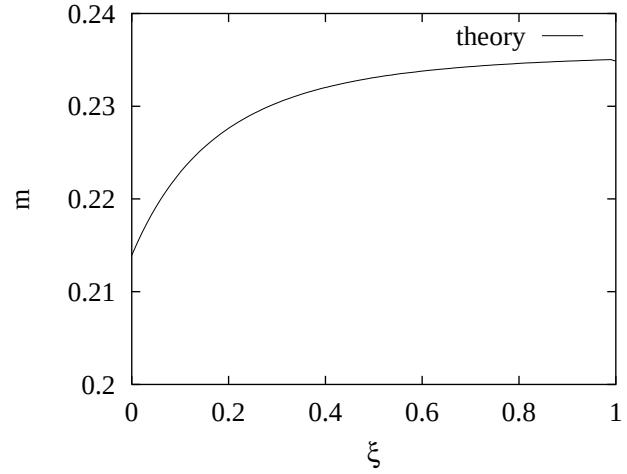

(a)

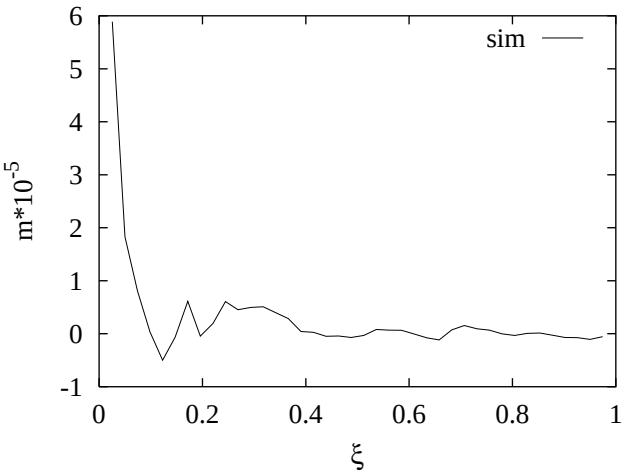

(b)

Fig. 9.4: *Behavior of the couple stress* $\boldsymbol{m}$ *in the Mohan model* **(a)** *and in the simulations* **(b)**.

couple stress tensor of a Cosserat type theory is predicted in the model in a different way as in the simulations. While in the simulation this quantity decays in radial outward direction, it increases in the model and reaches its maximum at the outer wall. At this point further investigations have to clarify what the reasons for the wrong behavior of the model are.

10 Conclusion

The goal of this thesis was to bridge the gap between a microscopic point of view of granular media where all the particles and the forces acting between them are considered and a macroscopic description of granular media where the material can be seen as a continuum. To achieve this goal we implemented a molecular dynamics simulation of a two-dimensional shear cell. The design of the shear cell was setup as close as possible to an actual experiment of that type in Durham (USA) in the group of Prof. R. Behringer.

As a first step a specific averaging formalism for computing macroscopic variables from the simulation was developed and tested. By using the same formalism we measured various quantities from the simulations and compared the results with the experiment. Encouraged by the agreement found, we computed quantities which are not or quite difficult to obtain in the experiment still these quantities lead to a better understanding of the processes happening inside the granular assembly. Within the framework of a continuum mechanics approach tensorial quantities like the stress tensor and the strain tensor were computed. Additionally we measured the fabric tensor which is helpful to describe the structure of a material, especially its degree of anisotropy. The derived field variables were used to compute material parameters of the constitutive relations of a continuum theory. At first we used an elastic Hooke type material law and computed the stiffness and the shear stiffness. As the rotations of the grains of the material play an im-

portant role in the behavior of the system especially in the shear zones the classical continuum theory was extended by the rotational degrees of freedom leading to a Cosserat type theory. Within this kind of theory the balance equations have to be supplemented by equations for the couples and the curvature. We also computed these quantities and derived the torque resistance as an additional material parameter. As a last step of this thesis the results of the simulations were compared to a recently proposed elastoplastic Cosserat model. For the model are no experimental data available yet the simulation provided the possibility to test the model.

10.1 From a Microscopic Point of View...

In order to study the formation and the development of shear bands one has to observe the granular material during a comparatively long time of shearing. Experimentally this can be done in a Couette shear cell. The two-dimensional realization of such a device by the group of Prof. R. Behringer seemed "simple" enough to try to setup a computer simulation which yields the same results as the experiment. In chapters 3 and 4 we reported the geometry and the simulation method used in this study.

Even if the experiment is performed with single particles the measurements taken are averages in time and space. Therefore, one consistent averaging formalism for arbitrary quantities was developed. The proposed averaging formalism proved to give reasonable results for ring shaped areas of the shearing device even if the width of the ring was chosen smaller than an average particle diameter.

With our averaging formalism we computed the local density, the tangential velocity and the rotation field inside our shear cell. The question of whether the numerical simulations are able to reproduce the actual experiment can clearly be answered positive. Our molecular dynamics simulation showed good qualitative agreement with the experimental results of the Behringer group. Partially even quantitative agreement was found despite the simple interaction force laws used and notwithstanding the many differences in details of the setup. The remaining discrepancies could be (possibly) explained by differences that would make the simulations extremely more

complicated and an arduous task. Examples therefore are a possible tilt of the particles out of their plane of motion, a possibly wrong modeling of the bottom friction, and a non-perfect cylindrical inner cylinder. We can see two ways to get rid of the discrepancies. Either a more realistic simulation has to be performed, that takes all details into account. This might be too complex and therefore a non practicable approach. The other way is to think of an even simpler model experiment that does not leave as much space for discrepancies. By this experiment one might learn what the important details in the implementation of a numerical simulation are. Both approaches should lead to a better understanding of the flow behavior and the shear band formation of granular media.

10.2 . . . to a Macroscopic Description

The final goal of the mechanics of granular media is to gain knowledge of the behavior of granular materials under external loads or under externally applied deformations. This goal is often tackled via continuum mechanics relating external loads on the material to the resulting displacements by constitutive relations or vice versa. As an essential ingredient for practical purposes at least a stress-strain relationship should be given as a result of any more fundamental theory.

As a first step in this direction we used our proposed averaging formalism to compute different tensorial quantities. The heterogeneous and discrete nature of granular materials is homogenized by continuum theories. However, we are interested also in the fabric tensor which is one possible measure for the degree of anisotropy of the assembly. The probability distribution to find a contact in a given direction of a particle shows that near the inner wall there are more contacts in tangential direction due to ordering influenced by the wall. Additionally there exist more particle contacts in the direction of $\phi = 60^o$ measured in the shearing direction because the grains resist against the shear or, with other words, contacts are opened due to shear in the opposite direction $-\phi$. Farther away from the shearing wall, the distribution became more homogeneous. At the outer part it became again inhomogeneous, this time due to crystallization effects during the initial compression phase where the grains formed a triangular lattice. The

dynamics in this outer part is slow, therefore this structures survive over long times.

To compute the macroscopic variables stress and strain, we derived those quantities from the microscopic variables forces, contact vectors and contact displacement. For the stress tensor we also took care of the components related to the dynamics of the granulate. However, these components were by orders of magnitude smaller than the stresses due to the forces. Therefore, the dynamical part was neglected in the rest of this thesis as well as components related with the rotations of the grains. These components only appear in the innermost part of the device and are strongly correlated with the shear zone, thus they might be of interest for further studies.

The behavior of the stress tensor can be predicted by continuum theoretical considerations. The diagonal elements of the stress tensor are constant, whereas the off-diagonal elements related to the shear decay proportional to $1/r^2$ when increasing the distance to the inner wall. These findings are in agreement with the simulations and also explain why the shear band is always found at the inner wall where the shear stress is largest.

The definition of the strain tensor is a controversial topic of current research. In our thesis we derived the strain based on a least square fit approach. With the stress and the strain at hand we computed the granular stiffness E and the shear stiffness G in the framework of an isotropic elastic material law of Hooke type. Even if the assumption of an isotropic material is wrong in large parts of the material we were able to collapse the computed stiffness for various packing fractions on one curve when plotted against the trace of the fabric tensor. This result is in agreement with mean field considerations. The shear modulus of different simulations also collapsed on one curve when plotted against the trace of the fabric for points near or within the shear band. In the outer part of the shear-cell the particles are strongly inter-locked and thus resist much more against shear, so that G diverges. For increasing global density, the critical contact number density also grows and has a proportionality factor of about $1/3$.

An interesting feature of shear experiments are the rotations occurring intensified in the shear zone. This rotations foster the rolling of layers of granulate like a gear. In the classical continuum theory these rotations are not considered. Therefore, we chose a Cosserat theory as an extension. In this type of theory not only translatoric degrees of freedom are taken into ac-

count, but also the rotational ones. The total particle rotation can be decomposed into a continuum rotation and an excess rotation. The continuum rotation can be derived from the continuum theory by means of the antisymmetric part of velocity gradient and is in good agreement with the simulation results.

The constitutive equations of the Cosserat continuum have to be extended by a relation between the curvature and the couple stresses. From considerations analogous to those of stress and strain, we were able to compute the curvature and the couple stress. These quantities resemble the core of a micropolar theory and their derivation and understanding are essential to compare the internal length of a Cosserat theory with length scales of other models. A first step in this direction is the computation of the ratio of the couple stress and the related curvature. This quotient is a new material parameter we termed as torque resistance the rotational equivalent to the elastic moduli. It depicts how strongly a material responds to small applied torques. Our results showed that the torque resistance is small in the shear zone due to a small local density and increases in the outer part where the particles are frustrated due to the higher densities. A dense material resists to an applied torque stronger than a dilute system.

At the end of this thesis the simulation was compared with a recently proposed frictional Cosserat model. By now there are no experimental results available to verify the model. However, we were able to compute the necessary kinematic quantities. The comparison showed good agreement between the predicted and the measured velocity profiles and rotation profiles. Also the model predicted the antisymmetric stress tensor qualitatively correct it failed to describe the couple stress tensor of the Cosserat theory. While in the simulation this quantity decays in radial outward direction, it increases in the model and reaches its maximum at the outer wall. At this point further investigations have to clarify what the reasons for the wrong behavior of the model are.

10.3 Outlook

Despite the fact that investigations in shear bands and shear zones are subject to research from various scientific communities, there are still many

open questions in this field. Some of them have been attacked in this work but at the same time new questions arose.

A general problem of the study of shear bands is how to measure processes and quantities deeply inside the media. Computer simulations provide a tool which opens the possibility to keep track of all forces velocities and other quantities of every grain. In this thesis we showed that numerical simulations as the molecular dynamics are able to reproduce an actual experiment. Still, there were difficulties which could be investigated more closely as the role of tilting of the particles and the effects of friction with the walls and the bottom plate.

Another subject not addressed in this work was the question of the behavior of non-spherical particles. Especially the rotations of the particles will change significantly. On the one hand a non-spherical shape gives rise to higher moments acting on the particles, while on the other hand the particles will inter-lock more strongly, thus reducing rotations.

We also encourage the study of three dimensional systems as in our geometry the only direction for the grains to dilate was the radial outward one. Whereas in a three dimensional geometry the particles can also move up- and downwards. The mentioned inter-locking will also increase as it becomes more difficult to form the ball bearing shown in the two-dimensional system. Since recent experiments are available to guide 3D simulations in that direction.

In order to perform the transition from the microscopic discrete variables to the macroscopic field variables a homogenization method is needed. We showed that this could be done with the proposed averaging formalism. Yet, the question of the proper size for an averaging volume remains controversial. In our geometry due to the possibility of space and time averaging we were able to use rather small areas. However, for a different kind of system, where one wants to measure quantities only at one time instant and deduce macroscopic variables out of these data the volume might be chosen more carefully, possibly much larger.

We have to bear in mind that in continuum theories the role of the structure of the packing is not taken into account in general. Especially in the presented definition of the strain tensor the opening and closing of contacts is not captured at all. Therefore, a definition of the strain which takes into account the neighborhood of particles seems to be of interest. This kind of exten-

sions also would possibly be able to capture plastic deformations occurring in the granular assembly. Furthermore, we think that a theory including the anisotropy of the granulate might be useful in order to find effective moduli which predict more completely the response of the granular material to external loads and take into account the anisotropy of the packing.

Concerning the question of the usefulness of a micropolar Cosserat approach to granular media we showed that there are strong reasons for doing so. We found localization of tangential displacement as well as of grain rotations accompanied by a density decrease in an interface layer of a few grain diameters. These phenomena are not predicted by classical continuum theories whereas Cosserat type theories include inherently a length scale enabling a prediction of the width of such fault zones. However, the shear zone in which the couple stresses and curvatures play an important role are quite small. In order to increase the effect of moments transmitted at the contacts non-spherical particles seem to be promising. In that case the equations derived in this study have to include not only the moments resulting from the contact forces, but the particles might transmit moments directly at a contact.

Finally, the most difficult question is whether any continuum model will be able to account for the oscillations of the rotation directions of the layers of the granulate. We do not know if this information is crucial in correctly predicting the behavior of the granulate on a larger scale, but on a small microscopic scale it seems an arduous task and we are not aware of a continuum description that seems able to describe oscillating rotations and the rolling of layers.

As the industrial applications of granular media are quite large and cover a great range of product lines the understanding of the behavior of granular media is of big importance. In this thesis we focused on the subject of shearing and showed various approaches to predict the behavior of a granulate in a shear device. We hope that our work will stimulate further investigations and will be inspiring to the community searching for answers in the field of granular matter. The path to the final goal of a theory of granular media might be long but on the other hand it is still very exciting.

Bibliography

[1] M. P. Allen and D. J. Tildesley. *Computer Simulation of Liquids*. Oxford University Press, Oxford, 1987.

[2] J. A. Astrøm, H. J. Herrmann, and J. Timonen. Granular packings and fault zones. *Phys. Rev. Lett.*, 84(4):638–641, 2000.

[3] E. Azanza, F. Chevoir, and P. Moucheront. Experimental study of collisional granular flows down an inclined plane. *J. Fluid Mech.*, 400: 199–227, 1999.

[4] K. Bagi. Stress and strain in granular assemblies. *Mechanics of Materials*, 22:165–177, 1996.

[5] K. Bagi. Microstructural stress tensor of granular assemblies with volume forces. *Journal of Applied Mechanics*, 66:934–936, 1999.

[6] Y. M. Bashir and J. D. Goddard. A novel simulation method for the quasi-static mechanics of granular assemblages. *J. Rheol.*, 35(5):849–885, 1991.

[7] P. Z. Bažant and B. H. Gambarova. Crack shear in concrete: Crack band microplane model. *J. Struct. Engng.*, 110:2015–2036, 1984.

[8] E. Becker and W. Bürger. *Kontinuumsmechanik*. B. G. Teubner, Stuttgart, 1 edition, 1975.

[9] D. Besdo. Ein Beitrag zur nichtlinearen Theorie des Cosserat-Kontinuums. *Acta Mechanica*, 20:105–131, 1974.

[10] L. Bocquet, W. Losert, D. Schalk, T. C. Lubensky, and J. P. Gollub. Granular shear flow dynamics and forces: Experiments and continuum theory. *Phys. Rev. E*, 65:011307, 2002. cond-mat/0012356.

[11] N. Bogdanova-Bontcheva and H. Lippmann. Rotationssymmetrisches ebenes Fließen eines granularen Modellmaterials. *Acta Mechanica*, 21: 93–113, 1975.

[12] L. Brendel and S. Dippel. Lasting contacts in molecular dynamics simulations. In H. J. Herrmann, J.-P. Hovi, and S. Luding, editors, *Physics of Dry Granular Media*, page 313, Dordrecht, 1998. Kluwer Academic Publishers.

[13] H. Buggisch and G. Löffelmann. Theoretical and experimental investigations into the local granulate mixing mechanisms. *Chemical Engineering and Processing*, 26(3):193–200, 1989.

[14] B. Cambou, F. Dubujet, F. Emeriault, and F. Sidoroff. Homogenization for granular materials. *Eur. J. Mech. A/Solids*, 14(2):255–276, 1995.

[15] B. Cambou and P. Dubujet. Difficulties and limitations of statistical homogenization in granular materials. In P. A. Vermeer, S. Diebels, W. Ehlers, H. J. Herrmann, S. Luding, and E. Ramm, editors, *Continuous and Discontinuous Modelling of Cohesive Frictional Materials*, pages 205–214, Berlin, 2001. Springer.

[16] R. Chambon, T. Matsuchima, and D. Caillerie. Microstructured materials: local constitutive equation with internal length, theoretical and numerical studies. In P. A. Vermeer, S. Diebels, W. Ehlers, H. J. Herrmann, S. Luding, and E. Ramm, editors, *Continuous and Discontinuous Modelling of Cohesive Frictional Materials*, pages 275–291, Berlin, 2001. Springer.

[17] C. S. Chang. Numerical and analytical modeling for granulates. In Yuan, editor, *Computer Methods and Advances in Geomechanics*, Rotterdam, 1997. A. A. Balkema.

[18] J. Christofferson, M. M. Mehrabadi, and S. Nemat-Nasser. A micromechanical description of granular material behavior. *J. Appl. Mech.*, 48(2):339–344, 1981.

[19] E. Cosserat and F. Cosserat. *Theorie des Corps Deformables*. Herman et fils, Paris, 1909.

[20] M. Coulomb. Theorie des Machines Simples. *Academie des Sciences*, 10:166, 1781.

[21] S. C. Cowin. A simple theory of instantaneously induced anisotropy. In J. T. Jenkins and M. Satake, editors, *Micromechanics of Granular Materials*, pages 71–80, Amsterdam, 1988. Elsevier.

[22] P. A. Cundall and R. Hart. Numerical modelling of discontinua. *Eng. Comp.*, 9:101–113, 115–287, 1992.

[23] P. A. Cundall and O. D. L. Strack. A discrete numerical model for granular assemblies. *Géotechnique*, 29(1):47–65, 1979.

[24] R. de Borst. Simulation of strain localization: A reappraisal of the Cosserat continuum. *Engng. Comp.*, 8:317–332, 1991.

[25] R. de Borst. A generalisation of j_2-flow theory for polar continua. *Comput. Methods Appl. Mech. Engrg.*, 103:347–362, 1993.

[26] F. Dedecker, M. Chaze, P. Dubujet, and B. Cambou. Specific features of strain in granular materials. *Mech. Coh.-Fric. Mat.*, 5(3):174–193, 2000.

[27] T. G. Drake. Structural features in granular flows. *J. of Geophysical Research*, 95(B6):8681–8696, 1990.

[28] W. Ehlers and W. Volk. Cosserat-Theorie für gesättigte poröse Festkörper. *Zeitschrift für Angewandte Mathematik und Mechanik (ZAMM)*, 77(Supplement 1):83–84, 1997.

[29] A. C. Eringen. Theory of micropolar elasticity. In H. Liebowitz, editor, *Fracture*, volume 2, pages 621–729. Academic Press, New York and London, 1968.

[30] A. C. Eringen and C. B. Kafadar. Polar field theories. In A. C. Eringen, editor, *Continuum Mechanics*, volume VI, pages 1–73. Academic Press, 1976.

[31] Z. Farkas, G. Bartels, T. Unger, and D. E. Wolf. Frictional coupling between sliding and spinning motion. cond-mat/0210024, 2002.

[32] S. F. Foerster, M. Y. Louge, H. Chang, and K. Allia. Measurements of the collision properties of small spheres. *Phys. Fluids*, 6(3):1108–1115, 1994.

[33] J. Geng, D. Howell, E. Longhi, R. P. Behringer, G. Reydellet, L. Vanel, E. Clément, and S. Luding. Footprints in sand: The response of a granular material to local perturbations. *Phys. Rev. Lett.*, 87:035506, 2001.

[34] P. Germain. La méthode des puissances virtuelles en mécanique des milieux continus. *J. Mécanique*, 12:236–274, 1973.

[35] J. D. Goddard. Continuum modeling of granular assemblies. In H. J. Herrmann, J.-P. Hovi, and S. Luding, editors, *Physics of Dry Granular Media*, pages 1–24, Dordrecht, 1998. Kluwer Academic Publishers.

[36] I. Goldhirsch. Note on the definition of stress for discrete systems. preprint, 1999.

[37] W. Günther. *Zur Statik und Kinematik des Cosseratschen Kontinuums*, volume 10, pages 195–213. 1958.

[38] J. P. Hansen and I. R. McDonald. *Theory of simple liquids*. Academic Press Limited, London, 1986.

[39] H. J. Herrmann. Die wunderbare Welt der Schüttgüter. *Physikalische Blätter*, 51(11):1083, 1995.

[40] H. J. Herrmann and S. Luding. Modeling granular media with the computer. *Continuum Mechanics and Thermodynamics*, 10:189–231, 1998.

[41] H. Hertz. Über die Berührung fester elastischer Körper. *J. für die reine u. angew. Math.*, 92:136, 1882.

[42] D. Howell, R. P. Behringer, and C. Veje. Stress fluctuations in a 2d granular Couette experiment: A continuous transition. *Phys. Rev. Lett.*, 82(26):5241–5244, 1999.

[43] D. W. Howell. *Stress Distributions and Fluctuations in Static and Quasi-static Granular Systems*. PhD thesis, Duke University, Department of Physics, 1999.

[44] D. W. Howell, R. P. Behringer, and C. T. Veje. Fluctuations in granular media. *Chaos*, 9(3):559–572, 1999.

[45] R. Jackson. Some mathematical and physical aspects of continuum models for the motion of the granular materials. In R. E. Meyer, editor, *Theory of Dispersed Multiphase Flow*, pages 291–337. Academic Press, New York., 1983.

[46] H. M. Jaeger and S. R. Nagel. Physics of the granular state. *Science*, 255:1523, 1992.

[47] N. P. Kruyt and L. Rothenburg. Micromechanical definition of strain tensor for granular materials. *ASME Journal of Applied Mechanics*, 118: 706–711, 1996.

[48] N. P. Kruyt and L. Rothenburg. Statics of the elastic behavior of granular materials. *Int. J. of Solids and Structures*, 38:4879–4899, 2001.

[49] L. D. Landau and E. M. Lifshitz. *Elasticity Theory*. Pergamon Press, Oxford, 1975.

[50] M. Lätzel, S. Luding, and H. J. Herrmann. From discontinuous models towards a continuum description. In P. A. Vermeer, S. Diebels, W. Ehlers, H. J. Herrmann, S. Luding, and E. Ramm, editors, *Continuous and Discontinuous Modelling of Cohesive Frictional Materials*, pages 215–230, Berlin, 2001. Springer.

[51] C.-L. Liao, T.-P. Chang, D.-H. Young, and C. S. Chang. Stress-strain relationship for granular materials based on the hypothesis of best fit. *Int. J. Solids & Structures*, 34:4087–4100, 1997.

[52] G. Löffelmann. *Theoretische und experimentelle Untersuchungen zur Schüttgut-Wand-Wechselwirkung und zum Mischen und Entmischen von Granulaten*. PhD thesis, Universität Fridericiana Karlsruhe, 1989. Fakultät für Chemieingenieurwesen.

[53] W. Losert, L. Bocquet, T. C. Lubensky, and J. P. Gollub. Particle dynamics in sheared granular matter. *Phys. Rev. Lett.*, 85(7):1428–1431, 2000. cond-mat/0004401.

[54] W. Losert, D. G. W. Cooper, and J. P. Gollub. Propagating front in an excited granular layer. *Phys. Rev. E*, 59:5855, 1999.

[55] S. Luding. Collisions & contacts between two particles. In H. J. Herrmann, J.-P. Hovi, and S. Luding, editors, *Physics of dry granular media - NATO ASI Series E350*, page 285, Dordrecht, 1998. Kluwer Academic Publishers.

[56] S. Luding. Structures and non-equilibrium dynamics in granular media. *Comptes Rendus Academie des Science*, 3:153–161, 2002.

[57] S. Luding, E. Clément, A. Blumen, J. Rajchenbach, and J. Duran. Anomalous energy dissipation in molecular dynamics simulations of grains: The "detachment effect". *Phys. Rev. E*, 50:4113, 1994.

[58] S. Luding, M. Lätzel, and H. J. Herrmann. From discrete element simulations towards a continuum description of particulate solids. In A. Levy and H. Kalman, editors, *Handbook of Conveying and Handling of Particulate Solids*, pages 39–44, Amsterdam, The Netherlands, 2001. Elsevier.

[59] L. E. Malvern. *Introduction to the mechanics of a continuous medium*. Prentice-Hall series in engineering of the physical sciences. Prentice-Hall, Englewood Cliffs, NJ, 1969.

[60] MATLAB 6. Release 12. by The MathWorks, Inc., 2000.

[61] H.-G. Matuttis, S. Luding, and H. J. Herrmann. Discrete element methods for the simulation of dense packings and heaps made of spherical and non-spherical particles. *Powder Technology*, 109:278–292, 2000.

[62] M. M. Mehrabadi, S. Nemat-Nasser, H. M. Shodja, and G. Subhash. Some basic theoretical and experimental results on micromechanics of granular flow. In *Micromechanics of granular media*, Amsterdam, 1988. Elsevier.

[63] R. W. Mei, H. Shang, O. R. Walton, and J. F. Klausner. Concentration non-uniformity in simple shear flow of cohesive powders. *Powder Technology*, 112(1-2):102–110, 2000.

[64] B. Miller, C. O'Hern, and R. P. Behringer. Stress fluctuations for continously sheared granular materials. *Phys. Rev. Lett.*, 77:3110–3113, 1996.

[65] L. S. Mohan, P. R. Nott, and K. K. Rao. A frictional Cosserat model for the flow of granular materials through a vertical channel. *Acta Mech.*, 138:75–96, 1999. cond-mat/9904167.

[66] L. S. Mohan, K. K. Rao, and P. R. Nott. A frictional Cosserat model for the slow shearing of granular materials. *J. Fluid Mech.*, 457:377–409, 2002. cond-mat/0107563.

[67] D. M. Mueth, G. F. Debregeas, G. S. Karczmar, P. J. Eng, S. R. Nagel, and H. M. Jaeger. Signatures of granular microstructure in dense shear flows. *Nature*, 406:385–389, 2000. cond-mat/0003433.

[68] D. M. Mueth, H. M. Jaeger, and S. R. Nagel. Force distribution in a granular medium. *Phys. Rev. E.*, 57(3):3164–3169, 1998.

[69] H.-B. Mühlhaus. Application of Cosserat theory in numerical solution of limit load problems. *Ing. Arch.*, 59:124–137, 1989.

[70] H.-B. Mühlhaus, editor. *Continuum Models for Materials with Microstructure*. Wiley, New York, 1995.

[71] H.-B. Mühlhaus and A. C. Aifantis. A variational principle for gradient plasticity. *Int. J. Solids & Structures*, 28:845–857, 1991.

[72] H.-B. Mühlhaus, H. Sakaguchi, L. Moresi, and M. Fahey. Discrete and continuum modelling of granular materials. In P. A. Vermeer, S. Diebels, W. Ehlers, H. J. Herrmann, S. Luding, and E. Ramm, editors, *Continuous and discontinuous modelling of cohesive-frictional materials*, number 568 in Lecture Notes in Physics, pages 185–204. Springer, 2001.

[73] H.-B. Mühlhaus and I. Vardoulakis. The thickness of shear bands in granular materials. *Géotechnique*, 37(3):271–283, 1987.

[74] R. M. Nedderman and C. Laohakul. The thickness of the shear zone of flowing granular material. *Powder Technol.*, 25:91, 1980.

[75] M. Nicodemi, A. Coniglio, and H. J. Herrmann. Compaction and force propagation in granular packings. *Physica A*, 240:405, 1997.

[76] E. R. Nowak, M. Povinelli, H. M. Jaeger, S. R. Nagel, J. B. Knight, and E. Ben-Naim. Studies of granular compaction. In *Powders & Grains 97*, pages 377–380, Rotterdam, 1997. Balkema.

[77] P3T class libraries. A C++ software kit for general particle tracking applications. http://www.ica1.uni-stuttgart.de/Research/Software_P3T/P3T.html, 2001.

[78] T. Pöschel and S. Luding, editors. *Granular Gases*, Berlin, 2001. Springer. Lecture Notes in Physics 564.

[79] W. H. Press, S. A. Teukolsky, W. T. Vetterling, and B. P. Flannery. *Numerical Recipes*. Cambridge University Press, Cambridge, 1992.

[80] F. Radjai, J. Schäfer, S. Dippel, and D. Wolf. Collective friction of an array of particles: A crucial test for numerical algorithms. *J. Phys. I France*, 7:1053, 1997.

[81] F. Radjai, D. E. Wolf, S. Roux, M. Jean, and J. J. Moreau. Force networks in dense granular media. In R. P. Behringer and J. T. Jenkins, editors, *Powders & Grains 97*, pages 211–214. Balkema, Rotterdam, 1997.

[82] D. C. Rapaport. *The Art of Molecular Dynamics Simulation*. Cambridge University Press, Cambridge, 1995.

[83] L. Rothenburg and A. P. S. Selvadurai. A micromechanical definition of the Cauchy stress tensor for particulate media. In A. P. S. Selvadurai, editor, *Mechanics of Structured Media*, pages 469–486. Elsevier, Amsterdam, 1981.

[84] M. Satake. Three-dimensional discrete mechanics of granular materials. In N. A. Fleck and A. C. E. Cocks, editors, *IUTAM Symposium on Mechanics of Granular and Porous Materials*, pages 193–202. Kluwer Academic Publishers, 1997.

[85] H. Schaefer. Das Cosserat-Kontinuum. *Zeitschrift für angewandte Mathematik und Mechanik*, 47(8):485–498, 1967.

[86] J. Schäfer, S. Dippel, and D. E. Wolf. Force schemes in simulations of granular materials. *J. Phys. I France*, 6:5–20, 1996.

[87] S. Schöllmann. Modellierung von Reibungsmaterialien mit Diskontinuumsmethoden. Master's thesis, Universität Stuttgart, 1998.

[88] S. Schöllmann. Simulation of a two-dimensional shear cell. *Phys. Rev. E*, 59(1):889–899, 1999.

[89] P. Steinmann. A micropolar theory of finite deformation and finite rotation multiplicative elastoplasticity. *Int. J. Solids & Structures*, 31: 1063–1084, 1994.

[90] P. Steinmann and K. Willam. Localization within the framework of micropolar elastoplasticity. In J. N. O. B. V. Mannl, editor, *Advances in Continuum Mechanics*, volume VI, pages 296–313. Springer, Berlin, 1991.

[91] J. Tejchman and G. Gudehus. Silo music and silo-quake experiments and a numerical cosserat approach. *Powder Technol.*, 76:201, 1993.

[92] J. Tejchman and W. Wu. Numerical study of patterning of shear bands in a cosserat continuum. *Acta Mech.*, 99:61–74, 1993.

[93] J. Tejchman and W. Wu. Numerical study on sand and steel interfaces. *Mech. Res. Comm.*, 21(2):109–119, 1994.

[94] C. Thornton. Coefficient of restitution for collinear collisions of elastic-perfectly plastic spheres. *Journal of Applied Mechanics*, 64:383–386, 1997.

[95] C. Thornton. Numerical simulations of deviatoric shear deformation of granular media. *Géotechnique*, 50(1):43–53, 2000.

[96] C. Thornton and S. J. Antony. Quasi-static deformation of a soft particle system. *Powder Technology*, 109(1-3):179–191, 2000.

[97] C. Thornton and K. K. Yin. Impact of elastic spheres with and without adhesion. *Powder Technol.*, 65:153, 1991.

[98] C. Truesdell. *The mechanical foundations of elasticity and fluid dynamics*, volume 1 of *Continuum mechanics*. Gordon & Breach, New York, international science review series edition, 1966.

[99] O. Tsoungui, D. Vallet, J.-C. Charmet, and S. Roux. "partial pressures" supported by granulometric classes in polydisperse granular media. *Phys. Rev. E*, 57(4):4458–4465, 1998.

[100] L. Vanel, P. Claudin, J.-P. Bouchaud, M. E. Cates, E. Clément, and J. P. Wittmer. Stresses in silos: Comparison between theoretical models and new experiments. *Phys. Rev. Lett.*, 84(7):1439–1442, 2000.

[101] C. T. Veje and P. Dimon. Two-dimensional granular flow in a small-angle funnel. *Phys. Rev. E*, 54(4):4329–4337, 1996.

[102] C. T. Veje, D. W. Howell, and R. P. Behringer. Kinematics of a 2D granular Couette experiment at the transition to shearing. *Phys. Rev. E*, 59(1):739–745, 1999.

[103] C. T. Veje, D. W. Howell, R. P. Behringer, S. Schöllmann, S. Luding, and H. J. Herrmann. Fluctuations and flow for granular shearing. In H. J. Herrmann, J.-P. Hovi, and S. Luding, editors, *Physics of Dry Granular Media*, page 237, Dordrecht, 1998. Kluwer Academic Publishers.

[104] L. Verlet. Computer "experiments" on classical fluids. I. Thermodynamical properties of Lennard-Jones molecules. *Phys. Rev.*, 159(1):98–103, 1967.

[105] W. Volk. *Untersuchung des Lokalisierungsverhaltens mikropolarer por"oser Medien mit Hilfe der Cosserat-Theorie*. PhD thesis, University of Stuttgart, Institut für Mechanik (Bauwesen), 1999.

[106] G. F. Voronoi. Nouvelles applications des parametres continus a la theorie des formes quadratiques. deuxieme emorie: Recherches sur les paralleloedres primitifs. *J. für die reine u. angew. Math.*, 134:198–287, 1908.

[107] O. R. Walton and R. L. Braun. Stress calculations for assemblies of inelastic spheres in uniform shear. *Acta Mechanica*, 63:73, 1986.

[108] O. R. Walton and R. L. Braun. Viscosity, granular-temperature, and stress calculations for shearing assemblies of inelastic, frictional disks. *Journal of Rheology*, 30(5):949–980, 1986.

[109] A. Zervos. *Micropolar properties of two-dimensional discrete media*. PhD thesis, Section of Mechanics, National Technical University of Athens, 1996. Diploma Dissertation.

[110] A. Zervos, I. Vardoulakis, M. Jean, and P. Lerat. Numerical investigation of granular interfaces kinematics. *Mech. Coh.-Fric. Mat.*, 5:305–324, 2000.

Acknowledgments

At the end of this thesis I would like to thank all those who made this work possible.

First and foremost, I want to thank my supervisor Prof. Dr. Stefan Luding, who offered me such an interesting subject and introduced me to the world of scientific research. I enjoyed great freedom in pursuing my research interests and gathered a wealth of invaluable experience in many aspects of academic life. The fruitful discussions with him and his tireless corrections of my publications encouraged me in writing this thesis.

I am indebted to Prof. Dr. Udo Seifert who accepted to referee this thesis.

Likewise I am grateful to Prof. Dr. Hans J. Herrmann who gave me the opportunity to work on my thesis at the ICA1.

I thank Prof. R. P. Behringer and Dan Howell of the Physics Department of Duke University for the opportunity to share their experimental data of the Couette device and for their hospitality during my stay in Durham.

I want to express my thanks to all my current and former colleagues of the ICA1, Stuttgart. They supported this work directly and indirectly by an excellent working atmosphere, system administration, and a programming library. A very special thank belongs to our secretary Marlies Parsons who supported me at the ICA1 concerning all administrative affairs.

I want to acknowledge the financial support of the German Science Foundation (DFG) through the research group “Modeling of Cohesive-Frictional Materials”. I am also grateful to the members of this research group for the fruitful discussions and inspiring ideas.

I do not want to close this thesis without thanking my fellow students Steffen Krusch, Gunther Schaaf, Holger Kollmer and Markus Schulte. They made studying physics an enjoyable task.

Furthermore, I would like to thank my family, especially my parents and my sister, who provided a stable and stimulating environment for my personal and intellectual development.

Finally, I gratefully acknowledge the constant support of my loving and caring wife Alexandra, who influenced my life and work in many ways, and whose proofreading and commenting of this thesis was an important contribution to its final form.

As undoubtedly, this list of acknowledgments is essentially incomplete, I would like to express my gratitude for the constant support of all the people I have been associated with during the past years.